NOVEL DETECTION METHODS AND GAS-FREE HYDROXIDE ELUENT GENERATOR FOR CAPILLARY LIQUID/ION CHROMATOGRAPHY

by

BIKASH CHOUHAN

Presented to the Faculty of the Graduate School of
The University of Texas at Arlington in Partial Fulfillment
of the Requirements
for the Degree of

DOCTOR OF PHILOSOPHY

THE UNIVERSITY OF TEXAS AT ARLINGTON
August 2020

I dedicate this dissertation to my late parents,

Khadga B. Chouhan and Bishnu D. Chouhan

Acknowledgements

I feel very fortunate to have Dr. Dasgupta as my supervising professor. He is a great analytical chemist and a fabulous mentor. I am very grateful to him for his guidance and supervision during my graduate career. What I have learned and achieved as a graduate student is because of his continuous effort to push me to do the best with his never-ending ideas and motivations. I also would like to thank my graduate committee members: Dr. Daniel W. Armstrong, Dr. Saiful Chowdhury, and Dr. Frank W. Foss Jr., for their valuable suggestions and time.

I want to thank and appreciate the faculty members and staff in the Department of Chemistry and Biochemistry for their assistance during my tenure as a Ph.D. student. At this time, I would like to extend my gratitude to Dr. Charles P. Shelor for his continuous guidance and support in my research activities. I would also like to thank Dr. Weixiong Huang and Dr. Chuchu Qin for their valuable help and suggestions. I am equally thankful to all my colleagues: Akinde, Fereshteh, Dr. Masaki, Andrew, Shane, Sajad, Payton, Roger, Joseph, Kamil, Magdalena, and everyone whose name I could not mention here.

My heartfelt gratitude goes to all my family members and friends for their encouragement and support. I am truly indebted to my parents and my brother for giving all the supports and resources I needed to become who I am today. The most significant appreciation goes to my wife, Shanta, because of whose tireless support, motivation, and encouragement that helped me achieving this degree. Finally, my love and thankfulness to my sweet daughters: Upasana and Avika for bringing smile on my face even when I am back home exhausted after a long, hectic day.

June 15, 2020

Abstract

NOVEL DETECTION METHODS AND GAS-FREE HYDROXIDE ELUENT GENERATOR FOR CAPILLARY LIQUID/ION CHROMATOGRAPHY

Bikash Chouhan

The University of Texas at Arlington, 2020

Supervising Professor: Purnendu K. Dasgupta

The light absorbed by a molecule, except for an efficient fluorophore, is mostly converted into heat, thereby causing a change in temperature. In a liquid flow system, this change in temperature results in changes in the refractive index (RI) and electrical conductivities of the solution. Photothermal measurement of optical absorption (PMOA) most often involves detecting the temperature change indirectly by measuring changes in pressure, RI, or conductivity. In a small-bore capillary, the PMOA detection technique has some distinct advantages: (a) no penalty is paid for smaller path length, (b) there are no stray light issues, and (c) a broadband light source can be used without a monochromator. In our approach, we measured the photothermal effects of optical absorption by measuring temperature change directly rather than measuring temperature-induced RI or conductivity changes. We successfully demonstrated the feasibility of this detector to be useful for liquid chromatography with both macro and micro-sized cells. The baseline standard deviation of the sensor output is 1 m°C. Chapter 2 of the thesis describes the POMA technique in more detail.

Chapter 3 of this thesis describes and compares capillary scale admittance and conductivity detection. It describes five different designs of contact conductivity cells for Open Tubular Ion Chromatography (OTIC). An admittance detector is the first choice for

measurements in small diameter open tubular columns. However, at a suppressed background where the solution resistivity is very high, and the column i.d. is small (< 30 µm), the admittance signal is non-linear with the analyte concentration. Unlike admittance measurements, a contact conductivity detector output is linear up to a concentration of 1 mequiv/L and it is more sensitive at low concentrations in a low specific conductance, fully suppressed background. Here, we report single digit µM LODs for anions like fluoride, chloride, and nitrite.

Alkali hydroxides are more frequently used as eluent in suppressed anion chromatography as the background can be changed to pure water. However, manually prepared hydroxide solutions often contain impurities such as carbonates, chlorides, etc. Further, such solutions absorb CO_2 from air leading to increased carbonate concentration. Chapter 4 of this thesis discusses about hydroxide eluent generator (EG) for open tubular ion chromatography. Such a device has an internal volume of 210 nL and generates a gas-free, pure hydroxide solution online. It is capable of carrying out chromatographic gradient separation at a flow rate of < 200 nL/min without needing any split in the flow. An excellent reproducibility of the EG is apparent from the relative standard deviations of the retention times of the separated peaks (< 0.5 % for isocratic to < 1.2 % for gradient chromatography).

TABLE OF CONTENTS

LIST OF ILLUSTRATIONS

LIST OF TABLES

Chapter 1

INTRODUCTION

The dissertation covers three independent but related projects, all connected to capillary scale open tubular liquid/ion chromatography. The first project is related to the photothermal measurement of optical absorption in a flow-based system. This project, as embodied in chapter 2 of the thesis, is reproduced from the published article:

Chouhan, B., Dasgupta, P. K. Direct Photothermal Measurement of Optical Absorption in a Flow System. *Analytical Chemistry,* **2019**, 91, 2923−2931.

The second project, centered on the topic of admittance and conductance detection in capillary ion chromatography, is discussed in chapter 3 of this thesis. It is reproduced from the published article: Huang, W.; Chouhan, B.; Dasgupta, P. K. Capillary Scale Admittance and Conductance Detection *Analytical Chemistry,* **2018**, 90, 14561−14568.

The third project, mainly focused on designing and building a gas-free, pure hydroxide eluent generator device for open tubular ion chromatography, is presented in chapter 4. It is reproduced from the published article: Chouhan, B.; Shelor, C. P.; Huang, W.; Chen, Y.; Dasgupta, P. K. Nanovolume Gas-Free Hydroxide Eluent Generator for Open Tubular Ion Chromatography *Analytical Chemistry* **2020**, 92, 5561-5568.

1.1 Detection Based on Photothermally Measured Optical Absorption

When an analyte absorbs light energy, unless it has a near-unity quantum efficiency in re-emitting that energy as fluorescence or phosphorescence, the molecule undergoes non-radiative relaxation, resulting in the production of heat. This process of conversion of the absorbed light into heat is called the photothermal effect. So, photothermal measurement of optical absorption (PMOA) is simply a technique of measuring the heat resulting from light absorption. The PMOA technique can measure total energy absorbed directly, unlike optical absorbance detection, where a reduction in transmitted light intensity is measured and is interpreted as an absorbance value. When we consider measuring the total light energy absorbed, the PMOA method has many obvious advantages over conventional absorbance measurement. First, it is not affected by the pathlength of the flow cell. Shorter pathlength results in less energy absorption; but the mass of the liquid that needs to be heated also decreases proportionally, resulting in no difference in the temperature rise as a function of path length. Second, there are no spatial stray light issues: the total energy absorbed by the solution is what matters. Third, any broadband light source can be used. In an illuminated flow-through system, the absorbed light causes the temperature of the solution to rise. A change in temperature directly affects several properties of the solution. Present photothermal absorbance measurement systems detect temperature change by measuring one of these properties.

Photoacoustic spectroscopy (PAS) measures temperature change by measuring pressure changes in a confined volume.[8] A pulsating pressure wave is generated when a pulsed light beam is absorbed. Typically, the frequency is in the audio frequency range and permits the use of a sensitive microphone as the detector. Photoacoustic Spectroscopy is more successful in gas phases as gases are compressible. In photothermal Deflection Spectroscopy (PDS), the absorbed energy is measured by detecting the RI change of the solution.[11] The relative change of RI per degree change in temperature in aqueous solution is ~ 0.01 %, and in an organic solvent is ~ 0.04 %.[15] The PDS technique is the most widely used approach among all photothermal methods, particularly in small-volume measurements involving capillaries. The high sensitivity of this technique comes from the laser source used for excitation; this provides high power with spatial coherence allowing intense illumination of a tiny volume. Photothermal Conductivity Measurement (PCM) technique involves measuring temperature change by measuring viscosity change (~2 % decrease per degree C for water) that manifests itself by a corresponding increase in the electrical conductivity.[14,15]

The techniques mentioned above measure temperature changes indirectly and are not useful for carrying out gradient liquid chromatography. During gradient liquid chromatography, the background RI or viscosity changes due to changes in solvent composition far more than any change due to small temperature changes. Herein, we demonstrated a novel method of directly measuring temperature change. It is important to note that the emphasis is on measuring a small difference in temperature, and not on the absolute accuracy of measuring temperature. We use a single, two-junction thermocouple sensor, which intrinsically measures the differential temperature between the two junctions. The thermocouple was constructed from 25 µm diameter iron and constantan wires, first by twisting the ends together and then welding by the capacitive discharge method. We call this photothermal technique a direct PMOA measurement and used it as a detector in a liquid chromatography system, using both macro and micro volume cells. One of the junctions is placed just before the point of illumination and the second junction immediately after it. The potential difference between the two junctions is directly proportional to the temperature difference between them. This arrangement allows us to measure the rise in temperature when an analyte absorbs light energy while passing through the flow cell. We used both a broadband light source (LED flashlight) and inexpensive focusable lasers (660 nm and 445 nm) as light sources.

We have successfully demonstrated that the detector can be coupled to an HPLC system and used for the detection of separated analytes that absorb visible light. The present baseline standard deviation is 1 m°C. The attainable detection limit for methylene blue, a dye that absorbs strongly at 660 nm, was 30 nM (120 amol in the illuminated volume) using a 19 mW, red laser (660 nm). By comparison with a nonfluorescent dye of the same absorbance at the illumination wavelength it was possible also to determine the quantum efficiency of a fluorescent molecule like methylene blue.

1.2 Admittance and Conductance Detection

Commercially available Ion chromatography systems use a conductometry to monitor when an ionic species passes through the flow cell. With the use of suppressors, the suppressed background conductance is very low and conductometry provides excellent limits of detection. The eluent suppressor is placed ahead of the detector. In anion chromatography with an alkali hydroxide as the eluent, the suppressed background is high purity water. The analyte also emerges with a hydrogen ion as the counter ion from the suppressor; the high mobility of the proton considerably increases the sensitivity of the analyte measurement. In addition to the conducting ion chromatography in the conventional scale, our laboratory has a long history of pursuing ion chromatographic separations in small-bore open capillaries. With the experience of working in various inner diameter tubes and balancing between useful mass transfer properties, available detectors, and the practicability of working, the focus has been on capillaries ranging between 10-30 µm.

The typical flow rates on capillary scale ion chromatography is < 200 nL/min with the sample injection volume as low as 40 pL but typically varying from 1-4 nL. Contact conductivity detection on this platform is difficult to perform as conserving the chromatographic peak efficiency is a challenging task. In a microfabricated platform where the electrodes can be fabricated inside the channel, such detection is more convenient.

Capacitively Coupled Contactless Conductivity Detection[54,55] (C^4D), strictly, admittance measurement is easily deployed from outside the capillary and is very common in capillary electrophoresis. We have been using admittance detection, both using commercially available and laboratory-built detectors on very small i.d. open tubes. However, over a significant range of analyte concentrations, the admittance signal is non-linearly related to the analyte concentration, especially in small-bore suppressed open tubular ion chromatography. Herein, we have carried out a comparative study of an admittance detector to that of different designs of solution contact conductivity detectors. We have tested five different cell configurations for measuring solution conductivity: (a) standard opposed electrodes where the solution flows past two electrodes, the electric field being perpendicular to the flow direction; (b) annular tubular electrodes, where the liquid exits through the central tube; (c) annular ring disk electrodes, where the liquid impinges on the face then flows out through the annulus; (d) bifilar electrodes developed previously in this lab, and (e) planar foil electrodes sandwiching an insulator where the solution flows through a hole drilled through the plane of the electrodes. The first two designs show considerable peak dispersion compared to the other three. The efficiencies of the last three cells are comparable (12000 ± 200 plates/m for chloride). We compare the calibration curves for the admittance and the conductivity cell responses as a function of the analyte concentrations. We recorded the responses in the same chromatographic run with the admittance detector placed immediately after the conductivity cell. The data clearly shows that the conductance signal is linear over the analyte concentration range studied while the admittance signal is not. The dependence of the probe frequency to the admittance response was also studied.

For solution contact conductivity measurement, the present system exhibited concentration LODs of single digit micromolar (mass LODs in double-digit femtomoles) for anions like fluoride, chlorides, and nitrites. Considering that these data were obtained in an environment without temperature control, and by simply connecting the electrodes with unshielded wires to the electronics of a 35-year old commercial detector (Dionex CDM-I, 5 v peak to peak, 3 kHz), a properly designed system should yield much better LODs.

1.3 Nanovolume Eluent Generator

An Eluent Generator (EG) is a device that produces pure eluent online in a directly electrically programmable manner for ion chromatography. In anion chromatography, alkali hydroxides are the preferred eluents, they achieve a background of pure water after a suppressor device.[77] Commercially available hydroxides often contain impurities like carbonates and chlorides. Also, the alkali solution absorbs CO_2 from the air to form increasing amounts of carbonate over time, which alters the retention behavior of the eluent on subsequent runs. Impurities present in the eluent concentrate on the column and elute as a hump on gradient elution. Impurities in the eluent make the suppressed background high. Equally importantly, an eluent generator not only supplies pure hydroxide eluent but also provides the luxury of changing the concentration of the generated hydroxide during a chromatographic run by merely changing the current applied to the device. Hence, a gradient separation is possible without requiring the mechanical mixing of eluents from different reservoirs.

A commercial EG typically uses a reservoir containing 4 M KOH connected to the eluent generation chamber through a stack of cation exchange membranes (CEM).[78] The K^+ ion reservoir is held positive with a platinum anode immersed in it. The K^+ ions penetrate through the CEM and mix with OH^- ions formed at the eluent generation chamber (cathode), thereby forming KOH along with H_2 gas. A separate degassing tube then removes the H_2 gas prior to the injector. The degasser requires significant backpressure for effective removal of the gas and is an essential component of such an EG, designed to operate in the 10 μL/min to mL/min flow regimes.

For an Open Tubular Ion Chromatography, the EG should be capable of operating at a flow rate of ≤ 200 nL/min with short lag and rise times appropriate for gradient chromatography. We present here a Nanovolume Gas-free EG with an internal volume of < 300 nL that does not generate gas and hence does not require any degassing tube, eliminating any extra volume. We constructed the EG within a 1 cm x 1 cm x 0.45 cm microfluidics cross. It is made with a cation exchange membrane on one side and a bipolar membrane (BPM) on the other side of the eluent generation chamber. The EG shows an excellent linearity between the concentration of the KOH generated and the applied constant current. The RSD of the retention times of the separated peaks (≤ 1.2 %) demonstrates the reproducibility of the generator.

Chapter 2

DIRECT PHOTOTHERMAL MEASUREMENT OF OPTICAL ABSORPTION IN A FLOW SYSTEM

2.1 Introduction

Arguably, *transmissiometry* better describes optical absorbance measurement: transmittance is the primary measurand. Excitation from light absorption is typically followed by non-radiative relaxation with the absorbed energy manifesting itself as temperature rise. Photothermal spectroscopies for chemical analysis is the topic of a monograph;[1] a succinct review of the more important photothermal effects is available.[2] Among photothermally measured optical absorption (PMOA) techniques, exploitation of the photoacoustic effect (first used by Bell in his *Photophone*[3]) is preeminent. There are many reviews on photoacoustic spectroscopy (PAS),[4,5] which has now expanded to imaging.[6] While PAS is often the benchmark technique to measure trace gases, flow-through liquid phase adoption is especially susceptible to pulsations.[7] A PAS-based HPLC detector reported in 2008 relied on a pulsed Nd:YAG laser (500 µJ/pulse) and stated a limit of detection (LOD) of 5 µM for Coumarin 440; the chromatogram shown used 10 mM analytes.[8]

Photothermal deflection spectroscopy (PDS) is likely the most commonly used liquid phase PMOA technique. Although the first identification of the thermal lensing phenomenon was carried out with a single laser,[9] a two-laser arrangement is more common.[1,10] In a typical setup, two laser beams are focused in the liquid. The absorption of the “pump” beam from a high fluence laser by the analyte causes a local change in temperature and thence the refractive index (RI); the deflection of the second, “probe” laser beam by the thermal lens thus formed is sensed. Dovichi and his students carried out much of the pioneering studies; demonstrating sub-fmol LODs for derivatized amino acids.[11] Zare's laboratory demonstrated p-p noise levels of 4 x 10^{-8} absorbance units (AU),[12] many others have since demonstrated $\leq 10^{-7}$ AU LODs. Importantly, sensitivity in PDS is highly solvent dependent. Water has a high specific heat (resulting in a smaller Δt for the same heat input), $\Delta RI/\Delta t$ is also small. Thus, while many of the best reported PDS LODs come from nonaqueous media, practical importance is limited.

The Dovichi laboratory also first recognized that rather than RI, it may be advantageous to follow some other property. Viscosity, and hence electrical conductance (G) of a dilute salt solution ($\Delta G/\Delta t$ ~2% /°C), are very sensitive to temperature changes. McLaren and Dovichi focused a 4 mW laser between electrodes 240 μm apart and attained an LOD of 0.2 μM methylene blue (MB) in 0.05 M NaCl flowing therebetween.[13] The authors were prescient in suggesting "electrodeless" conductivity measurement to avoid direct illumination of electrodes; nearly two decades later, the Jorgenson group used capacitively coupled contactless conductivity detection.[14] Sub-μM LODs were possible for dabsyl glucosamine with 200 mW illumination. Later work showed better results with microfabricated Pt electrodes 50 μm apart in a microchannel; an LOD of 0.3 μM was possible (48 mW illuminating a spot <10 μm in dia.).[15] More recently, polyelectrolyte gel electrodes have been shown to work even better.[16]

While all PMOA techniques rely on a temperature change, this is rarely directly measured. A notable exception is the early work by Bard et al., who used a thermistor to measure the temperature rise of strongly absorbing solids or dye solutions upon irradiation with a 2.5 kW Xe source.[17] Subsequent work used a second thermistors in the non-illuminated part as a reference. It was possible to follow oxide or heptyl viologen formation, or Cu deposition on Pt/Au electrodes.[18,19]

We have had a longstanding interest in open tubular liquid/ion chromatography,[20] where detection has been[21] and remains the bottleneck.[22] No HPLC technique can be considered complete without sensitive absorbance detection. Yet, the limitations of a minuscule radial path and Bouguer-Lambert's law makes transmissiometry particularly insensitive. The PMOA approach has especially attractive characteristics for a capillary detection system in that (a) no penalty is paid for a smaller path length *L*; a smaller *L* may result in less light absorption but a proportionally smaller liquid volume needs to be heated, (b) there are no stray light issues, spatially or with respect to wavelength, and (c) a broadband source without a monochromator can be used in an *omni-wavelength* absorbance detector where any absorption in any region will produce a response (we deliberately use this term, as *multi-wavelength* suggests some intrinsic wavelength selection/discrimination capability).

Despite the fact that the power of PMOA now benefits microfluidic devices,[23,24] and numerous flow-through applications are known,[25] there is no commercial detector for liquid phase PMOA. The typical need of using high power lasers (which also limits a given setup to a single wavelength), demanding optical alignment, lack of affordable lasers in the low-UV (primary region of interest in HPLC) all detract from a general-purpose detector. Overmore, typical gradient HPLC involves too large a change in RI and conductivity for traditional PMOA to be applicable. Herein we explore what is possible if one attempts to measure a temperature change precisely by measuring *that*, rather than RI or conductivity.

2.2 Experimental Section

2.2.1 Materials and Auxiliary Equipment.

Suppliers of dyes and methanol is given in the Supporting information (SI). Milli-

Q water was used throughout. All solutions were filtered through 0.45 μm Whatman polyethersulfone membrane filters (www.fishersci.com) prior to use. Thermocouple (TC) wires were obtained from www.omega.com. Absorption Spectra were measured with a HP8453 UV-visible photodiode array spectrometer. LED light spectra were taken with a BWTek *Exemplar Pro* Peltier-cooled CCD array spectrometer. Optical power was measured with a Sper Scientific model 840011 Laser Power Meter; correction factors were applied for the nonuniform sensor response with wavelength. A capacitive arc welder was made from a 5000 μF, 25 V capacitor bank for microwelding, charged to 7-16 V depending on wire size. A Keyence VHX microscope was used for imaging.

2.2.2 Chromatography.

A model 2690 pumping system (1996 vintage, www.waters.com) was used with in conjunction with a 10 μL manual loop injector (www.vici.com) and an Acclaim C18 column (RSLC 120, 2.2 μm, 2.1x100 mm, www.thermofisher.com) that was placed in an external column heater (Eppendorf CH-30, , www.sial.com) kept at 35 °C. The chromatographic flow rate was 0.3 mL/min throughout with 10 μL sample injected. A 500 mm length of coiled stainless steel tubing (178 μm i.d., 12.4 μL volume, put in a serpentine configuration[26] to minimize dispersion), potted in a 50 x 25 x 20 mm block of Field's metal, was placed between the column and the detector for thermal equilibration before it entered the detection cell (described in the next section). When a 100 μm capillary based detection cell was used, flow was split before the cell with appropriate restriction tubes to allow a small portion of the flow to proceed through the detection capillary while the rest was sent to waste. The general arrangement is shown in Figure 2-1. All data were acquired with a 2.5 V full scale Emant 300 DAQ card (www.emant.com, 22-bit @10 Hz) and processed with a 10-point rectangular kernel moving average filter spanning 1 s, with a macro written in MS Excel.

2.2.3 Flow Cell.

The 3 mm path flow cell (illuminated volume ~5.4 µL) was based on a $^{1}/_{16}$ in. i.d., $^{1}/_{8}$ in. o.d. PEEK tube. Two 0.35 mm holes, lengthwise 3 mm apart, were drilled on opposite sides the tube; into these 2 cm lengths of 150/360 μm i.d./o.d. PEEK tubes were forcibly inserted (a ~1.5 mm dia. wire in the cell lumen prevents the I/O tubes from encroaching into the lumen) and epoxied in place to provide liquid I/O. Approximately 1.5 mm from the cell body, a 0.2 mm ϕ hole is drilled through the wall in each of the I/O tubes for placement of the TC sensors. After sensor insertion, a minimum amount of epoxy adhesive is then used to seal off the aperture. During drilling, some inserted member (e.g. a metal wire) must be present in the I/O tube to prevent drilling debris from falling into the lumen and blocking it. Two lengths of 1.5 mm optical fiber (one 12 cm and other 2 cm) with polished ends were inserted through the cell termini, each reaching just up to the proximal I/O tube. The longer fiber serves to bring in light. The shorter fiber was just used as an exit window and can be used for transmissiometry. Some experiments were conducted by making the distal end a reflector; either by silvering or attaching a reflective mylar foil to increase light absorption; the benefits were marginal.

The performance of a smaller cell, a 100 μm i.d., 360 μm o.d. radially illuminated silica capillary, was also investigated. The design is shown in the dashed line enclosure in Figure 2-1. The junctions of the sensor are small enough to be inserted into each end of a 2 cm long capillary (coating removed in illuminated region). The terminal end of 0.005 in. i.d. PVC pump tubing is briefly heated with a heat gun and the softened end is slipped over the silica capillary; it forms a seal when cooled.

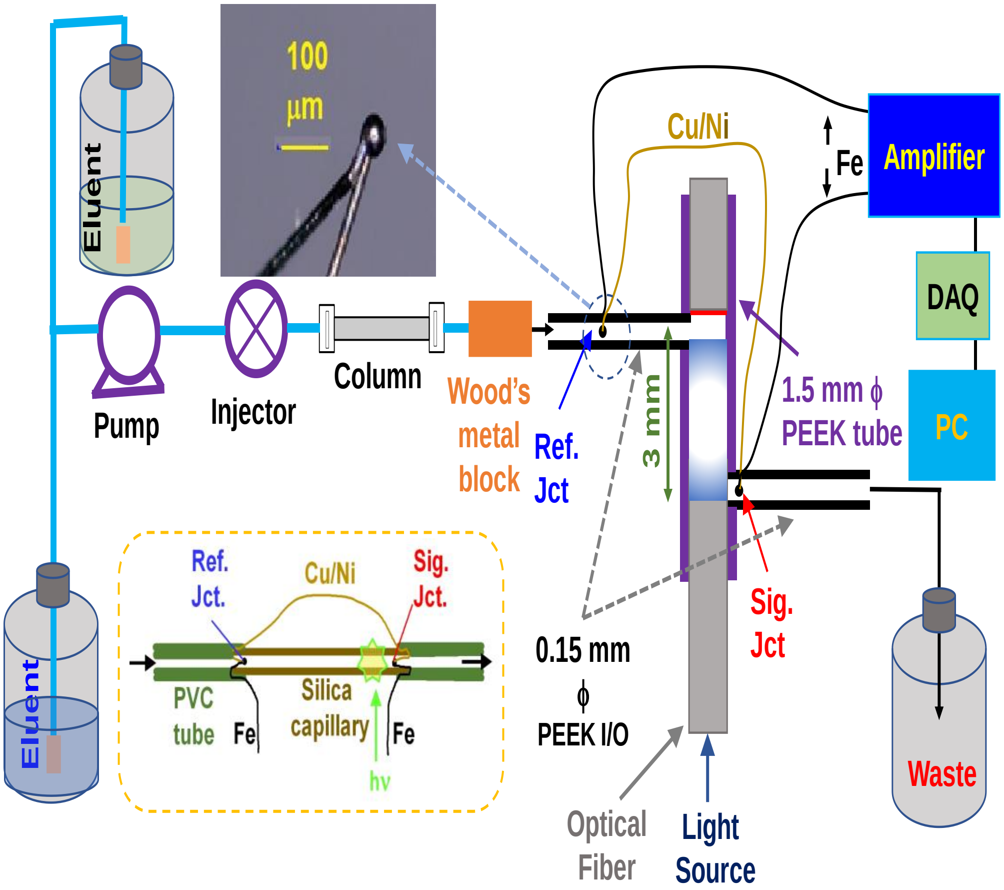

Figure 2-1 HPLC system shown coupled to macroscale PEEK tube cell-based photothermal absorbance detector. Microphotograph of the TC junction is shown in the top left inset. The dashed enclosure shows the construction of a 100 µm ϕ fused silica capillary based cell. A fiber optic coupled white LED flashlight and a laser (449/660 nm) were respectively used as light sources for the PEEK and the silica capillary cell.

2.2.4 Thermocouples.

The ends of iron and constantan (55% Cu, 45% Ni) TC wires (25, and 75 μm) were twisted together and then welded by capacitive discharge; the method is well-known.[27] Except as stated, the results pertain to 25 μm wires. The respective lengths of the iron and constantan legs were ~3.5 and ~4.5 cm (total resistance ~50Ω, the sum of the two iron legs has half the resistance of the constantan portion). A TC made of 250 µm wires (same segment lengths) was also used, the wire tips were just twisted together (welding results in too large a thermal mass at the tip). A similar arrangement is not possible with the 25 µm wires; without being welded, the assembly tip is difficult to insert. Except as stated, rather than the voltage, the short-circuit current generated by the TC pair was measured using the simple one-chip transimpedance amplifier circuit shown in Figure A-S1.

2.2.5 Sensor Calibration.

The absolute response of the TC sensors including the electronics to changes in temperature was determined by enclosing everything in a controlled enclosure at a known temperature to establish a baseline value. Then one junction was put in ice and the signal measured.

2.2.6 Light Sources.

A central hole was drilled into the transparent top of a white LED flashlight (Ozark Trail OT-700L, www.walmart.com). A sleeved acrylic optical fiber that fits tightly in the hole was inserted to be directly atop the emitting region of the LED chip; this end of the fiber was thermally shaped to a larger diameter to gather more light (See Figures A-S2, A-S3). The LED was powered at a constant 6 V (1.4 A). We also used two inexpensive ($30-50) “focusable” (to a spot size of ~0.5 mm) lasers with stated wavelength (power) of

660 nm 50 mW) and 445-450 nm (200 mW), both from www.ebay.com; operational values were measured to be 660 nm (19 mW) and 449 nm (90 mW).

2.2.7 Thermal Loss Measurements.

To ascertain heat loss to the surroundings, the temperature increase was measured for known amounts of heat input as a function of water flow rate. The experiment utilized the cell in Figure 2-2. A slit was made in the wall of a short segment of a 1.5 mm i.d. PVC tube and a precision thin-film 1.0 kΩ resistor (dR/d*t* 5 ppm/°C) was inserted through the slit and the opening sealed by epoxy. PTFE tubes, 0.25/1.6 mm i.d./o.d. were inserted at each end for liquid I/O. Holes (sealed after sensor insertion) drilled in the walls of these tubes accommodated the sensors. The measuring TC junction was 4 mm from the resistor center. Constant voltage pulses (2.00-9.00 V) of 5 s duration (microprocessor controlled MOSFET switch) was applied to the resistor and the corresponding response integrated. In a second similar experiment, a 7 V pulse of 5 s duration was applied to the resistor and the response of TC sensors of different diameters determined.

2.3 Results and Discussion

2.3.1 Why a Thermocouple?

Thermistors and thermocouples are the two most commonly used means to measure temperature; both directly translate a temperature change to an electrical output. TCs are relatively insensitive (best metallic TC sensitivity ~50-60 μV/°C, present sensor 51.7 μV/°C) and they are most commonly used in measuring high temperatures, e.g., in ovens/furnaces. We know of no examples where TCs have been used to measure a small temperature difference, much less at the millidegree scale. However, a TC pair has very low input impedance that should allow high amplification without large input noise. A TC also obligatorily provides a *differential* temperature measurement, uniquely

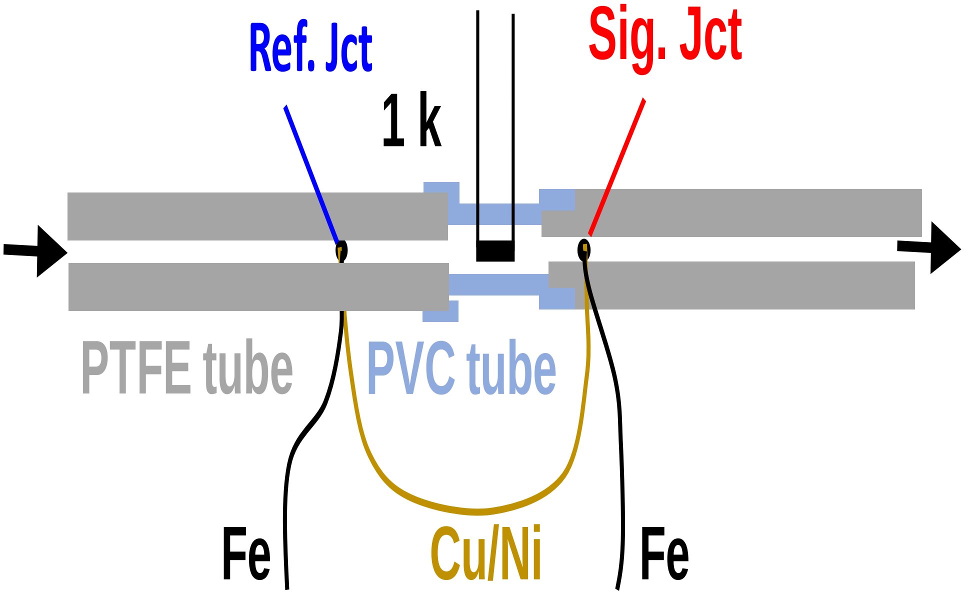

Figure 2-2 Flow cell design for the thermal loss experiment.

useful in the present situation although this aspect is seldom, if ever, of importance in other situations. The primary reason that we opted for a pair of TCs rather than thermistors was size/mass: the smallest available thermistor size was 0.3 mm in diameter. The resulting thermal mass of the sensor was significant and would be likely to affect the measurement both by loading the system and resulting in a slow response time (see below).

2.3.2 Current vs. Voltage Measurement.

Fundamentally, the potential difference between the two junctions of a TC sensor is linearly related to the temperature difference between them, the exact ΔV being dependent on the Seebeck coefficients of the two metals constituting the TC. As long as Δt is the same, ΔV is independent of the dimensions/diameter of the sensor. However, in the case of a transient thermal pulse, a larger sensor with a correspondingly higher thermal mass may not reach the same Δt value as a smaller sensor. If one were to measure the current generated by a TC pair instead, this would simply be the ΔV generated divided by the resistance of the TC assembly. The choice of current or voltage measurement may seem equivalent but in typical deployment to measure temperature, it is the voltage that is measured. A TC is typically used to measure relatively high temperatures, minor variations in the reference junction temperature (often at ambient), may not much matter. For higher accuracy measurements, the reference temperature is independently measured, and any variations corrected for. However, as the temperature changes at the measurement junction, some of the connecting wire beyond the measurement junction may also experience a temperature change, affecting the precise resistance of the connecting cable. If current were measured, this would be affected. For this reason, the measurand is always voltage. However, in other applications, TCs are used as current sources: useful amounts of power are harnessed in radioisotope thermoelectric generators by using a large number of TCs in parallel.[28] We investigated the merits of both current and voltage measurement. The difference was not large, but current measurement in the transimpedance amplification mode was both simpler and produced less noise; this configuration was therefore adopted. We investigated two low bias-current amplifiers (OPA128 and LMP7721), there was no significant difference. The residual noise did not originate in the amplifiers.

2.3.3 Thermocouple Wire Diameter. Response Time.

For the resistor heating experiment, a 7 V 5 s pulse produces sufficient temperature rise for a long enough duration that the maximum response observed from each sensor should not be much affected by the thermal mass of the sensor. The results are shown in Figures A-S4 and A-S5 for the observed current and the generated voltage (inferred from the measured resistance and current). The TC resistance decreases with the square of the wire diameter. As such, the current is expected to increase greatly with the TC diameter: this is observed. The long duration heat pulse essentially reflects steady state conditions: the voltage response displays essentially the same peak maximum regardless of TC diameter. This is particularly notable in that the exact same batch of metal/alloy may not have been used for the different diameter TCs. These data do *not* reflect sensor response times the temporal response speed is limited by how the heat is dissipated by the thin-film resistor. Accordingly, the time constant for the signal to return to baseline as seen in Figure A-S5 is 3-5 s. If this truly reflected response times, such sensors could not be used as chromatographic detectors.

The 75 µm TC was tested both with welded (75_{w}) and twisted (75_{t}) tips (Figure 2-3). The former was further tested with the spherical tip fully in the conduit ($75_{w,\text{fully in}}$) whereas in the other cases, only the surface of the sphere touched the liquid. The 250 µm ϕ TC was tested only in the twisted form (250_{t}) as the welded tip made for too large a thermal mass. Conversely, without a welded tip, the 25 µm ϕ TC was very difficult to manipulate. It is seen that the current signals (solid traces) decrease in the expected order (250 >75> 25 µm; there is ~10^2 x decrease in the TC loop resistance in going from 25 to 250 µm). But the voltage developed (dashed lines, tantamount to measured differential temperature), is the highest for the 25 µm TC (25_w). This clearly shows that the larger sensors extract enough heat from the system to affect the measurement. The response times are independent of whether current or voltage is measured and consistently decrease with decreasing TC diameter. However, if the 75 µm ϕ TC is inserted to a greater depth in the conduit ($75_{w,\text{fully in}}$, thus representing a greater thermal mass), it can have a slower response than even the 250 µm TC. This suggests that the sensor should be in minimal fluid contact. The 10-90% rise times for 25_w, 75_t, 75_w, $75_{w,\text{fully in}}$, and 250_t were, respectively, (n = 3 ea): 0.68±0.02, 0.76±0.03, 0.81±0.05, 1.20±0.08, and 0.89±0.11 s. The differences in the corresponding values for the 90-10% fall times were much more pronounced: 0.93±0.03, 1.78±0.03, 1.43±0.10, 3.20±0.09, and 2.49±0.07 s, respectively. If the rise/fall behavior could truly be represented in exponential terms, the time constant will be 0.455*(10% ↔ 90%) rise/fall times, e.g., 0.31 and 0.42 s for the 25 µm TC.

2.3.4 Noise and Signal to Noise Ratio (SNR).

As we monitor current, it may seem that the larger diameter sensors, which produce much greater current should have greater SNR. In terms of practical utility as a chromatographic detector, this is moot because of the poor response times. In reality, there is no dilemma: the experimental results show that the SNR actually improves with decreasing sensor size. When a 15-s pre-laser pulse baseline span is considered and the standard deviation (STD) computed for the drift-corrected raw data @10 Hz, the peak signal to STD ratio was 950, 750, and 600 for the 25, 75 and 250 µm sensors,

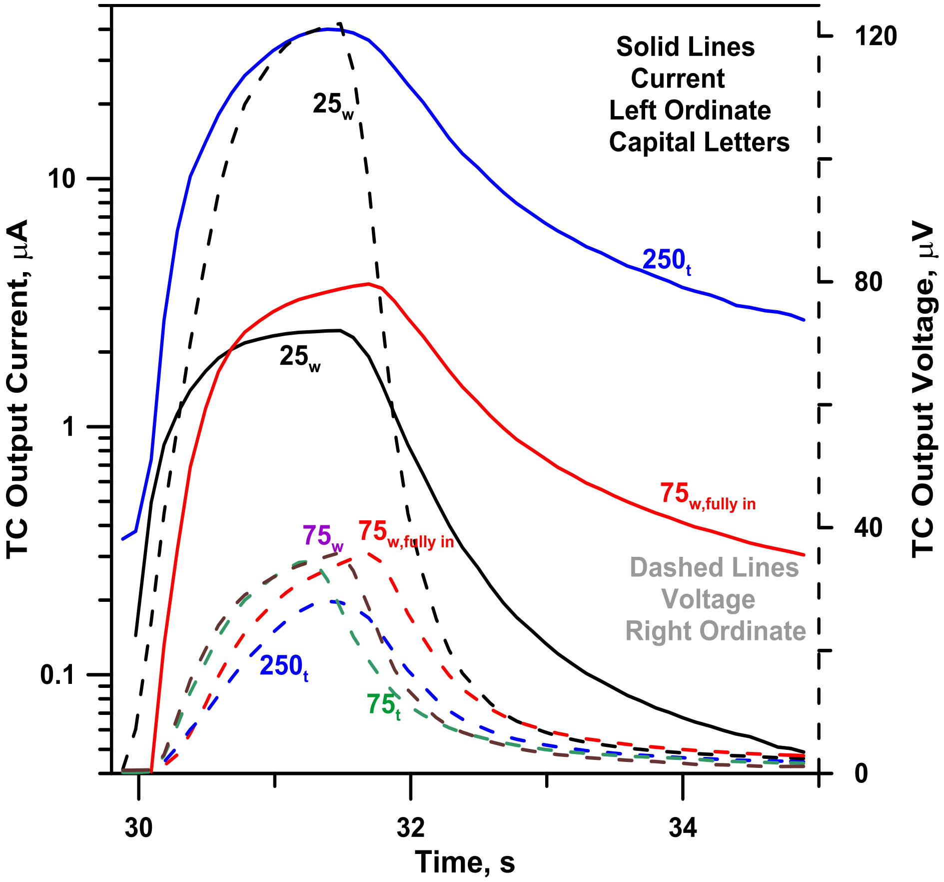

Figure 2-3 Sensor response to a 2 s 660 nm laser pulse illuminating a MB solution flowing at 0.5 mL/min as a function of the TC diameter. The current traces are in solid lines, note logarithmic ordinate scaling. See text for details. The laser pulse was 2.2 s wide for the 75w TC.

respectively (Figure A-S6). This suggests that the absolute value of the current was not a determining factor; the relative noise was approximately the same in all cases. The better SNR for the smaller sensor arises from it minimally affecting the measurement. All further work therefore utilized only the 25 µm sensors. As to going to even smaller sensors, while we found it possible to micro weld 15 µm wires, manual placement in desired locations has proven difficult.

Expressing baseline uncertainty in terms of temperature or absorbance may be more meaningful. For the following results a 10-point moving average filter was applied and in all cases water at ambient temperature was the influent liquid with the Fields metal thermal equilibration block ahead of the cell. For the fiber optic-based cell, at a flow rate of 300 µL/min the STD was 1.1 and 1.6 m°C with the LED off and on, respectively. For a 100 µm capillary at a flow rate of 2 µL/min, the dark noise was the same as above and with either the 660 or the 449 nm laser on, the baseline STD was 1.5 m°C. It is not meaningful to talk in terms of absorbance noise for a broadband source, but we can speak terms calibration with dyes with absorption maxima near the specified laser wavelengths. The baseline STDs in the capillary cell were 5 and 4 µAU at 449 and 660 nm, respectively, @ 2 µL/min.

2.3.5 How Much Heat is Lost?

Ideally one would like to monitor the temperature at the point of illumination (PoI) but this is not possible because light absorption by the signal junction (SJ) of the sensor itself causes a large background. Moving SJ far away from the PoI, however, reduces the signal due to thermal loss to walls/surroundings. The success of the technique will depend in part on majority of the heat generated remaining in the liquid *en route* to the SJ, rather than being lost to the walls. It is thus useful to determine the fraction of the heat input to the system that is registered by the sensors. This experiment is much easier to perform with a conventional resistance heater rather than a laser pulse because of the difficulty in ascertaining the exact amount of energy in a laser pulse that is actually absorbed by the solution. Voltage pulses (2.00- 9.00 V) were thus applied to the resistor in Figure 2-2. The sensor outputs are shown in Figures A-S7. Although a PVC rather than a PEEK tube was used for the convenience of inserting the resistor, tube i.d. was the same. The distance of SJ from the resistor was the same as the distance between SJ and the light input fiber in Figure 2-1.

The input heat (J) is computed as $t_{pulse}*V^2/R$. The recovered heat in Joules was computed from the peak area (A) in a plot of time (min) vs. ΔT (in millidegrees C) as $4.18\text{x } 10^{-3}\ AF\rho$, where the numerical term is the conversion factor for mcal to J, F is the flow rate (mL/min) and ρ is the density of water. Results for experiments conducted at four different flow rates and eight different voltages are shown in Figure A-S8. At each flow rate, the recovered heat signal was linearly related (r^2 0.9978-0.9998) to the input heat with intercepts that were statistically indistinguishable from zero. The respective slopes (equaling the fraction recovered) were 0.70, 0.77, 0.82_5, and 0.88 at flow rates of 0.2, 0.3, 0.4, and 0.5 mL/min. At the chromatographic flow rate of 0.3 mL/min used with the fiber optic cell, >75% of the heat produced is sensed. A plot of the fraction of the heat lost against 1/F suggests that the heat will be almost quantitatively retained by the liquid at $F \gtrapprox 1$ mL/min. (Fig. A-S9).

It is instructive to consider how the heat loss for a situation involving heating by an absorbed beam of light may differ. For a radially illuminated capillary, when the solution is poorly absorbing, there is little attenuation of light during the radial passage, resulting in radially uniform heat generation. However, as the flow velocity at the boundary layer is lower, the temperature at the wall is expected to be slightly higher than the center. This should reduce heat loss of the core solution to the wall.

2.3.6 Differential Measurement Configuration Provides Noise Immunity to Ambient Temperature Change.

Our arrangement measures the difference in temperature between two closely spaced locations. The approximate transit time between the sensing locations is 2.4 and 1.1 s in the capillary and the macro cell, at flow rates of 4 and 300 µL/min (linear velocities of 8.5 and 2.8 mm/s), respectively. Changes in ambient temperature are typically much slower than this time scale and thus not likely to have an effect on baseline noise. Figure 2-4 illustrates this. It can be seen from the red trace that when a long (180 s) 4 V pulse is applied to the system of Figure 2-2 @0.3 mL/min, the temperature rises almost immediately, reaching a plateau of ~460 m°C in ~30 s. If the system of Figure 2-2 is now changed such that the resistor is upstream of both sensor junctions (Figure A-S10) and a similar heat pulse applied, the system response is vastly attenuated, reaching maximum amplitudes of ~-85 to +55 m°C, and these only take place during the rising and falling edges of the upstream heat pulse. During the plateau of the pulse, baseline remains approximately flat, displaying no more noise than the pre-pulse baseline. The baseline does display a lower value than the original, indicating the extent of heat loss between the two sensing junctions.

2.3.7 Utility as an Omni-Wavelength Chromatographic Detector.

Absorption of any portion of a broadband incident light by an analyte results in a thermal signal; in a traditional transmission photometry system, such a signal may be swamped by light at other wavelengths. The emission spectrum of the white LED used is shown in Fig. A-S11. Under operating conditions, when read by a power meter, the power at the distal end of the coupled fiber measured 28.3 mW equivalent @ 633 nm, multiplying the LED emission matrix and the PD wavelength response matrix (Fig. A-S11), the actual power was computed to be 46.2 mW (Details are given in the SI file, ac18050913si_002.xlsx). Chromatograms with this white LED source for the separation of several dyes are shown in Figures 2.5a and 2.6. Absorption spectra of the various dyes superimposed on the LED emission spectra are shown in Figure A-S12. Figure 2-5b shows separation and detection of two yellow dyes with 449 nm laser illumination. The injected concentration is 187 µM: the peak volume represents 8.1 pmol tartrazine; the S/N=3 LOD is 3.9 µM, or 170 fmol (90 pg) injected. However, judged by the injection volume and the peak volume, at the apex, the original sample has been diluted ~38x. The actual peak concentration at the LOD will be 100 nM. The laser spot is 0.5 mm in diameter, illuminating a volume of ~3.9 nL, at the LOD there is ~400 fmol (0.2 pg) analyte in the illuminated volume. This is borne out by a large volume injection in the flow injection mode that obviates dilution; injection of an 18.7 µM Tartrazine sample produces a S/N of 600 (Figure A-S13). A similar injection was conducted with 3.1 µM (1 mg/L) MB using the 660 nm Laser. In this case the calculated LOD based on a S/N=3 was ~30 nM. Given the laser spot and the capillary dimensions, note that at a maximum, ~25% of the laser beam actually illuminates the solution. Even for an isocratic run, unless the sample is precisely in the same solvent as the chromatographic eluent, there will be a significant initial base line disturbance. As seen in Fig. 2-6, in a gradient run, the baseline change as the gradient is executed can be even greater. Consider the factors that can contribute to this change in baseline: (a) change in solvent absorption (no solvent is truly transparent), (b) change in solvent refractive index and the resulting change in Fresnel reflection loss at the window (fiber optic)-liquid interface, and (c) change in the solvent heat capacity. An increase in solvent absorption or RI and/or a decrease in specific heat will result in an increase in the baseline.

Let us assume that the small concentration of ammonium acetate present has

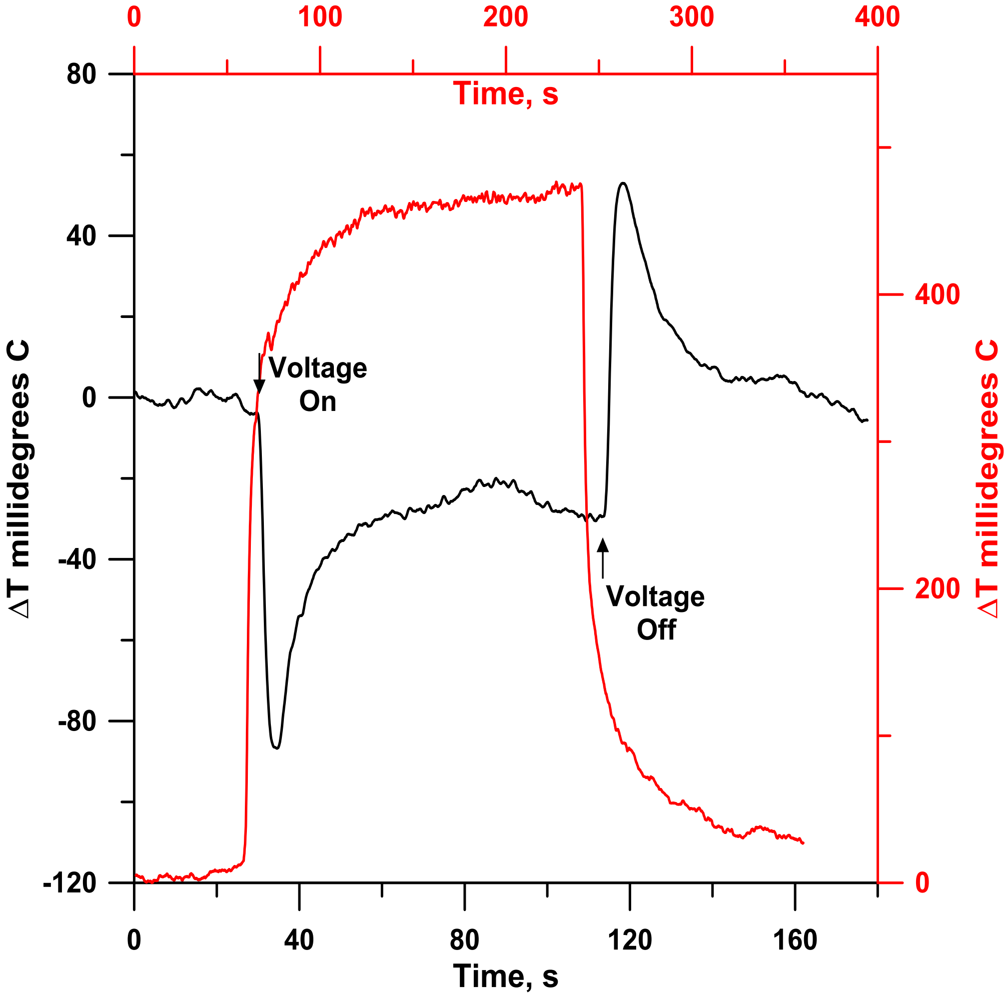

Figure 2-4 Red trace (top abscissa, right ordinate): Response to a 4 V 180s pulse in the system of Figure 2. Black trace (bottom abscissa, left ordinate): Same experiment with a 90 s pulse with the heater upstream of both sensors.

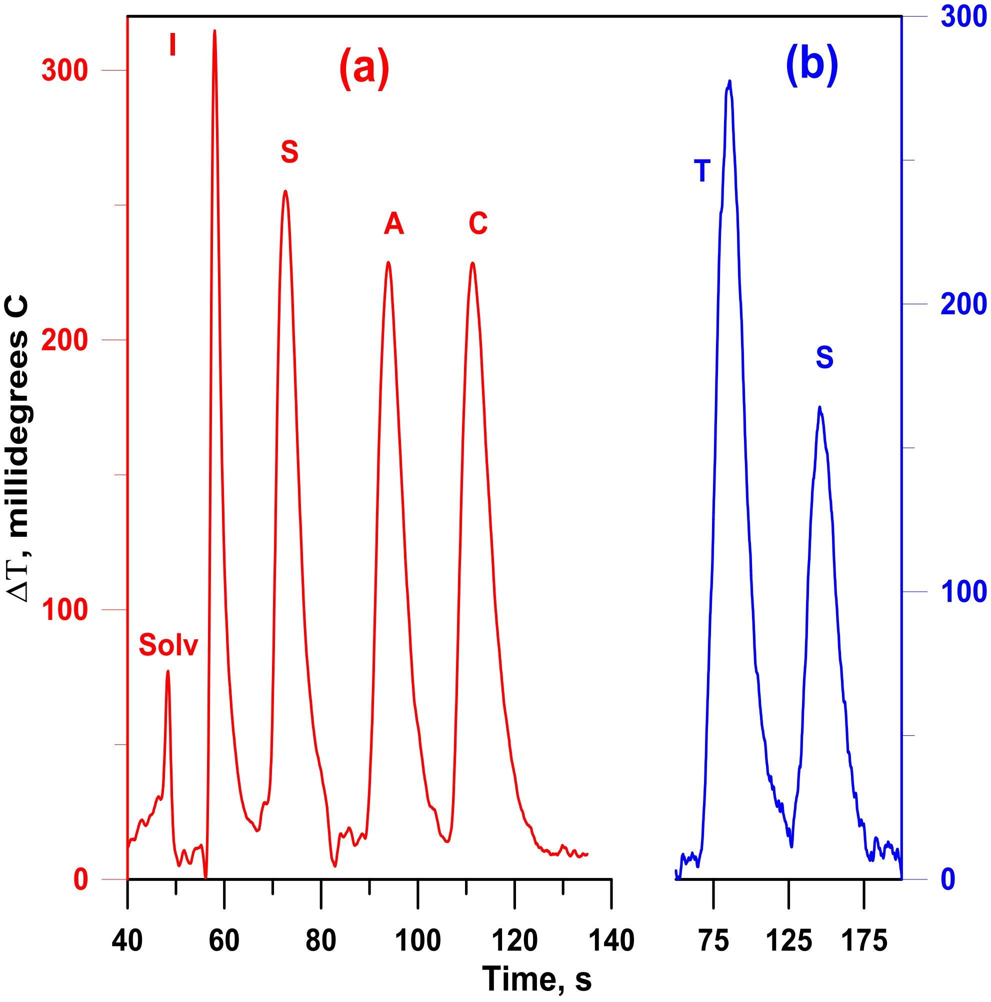

Figure 2-5 Isocratic separation of dyes. Solvents A: 20 mM NH_4OAc; B: MeOH. (a) LED illuminated 1. 5 mm ϕ, 3 mm cell, 62% A, 38% B. Solv: Solvent front; I: Indigo carmine; S: Sunset yellow; A: Allura red; C: Chromotrope 2R, 30 µg/mL ea., 300 µL/min (b) 449 nm laser illuminated 100 µm i.d. capillary, same conditions as in (a), 4.4 µL/min of the column effluent directed through the capillary cell. T: Tartrazine, dye concentrations 100 µg/mL each.

negligible parameters on these parameters a – c and we can assume that the situation is adequately represented by just water-methanol mixtures. From literature data on the RI of methanol-water solutions,[29] we have considered the range of 11.4 to 63.7 % v/v methanol (this compilation does not have data specifically for 15 and 60% v/v methanol but obviously encompasses the range of interest and includes seven other discrete intermediate compositions. Details appear in the SI file (ac18050913si_003.xlsx). The RI of the eluent was assumed to be independent of wavelength. The RI of the PMMA fiber optic was computed from an equation given by Beadie et al.[30] The change in the total energy entering the cell as modified by the Fresnel loss (dependent on both the RI of the eluent and the PMMA fiber optic) was then computed for each 0.5 nm wavelength bin based on the LED intensity distribution (Figure A-S11) and summed. Based on water and methanol absorptivity data made available to us (Figure A-S14, courtesy Karsten Kraiczek, Agilent Technologies), the relative change in the absorbed light, taking into account the varying Fresnel loss, in going from 11.4 to 63.7 % methanol changed by 19%. Compared to this, the specific heat of the liquid in traversing the same increase in methanol content decreases by 37%.[31] This would lead to 58% greater temperature rise, even if the same energy was absorbed. The change in the baseline is thus dominantly due to the change in specific heat of the eluent.

The RI of the solvent changes by >0.007 units in going from 15% to 60% methanol. With this degree of RI change, it will be difficult, if not impossible, to adapt gradient elution with ΔRI as a measurand. Conductometry will be similarly affected by solvent viscosity changes, even without considering changes in salinity that generally accompanies a gradient. The methanol-water system, where viscosity not only changes greatly as a function of composition, but also the change is not monotonic, presents a particular challenge for photothermal conductometry. In contrast, the present

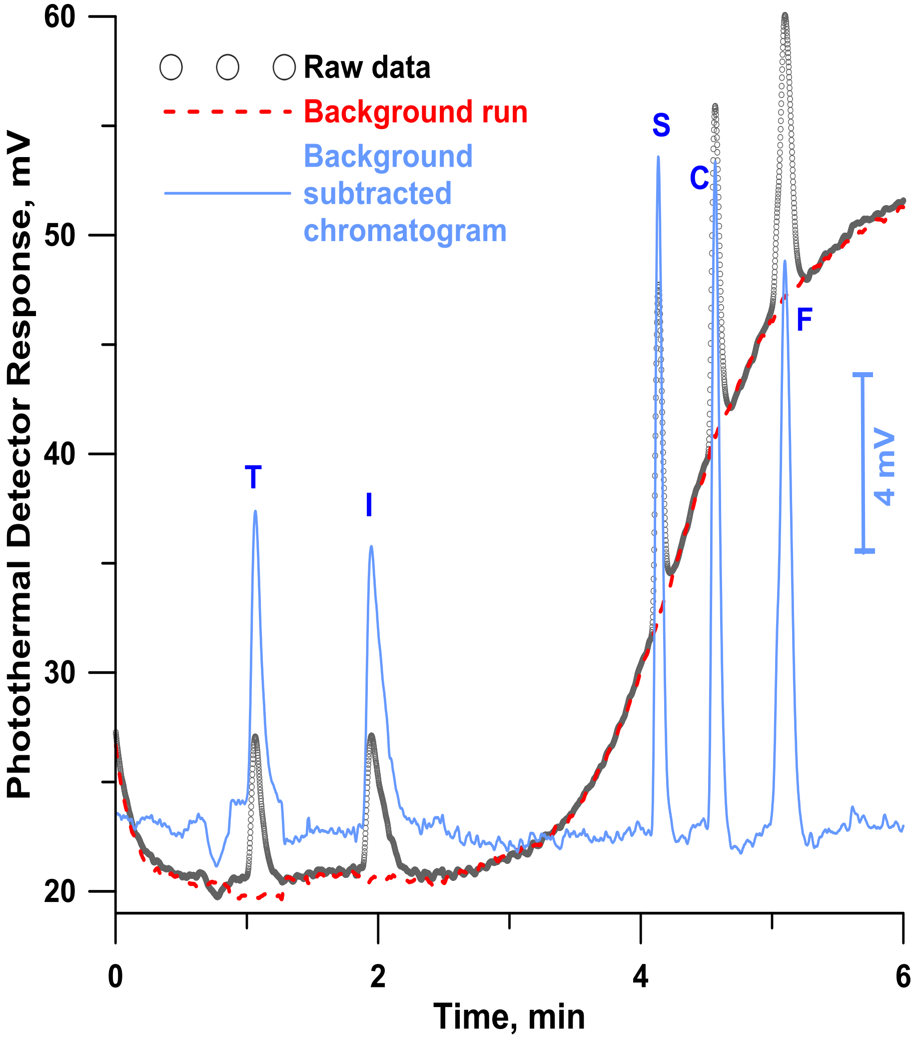

Figure 2-6 Gradient separation: 85% A:15% B to 40% A: 60% B, linear ramp begins at t =0 and ends in 1 min, dyes 100 mg/L. T: Tartrazine. F: Fast green FCF. Others as in Fig. 2.5a

baseline rise, while not negligible, is highly reproducible to allow background subtraction. Admittedly, the presently attainable sensitivity with LED illumination is not competitive with respect to extant photothermal approaches, or even conventional UV-Vis absorbance detectors. Unlike high intensity lasers focused on very small volumes, only a small portion of the broadband LED emission is absorbed by any analyte.

2.3.8 Signal-Concentration Relationship.

As is well known, the photothermal signal is proportional to the absorptance, given as (1 - *T*) where *T* is the transmittance. As such, if *P* is the total power available for absorption, the signal *S* would be given as, (*k* being the relevant absorptivity constant for the choice of the unit of concentration *C*):

$$S = P(1 - T) = = P(1 - 10^{-A}) = P(1 - 10^{-kC}) \quad \ldots(1)$$

In Figure 2-7, it is readily seen that the relationship between the observed peak area and the concentration is not linear for any of the dyes (dashed lines) over a large range; whereas they fit eq 1 with respective r^2 values of 0.9995, 0.9952, 0.9970, and 0.9985 for the dyes C, I, S, and A (see Figure 2-4 for names), the respective best fit values for *P* (with *k* given in parentheses) were: 334 (4.49×10^{-3}), 120 (8.44×10^{-3}), 200 (6.95×10^{-3}) and 290 (4.66×10^{-3}) for the 4 dyes. It is to be noted that as a broadband source is used, the values of *k* (effective absorptivities) and *P* (power effectively available for absorption) are both dependent on both the source intensity distribution and analyte absorption characteristics. As such, baseline noise cannot be specified in terms of absorbance without reference to an analyte. However, the noise/uncertainty can be specified in terms of temperature as previously enumerated.

2.4 Illustrative Application. Quantum Efficiency (QE) and the Methylene Blue Dimerization Equilibrium.

A demonstrable virtue of the present PMOA configuration utilizing direct thermometry is the straightforward demonstration of heat production resulting from light absorption. And when it does not do so completely, as for a fluorescent molecule, the degree of inefficiency provides a quantitative estimate of the fluorescence quantum yield.[32] Fluorescence quantum yields have long been determined from absolute calorimetric measurements.[33] Carried out in static systems; this requires excellent thermal insulation in the form of a Dewar-based absorption cell. It would be possible to adapt this to the present flow-through system in a square or rectangular flow-through cell that has a window large enough to accommodate the entirety of a laser beam of known power. With the blank solvent as a control and a photodiode to determine the transmittance, the temperature rise can provide a direct calorimetric measurement of the quantum efficiency, effectively defined here as the fraction of the absorbed photons that did not produce heat. However, a much simpler alternative is to use a reference non-fluorescent compound R, which absorbs at the same wavelength as the fluorescent compound A of interest.[32,34] If for example one takes a solution each of A and R of the same absorbance at the irradiation wavelength, the relatively lower temperature rise of A compared to R provides the measure for the QE of A.

The optical and equilibrium properties of MB is of interest in a great variety of applications.[35] Methylene blue absorbs broadly around 660 nm and emits around 690 nm, however, in solutions containing dissolved O_2, the major process involves deexcitation to produce singlet oxygen ($^1\Delta$ O_2): irradiation of MB is one of the most common ways to generate $^1\Delta$ O_2.[36] The quantum efficiency of MB is often listed as 0.52; this is actually the efficiency with which $^1\Delta$ O_2 is generated in methanolic medium; the QE for the process in dilute aqueous solution is ~0.56.[36] When ~690 nm photon emission is taken into account, the overall QE will be somewhat higher but an exact value

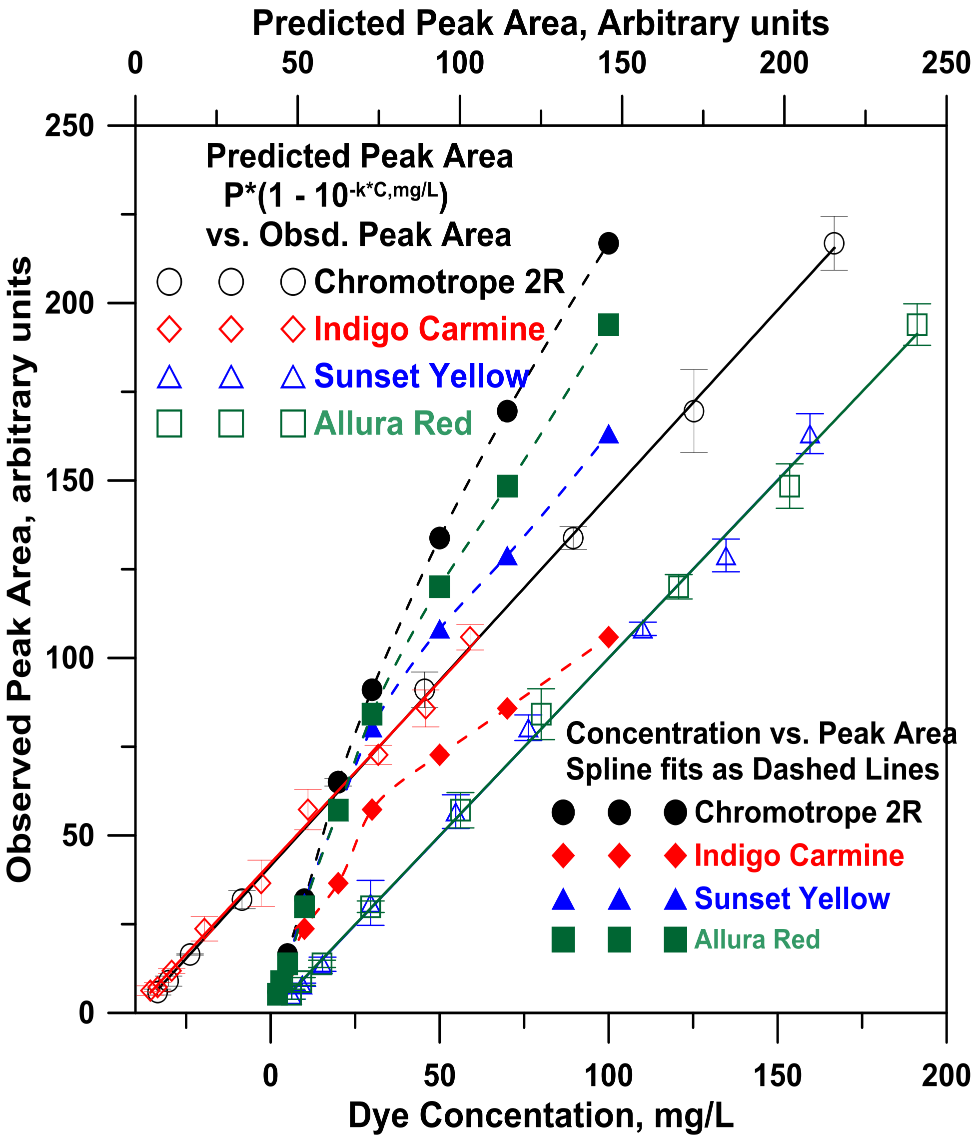

Figure 2-7 Peak area signal (Figure 4) vs. concentration (filled symbols, dashed lines). Fits according to eq 1 (open symbols, solid lines indicating linear fits). The error bars reflect ±1 standard deviation.

is not available in the literature. The observed QE of MB is not only solvent dependent, it is also concentration dependent; this is understandable because MB rather easily forms a dimer (this also is not without controversy[37]). The QE for the dimer is likely zero or very low due to intramolecular energy transfer. The equilibrium constant for dimerization (KD) is temperature, solvent and ionic strength dependent. The values of log KD (all in pure water except as stated) has been variously reported to be 3.60 (20 °C),38 3.85 (24°C, I = 0.0086 M with NaCl),39 3.84 (24°C , I = 0.0086 M with Na2SO4),39 3.54 (27°C),40 4.31 (60 µM MB, 25 °C),41 4.04 (30 µM MB, 25 °C),42 and 3.38 (30 °C, I ~ 0),43 cited in chronological order and all determined by spectrophotometry, based on spectral differences of the monomer vs. the dimer.

We chose alkaline Bromthymol blue (BTB) as the reference nonfluorescent analyte. Although the absorption maximum for BTB is at a lower wavelength (615 nm), the laser linewidth is narrow and permits a linear concentration-absorbance relationship. Figure 8 shows the photothermal response behavior of a BTB and a MB solution that has the same absorbance at 660 nm. The inset shows the concentration-photothermal response behavior of the two solutes: while that for BTB is linear, that for MB increases with increasing concentration – as more dimer is formed, the effective QE (QE_{eff}) decreases and heating increases.

The response behavior is easily modeled: if the total analytical concentration of MB is C, the monomer concentration C_m is given by :

$C_m = ((1 + *8K_DC)^{0.5} -1)/4K_D$… (2)

and if the QE of the dimer is taken as zero, QE_{eff} is given by:

$QE_{eff} = QE_m/(1 + 2K_DC_m)$ …(3)

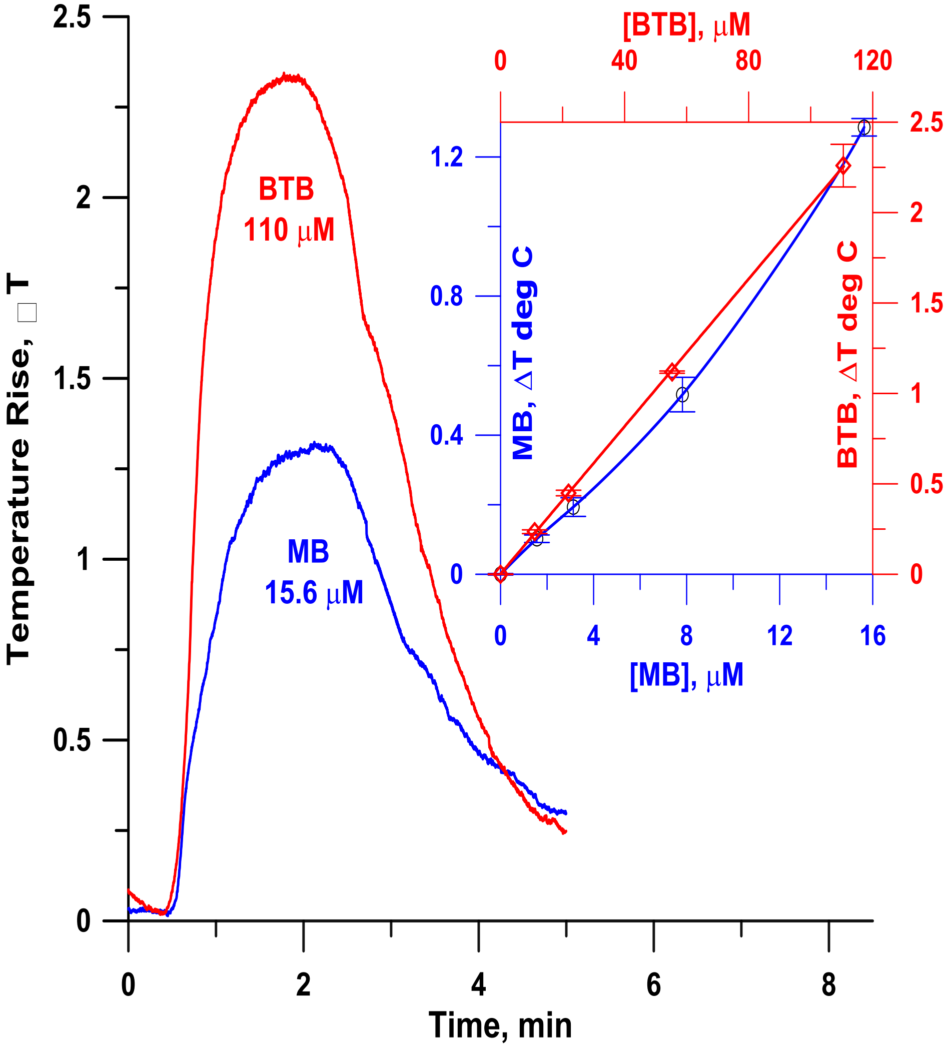

Figure 2-8 Large volume (4.9 µL) injections of bromthymol blue (BTB] and MB. Flow rate: 5 µL/min. Inset shows photothermal response curves, linear for BTB (r^2 1.0000).

where QE_m is the quantum efficiency of the monomer. We determined QE_{eff} at four different concentrations of MB and BTB (Table S1); the best fit values for log K_D and QE_m were determined to be 4.06 ± 0.32 and 0.609 ± 0.035 (Fig. 2-9), very much in the range of what would be anticipated from the literature.

2.5 Conclusion

We have explored the performance of an inexpensive easy-to-construct PMOA system that relies on direct thermometry and can function as an omni-wavelength detector with a white LED source, or can be operated at fixed wavelengths with other inexpensive solid-state sources. We demonstrate its performance in a LC system. While baseline shift in gradient elution is not eliminated, direct thermometry produces manageable and correctable baseline shifts compared to RI or conductivity measurements. With low-cost solid-state lasers, even with their poor ability to focus to a small spot, double digit nM LODs for strongly absorbing dyes are possible and this is readily demonstrated, even without beam modulation and lock-in amplification.

The white LED source HPLC detector, while not competitive in noise performance with commercial detectors, uniquely provides broadband detection. White LEDs differ considerably in their emission characteristics depending on the nature of the phosphor used;[44] some may be more suitable for use than others for a specific analyte. While any present whited LED is obviously unable to provide UV detection, much higher power laser-driven light sources that span the entire UV-visible range and has a small 100-200 µm source diameter are available.[45] In terms of further reducing the sensor size, it is obvious that we are near the limit of what can be done by making wires with thermocouples and manually placing them. Microfabrication of the sensors in a channel is the next logical step and may provide a simple way to perform absorbance

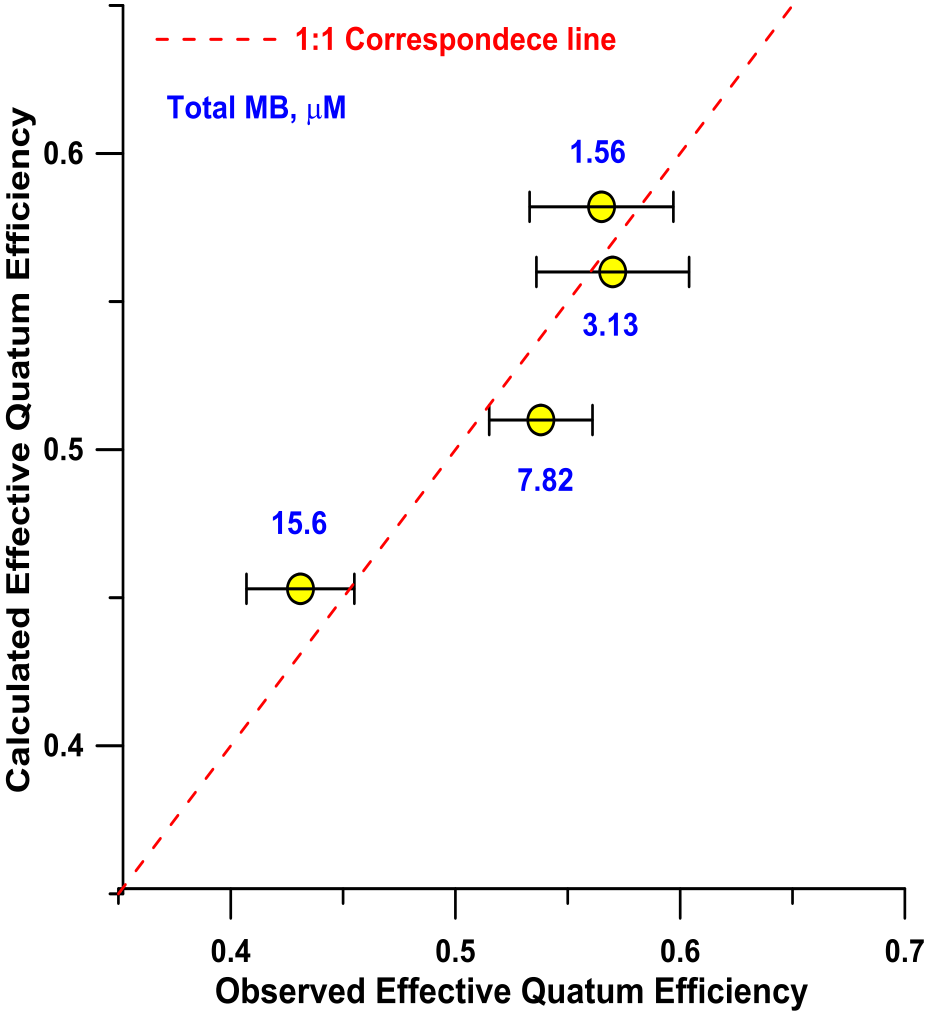

Figure 2-9 The observed vs. model (eq 3) predicted effective quantum efficiencies. The best fit values are $QE_m = 0.609$, and $K_D = 1.15 \times 10^4$ M^{-1}.

measurements with reasonable sensitivity even in very small path lengths. With better thermostating, sensor miniaturization and electronic improvements, an order of magnitude improvement in noise levels to ~0.1 m °C would seem to be feasible; the performance level necessary for the technique to be competitive with present commercial HPLC absorbance detectors, without resorting to exotic light sources.

It may be argued that the core of this paper is simply a flow-through microcalorimeter that may be of utility in applications that have nothing to do with light, much less absorbance measurements. Virtually any reaction involves a thermal change. Fast reactions that involve a significant thermal change can be exploited in the postcolumn mode for analyte detection. On the other hand, the rate of reactions that are not as fast may be followed by a flow-over sensor array, which can be of great value in situations where optical monitoring is not possible.

Chapter 3

CAPILLARY SCALE ADMITTANCE AND CONDUCTANCE DETECTION

3.1 Introduction

Conductivity measurement has a long and illustrious history. In 1776, Cavendish reported the relative conductance of different solutions to the Royal Society.[46] What is remarkable is that this was two decades before Volta described his pile, so that only static electricity was available to him. Cavendish compared conductivities of two solutions, each placed in a long tube, and one terminus of each connected to a battery of Leyden jars. The other end of each tube was connected to a wire, at least one of which could be inserted to different depths. He then proceeded to touch the wires in turn with one hand, the other touching the other terminal of the Leyden jar battery. When he received the same level of electric shock, the conductance ratio of the solutions in each tube was reciprocally related to the depth of the solution separating the wire electrode(s). Small has traced the evolution of conductometric detection in the context of the historical development of ion chromatography (IC).[47] A conductivity detector is the preferred choice in IC because ions uniquely affect the electrical conductivity of a solution. A flow-through cell is used to continuously monitor the conductivity. With reference to the current practice of anion chromatography, the background conductance and hence the noise level are lowered with an “eluent suppressor” placed before the conductivity cell. This makes the system selective for anions derived from acids of low to moderate pKa, enhancing the analyte signal and simultaneously reducing the background. It is possible to carry out IC without a suppressor: if the eluent ion has strong affinity for the stationary phase, a relatively low eluent concentration suffices, and the background conductance can be acceptably low. A further requirement for the eluent ion in this case is to have a mobility sufficiently different from those of the analyte ions of interest: the conductivity signal is generated by the difference in equivalent conductance between those of the analyte and the eluent anion.[48]

In solution conductometry, all possible combinations of two and four-electrode cells and alternating current/direct current (ac/dc) measurement modes have been reported.[49−53] In a fourelectrode design, a constant voltage or current is applied between the two outer electrodes, and the resulting current or voltage between the two inner electrodes is respectively measured.[51] The four-electrode approach minimizes detection probe polarization and avoids electrolysis at the detection electrodes, in principle providing greater measurement accuracy.[53] However, a two-electrode design is mechanically and electronically simpler and is more common.[48,50] The bipolar pulse technique (BPT) was introduced in 1970 to avoid the effects of cell/double layer capacitance.[50] Consecutive constant voltage square wave pulses of short duration, of equal magnitude but opposite polarity are applied to the electrodes; current is measured at the end of the second pulse. BPT provides fast measurements accurate to within 0.01% over a 4 orders of magnitude cell resistance range (102−106 Ω), independent of the cell/double-layer capacitance. It is presently the dominant approach to solution conductometry.

For the detection in capillary scale systems, in 1998 Zemann et al.[54] and da Silva and do Lago[55] near-simultaneously introduced an on-column detection technique that has since become known as a "capacitively coupled contactless conductivity detector (C4D)" and has enjoyed widespread use, especially in capillary electrophoresis (CE). The nomenclature is unfortunate: (a) while the electrodes are not in contact with the solution, they are certainly in contact with the outer walls of the conduit containing the electrolyte and (b) the arrangement really measures the admittance between the electrodes, a complex function of the contribution of the wall capacitance, stray interelectrode capacitance, solution capacitance, and solution conductance. Regardless, aside from its simplicity and inexpensive construction, C4D represents a noninvasive monitoring technique with no possibility of electrode deterioration/fouling or flow disturbance. Facile and repeatable movement of the detector along a column easily lends itself to imaging.[56] However, because of the capacitive components, the relationship of the detector output signal and the specific conductance (σ) of the solution is nonlinear over any significant range of σ and, in extreme cases, may not even be a single-valued function of σ.[57,58] Without delving into detailed modeling, it will be appreciated that the capacitance between the transmitter electrode and the solution, that between the solution and the receiver electrode, and the interelectrode capacitance together represent a fixed impedance at a fixed frequency (f). The solution impedance is in series with this; the overall current will linearly vary with the solution impedance only if the fixed impedance from the wall/ electrode etc. is negligible in comparison. A high f value decreases the fixed impedance but has relatively little or no effect on the resistive current through the solution. Thus, the best conditions for a linear relationship of the detector output and σ is a combination of high f and high σ. At low σ, however, the solution impedance is governed by both σ and the dielectric constant D. Starting from pure water, initially D either does not change or decreases in a minor fashion with increasing σ.[59] Only at relatively high σ does D finally begin to increase. At low σ and high f, the current through the solution is dominantly capacitive and does not significantly change with changing σ: i.e., it does not function as a conductivity detector. At low f, the current through the solution will be dominantly resistive and the detector will respond to changes in σ but, because the wall/electrode fixed impedance may be significant, the detector output is not likely to be linear with changes in σ. In addition, at low f, as the wall impedance is higher, less energy is coupled into and out of the solution, and despite careful design, sensitivity limitations arise. The above may uniquely be a problem in suppressed ion chromatography (IC) where the background is essentially deionized (DI) water:[60,61] to put matters in perspective, the resistance between two 25 μm diameter disk electrodes separated by a 500 μm layer of DI water is ~180 GΩ.

It is known that, with electrodes in direct solution contact, conductance changes linearly with electrolyte concentrations ranging from the limit of detection (LOD, sub-micromolar) to low millimolar levels. The measured value is not particularly frequency dependent except possibly at relatively high frequencies (≥200 kHz).[62] Attempts have been made to design a capillary scale solution contact conductivity (hereinafter contact conductivity) detector, mostly by Zare's group: Huang et al.[63] used a CO2 laser to drill 40 μm holes radially across 50−75 μm i.d. fused-silica capillaries and cemented 25 μm Pt wire electrodes therein. This is difficult: the group subsequently reported an end-column design where one wire was inserted at one end of the capillary and sealed. A single hole was drilled through the capillary wall just above where this wire terminated inside the capillary. This hole served as both the entrance for the second electrode and the liquid exit.[64] Later in 1998, Zhao et al.[65] simply placed a 25−50 μm diameter insulated wire across the face of a 75 μm i.d. capillary and affixed it by epoxy adhesive on each side. The wire was then cut where it passed across the capillary bore. While simple, a comparison with previous designs would indicate significantly poorer performance.

In 1993 Dasgupta and Bao[66] introduced suppressed conductivity detection in CE. They used a 100 μm Pt wire as one electrode deployed across the mouth of the capillary, and the second electrode was placed as close to it as possible in parallel configuration, without touching the first. A superior arrangement was shortly advanced in the form of bifilar wire end-column electrodes.[67] Even though a pair of 80 μm diameter Ni wires (+19 μm of insulation) were used (placed at the capillary exit with the wires following each other in the flow direction), very good peak shapes were observed. For a 75 μm i.d. capillary, assuming the flow stream passing across the electrodes remained constrained to the capillary exit diameter, the authors computed the detection volume to be ∼185 pL. The only commercially introduced capillary scale conductivity measurement cell utilized a ring disk geometry in a wall-jet configuration: the center electrode (150 μm Pt wire) was separated from a stainless-steel ring electrode by epoxy insulation.[68]

Contact conductometry have been frequently used on the chip scale.[69] Arguably, conductometry in standard capillaries on the same scale is more difficult; there are no comparable opportunities for fabricating electrodes in situ. The difficulty of constructing the cell and keeping the dispersion adequately small increases exponentially with decreasing diameter. Laser drilling technology has advanced greatly in the intervening years. Still, commercial laser drilling firms report that drilling 25 μm holes in 25 μm i.d. polymer capillaries without lumen blockage by the debris is extraordinarily difficult. Herein we compare several relatively simple end-column contact cell designs and compare them to admittance detection.

3.2 Experimental Section

Materials and Reagents. Tungsten wire (50, 75, and 100 μm diameter; www.alfa.com), 45 μm diameter insulated copper wire and bifilar copper wire (25 μm diameter each strand, both from www.mwswire.com), and stainless steel (SS) tubing (type 304; www.vitaneedle.com) of different diameters were used as electrodes. Tubing used included PEEK (75 μm i.d., 360 μm o.d.; 380 μm i.d., 0.025 in. o.d.; www.idex-hs.com), various small-bore PTFE tubes (www.zeus.com), and silica capillaries (20/25/75 μm i.d., ∼365 μm o.d.; www.molex.com). Micro drill bits were obtained from www.eternaltools.com.

The capillary suppressor was made of a Nafion perfluorosulfonate cation exchanger polymer block as previously described.[60] Cycloolefin (COP) capillaries (28 ± 2 μm i.d.) were sulfonated by chlorosulfonic acid (www.acros.com) to a capacity of ~3 pequiv/mm2 and coated with anion-exchange (AEX) AS18 latex particles (65 nm diameter, courtesy Thermo Fisher Scientific) to serve as separation columns.[61] Both laboratory-built[57,58] and commercial detectors (TraceDec, http://www.istech.at) were used for on-column admittance measurements.

Analyte anions were prepared in the form of reagent-grade sodium or potassium salts and cations as either chloride or bromide salts (reagent-grade chemicals, used as received). Ultrapure water (Milli-Q; www.millipore.com) was used throughout. All eluent solutions were prepared in DI water; sample solutions were prepared in eluent or DI water.

3.2.1 Description of Conductivity Cells.

3.2.1.1 Design A

Figure 3-1a is like that of Huang et al.[63] except that the holes are drilled not in the separation capillary but in a separate larger i.d. (75 μm) exit capillary. Two diametrically opposed holes are drilled through the detection capillary walls only 200 μm from the terminus to minimize dispersion in the much larger tube. Tungsten wires of 100 μm diameter were used as electrodes. The fabrication procedure is illustrated in Figure B-S1 in the Supporting Information. For testing of the conductance cell, an unmodified silica capillary (25 μm i.d., 73 cm in length) functioned as the “separation capillary” and was butt-joined to the PEEK detection capillary (Figure 3-1a and Figure B-S1 in the Supporting Information). The cell was tested in the flow injection mode.

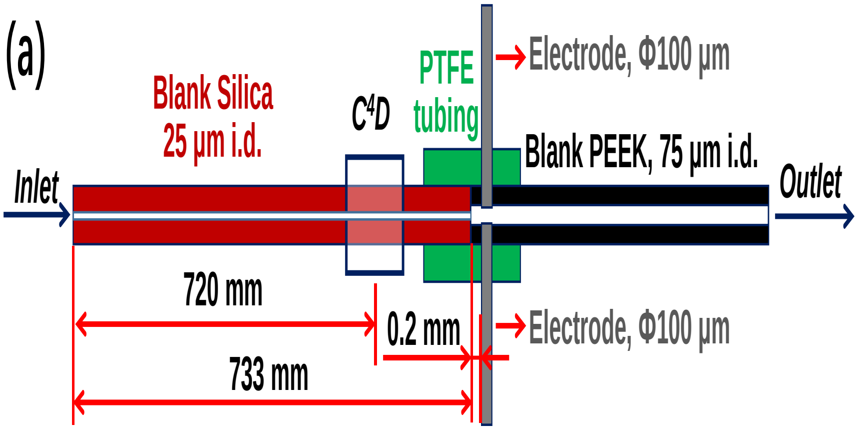

Figure 3-1 (a) Standard opposed electrodes. See text for details.

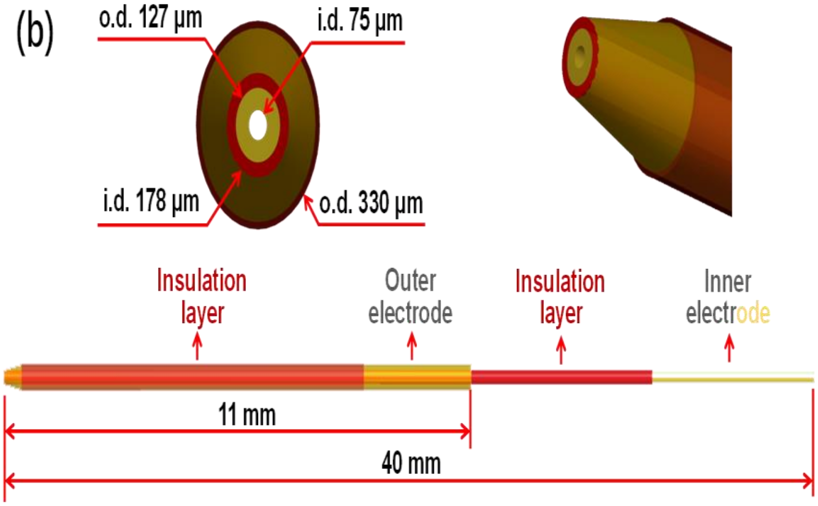

Figure 3-1 (b) Annular ring electrodes. See text for details.

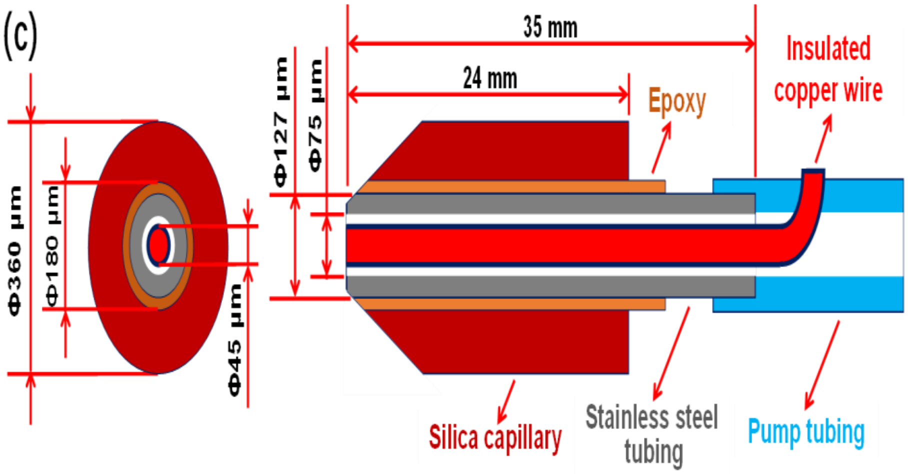

Figure 3-1 (c) Ring-disk electrodes. See text for details.

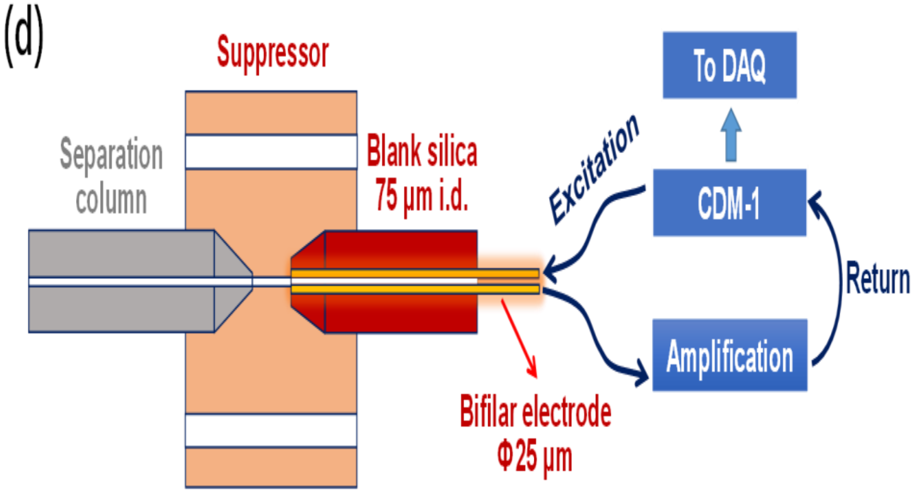

Figure 3-1 (d) Bifilar electrodes. See text for details.

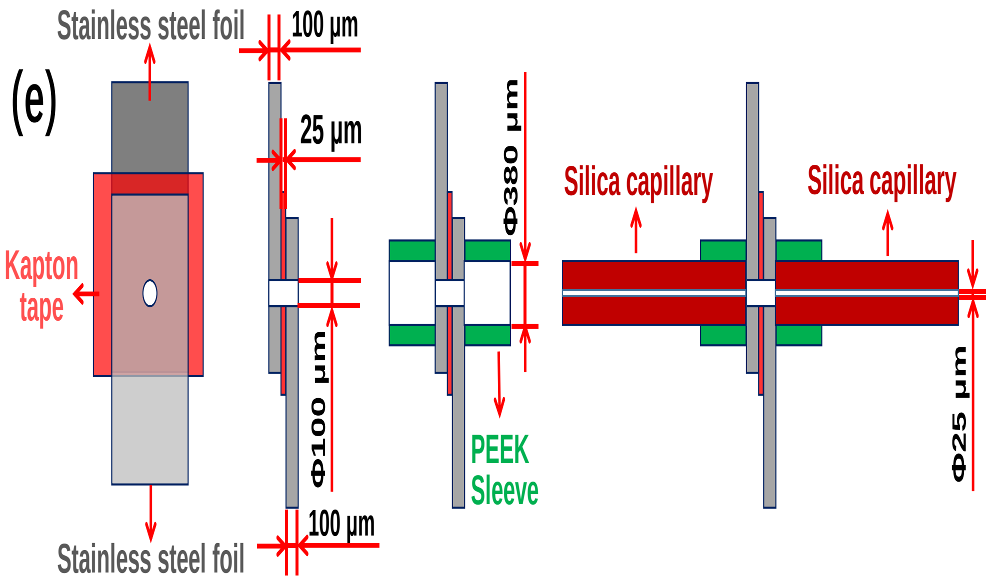

Figure 3-1 (e) Planar foil electrodes. See text for details.

3.2.1.2 Design B

Figure 3-1b utilized a pair of SS capillaries as electrodes in an annular configuration (inner tube, 75 µm i.d., 127 µm o.d., ~4 cm in length; outer tube, 178 µm i.d., 330 µm o.d., ~1 cm in length). The first ~15 mm of the inner tube was coated with a thin layer of epoxy adhesive as insulation on the exterior before insertion into the outer tube until the tips were coplanar. A larger amount of epoxy was applied where the inner tube exited the outer tube to hold the assembly in place. After curing, the first ~7 mm of the outer capillary was coated with epoxy on its exterior to serve as insulation. After curing, the tip of the outer electrode was honed by a micro grinding tip under a microscope to a pencil shape (Figure 3-1b) and the exposed surface coated with epoxy again for insulation. After curing, the very end of the tip was polished with emery paper to remove any insulating adhesive from the tip surface, effectively making the tip surface a planar annular ring electrode. Electrical connections were made with lead wires and silver epoxy with the exposed ~3 mm of the outer tube and the protruding part of the inner tube. Much like a honed capillary previously used as a capillary suppressor exit tube on which an admittance detector was placed, this honed annular assembly served as the exit tube with its tip providing electrodes for contact conductometry. Photos of the detection arrangement along with a capillary suppressor are shown in Figure B-S2 in the Supporting Information. The performance was tested under chromatographic conditions.

3.2.1.3 Design C

Figure 3-1c emulated a ring-disk electrode.[66] A SS capillary (75 µm i.d., 127 µm o.d., 35 mm in length) was coated on the exterior with epoxy adhesive and put inside a silica capillary (180 µm i.d., 360 µm o.d., 24 mm length) acting as a sleeve. After curing, the tip of the silica capillary (and the SS tube tip inside it) was honed to a conical shape. An enameled copper wire (45 µm in diameter) was used as the central electrode. A finegauge hypodermic needle was inserted through the wall of a small segment of a 0.125 mm i.d. vinyl tubing (peristaltic pump tubing), and the copper wire was inserted through the needle to go through the wall of the vinyl tube. The needle was then removed. The protruding length of the wire was then inserted through the SS tube and the vinyl tubing push-fit to the free terminus of the latter. Excess copper wire protruding from the honed tip was cut off with a scalpel blade. Photos of the cell and its assembly with a capillary suppressor are shown in Figure B S3 in the Supporting Information.

3.2.1.4 Design D

Figure 3-1d is an adaptation of the previously used design using bifilar wire electrodes (Figure B-S4 in the Supporting Information). This cell was relatively easy to make: one end of the insulated bifilar wire (copper, ~20 μm diameter each strand, separated by ~10 μm of insulation) was inserted through the flat end of a silica capillary (75 μm i.d., 360 μm o.d., ~2 cm in length), the exit end being prehoned. Excess wire was cut off at the tip with a sharp scalpel blade. At the entrance end, the bifilar wire was split into two individual strands (Figure B-S5 in the Supporting Information), to which lead wires were soldered. The probe was assembled with a capillary suppressor and tested in the SOTIC mode (Figure B-S6 in the Supporting Information).

3.2.1.5 Design E

Figure 3-1e represents an altogether different concept where the liquid of interest flows through a 100 μm hole in two parallel planar electrodes separated by ~175 μm (nominal). A 25 μm thick polyimide tape with 75 μm thick silicone adhesive on each side was sandwiched by two 100 μm thick SS foil electrodes that were vertically offset to facilitate electrical connections. A 100 μm hole (smallest available mechanical drill) was drilled through the SS foils and the tape in a perpendicular direction. Silica capillary segments (100 μm i.d., 360 μm o.d.) were each inserted inside two 1 cm lengths of snugfit PEEK sleeves (380 μm i.d.). With a 75 μm tungsten wire inserted in the hole of the foil sandwich assembly and using that as a guide, one sleeved capillary was aligned on the hole (wire inserts into the capillary) and the sleeve was then epoxied to the SS foil. After the epoxy was cured, the second sleeved capillary was similarly lined up on the other side and affixed in place. After full curing, the wire and the capillaries were removed from the sleeves, leaving the latter attached to the foil electrodes. Flat-cut, end-polished silica capillaries (20 μm i.d. for the inlet, where this couples to the suppressor, and 25 μm i.d. for the outlet capillary, which goes to waste) were then inserted into the sleeves and pushed simultaneously until they met at the foil surface. Figure B-S7 in the Supporting Information shows a photo of the foil electrode cell, by itself and in an assembly with a capillary suppressor and a TraceDec admittance probe following it. It is vital that capillary ends be as flat as possible to minimize dispersion. A comparison of the unpolished and polished tips of the silica capillary and the tool used to polish the capillary are shown in Figure B-S8 in the Supporting Information.

3.2.2 System Setup and Electronics.

A pneumatic pumping and injection system (Figure B-S9 in the Supporting Information) like that in a previously described report[58] was used. The contact conductometric cells as well as the admittance detector probe were variously positioned before and after the suppressor. Although Figure B-S9 depicts a system where the admittance detection probe and the contact conductometric probes were positioned respectively before and after the suppressor, multiple configurations were tested.

The cell constants of all the present contact conductance cells were relatively high and required preamplification before processing by most off the shelf conductivity detector electronics. Inasmuch as the purpose of the present work was to assess the functionality and utility of the different cell designs, we did not make any effort to perfect the electronics or minimize noise. We used a ca. 1981 conductivity detector (Dionex CDM- I, 5 V p-p, 3 kHz) and a two-stage operational amplifier (TL082; www.ti.com) between the detection electronics and the cell to amplify the current 20−1000× (Figure B-S10 in the Supporting Information). Connections, the cell, and the entire arrangement were not shielded. The analog output of the CDM-1 was digitized and acquired at 5 or 10 Hz by a DAQ card (EMANT300; www.emant.com). The commercial admittance detector used was a TraceDec instrument (www.istech.at).

3.3 Results and Discussion

3.3.1 Sensitivity and Linearity in Admittance Detection.

For admittance detection in a small-bore capillary, the response as a function of analyte concentration is acutely dependent on the background conductance of the solution and the operating frequency of the excitation signal. If the background conductance is sufficiently high, an excitation frequency can be found where the detector response will be linear with the background conductance, at least over a modest range. As these detectors have been almost exclusively used in applications where the background electrolyte concentration is minimally several millimolar (e.g., in capillary or microchip electrophoresis), issues with response nonlinearity have not been raised much in the literature. In our own experience with nonsuppressed OTIC (5 mM Na-benzoate eluent), reasonable linearity is observed at f = 150 kHz:[61] see Figure B-S11 in the Supporting Information. It is interesting to note in this figure that the linear correlation is often perceptibly worse for area-based quantitation than for height; the significance of this will become apparent later. However, linear response is not observed when the background has a very low specific conductance, as for example in SOTIC with a hydroxide eluent, when the detector background is essentially pure water or when simply the response to pure electrolyte solutions at low concentrations is measured. Figure B-

S12 in the Supporting Information shows sensitivity plots as a function of concentration for 50−400 μM KCl solutions at frequencies ranging from 100 Hz to 37.2 kHz: the response is not truly linear at any frequency even across this relatively short concentration span. Figure B-S13 in the Supporting Information shows a Bode plot for the frequency dependence of the signal, in terms of both height/areas, for five injected anions all at the same concentration in a SOTIC setup. Although they are all singly charged anions and the ionic mobilities are similar (and the concentrations are low enough for HF and HNO2 to be mostly ionized), there are subtle differences between the anions as to the frequency where the maximum signal is observed. The chromatographic peak broadens with increasing retention time; as such, the anions eluting later are mapped over a lower conductance terrain in comparison to fluoride or chloride. Accordingly, the frequency optimum shifts to lower f with more retained anions. With a commercial admittance detector, with the lower excitation frequency limit being 38 kHz, the signal disappears as the frequency increases (Figure 3-2). The calibration curve for five anions at this frequency is highly nonlinear in contrast to contact conductivity detection (Figure 3-3).

One aspect of this behavior at the probe frequency used in the experiment in Figure 3-3 is the apparent difference in height vs area-based quantitation. While the former is probed at the signal maximum, in the latter, the edges of a peak are poorly represented or do not appear at all. Second, this exponential response behavior makes the peaks appear more efficient than they really are; such signal transformation is sometimes deliberately done, and the mathematical basis of this is wellknown. [70,71] Third, the apparent efficiency is extremely dependent on the admittance measurement frequency; as shown in Figure B-S14 in the Supporting Information, which plots peak half-widths as a function of frequency in a gradient SOTIC system, the apparent half-width can dramatically decrease with increasing probe frequency. For example, for phosphate, the plate counts can vary by 40× from $f = 1$ to 40 kHz. Only when both f and σ are relatively high do admittance measurements more closely reflect the solution conductance. As such, it is impossible, for example, to judge dispersion induced by a suppressor. If the nonsuppressed signal ahead of the suppressor is measured with an admittance detector at an appropriately high f and measured after the suppressor with a suitably low f, the computed dispersion is negative: the peaks are narrower after the suppressor![60]

The virtues of “C4D”/admittance detection are unquestionable: not only is it highly flexible and simple but also it is difficult to beat the detection volume. If the latter is effectively governed by the distance between the electrodes, a spacing of as little as 100 μm has been demonstrated.[72] Nevertheless, highly nonlinear response behavior in the low σ−low capillary diameter domain and continuously variable response behavior with probe frequency (differently for peak height and peak area, Figures B-S15 and B-S16 in the Supporting Information) are not virtues. Most would agree that peaks appearing more efficient than they are in reality is also troublesome; this is compounded by firmware-imbedded filtration[73] by the leading commercial detector that also greatly distorts reality. It is therefore necessary to explore contact conductivity detectors at this scale. Even if the induced dispersion cannot yet match what is seemingly attained with admittance detectors, we cannot get there without exploration. This is the prime driver of the present work.

3.3.2 Performance of the Contact Conductometry Cells.

3.3.2.1 Design A.

This is the simplest of possible designs and mimics the very first effort of Huang et al.[63] However, the electrodes are on a separate and larger capillary. Even though

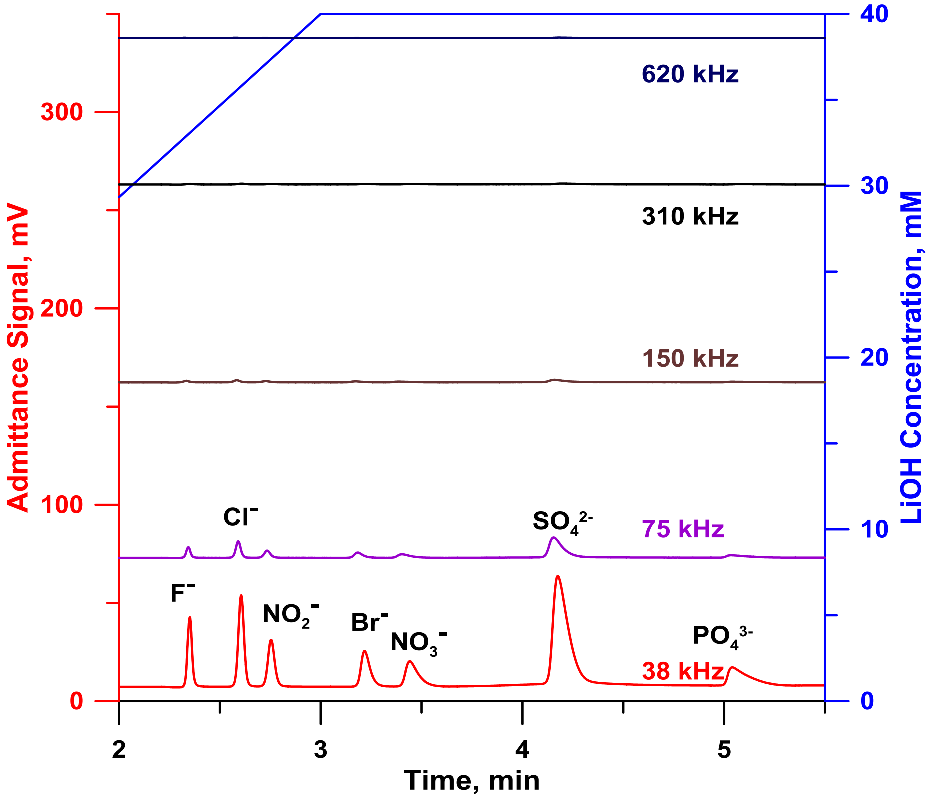

Figure 3-2 Effect of probe frequency on admittance signal in a gradient SOTIC setup. Sulfonated COP column (28 μm i.d., 370 μm o.d., 690 mm in length) coated with AS18 latex. Exit capillary: silica, 25 μm i.d., 370 μm o.d., 75 mm in length. TraceDec admittance detection: voltage, 0 dB; gain, 200%; frequency, 38−620 kHz; detection probe located 30 mm from the suppressor center. The linear gradient begins at 0 min with 8.0 mM LiOH and ends at 40.0 mM LiOH, at a flow rate of 175 nL/min. Suppressor active length 0.46 mm, current 5.0 μA. Injection 7.0 nL, each analyte 100 μM except for phosphate (200 μM).

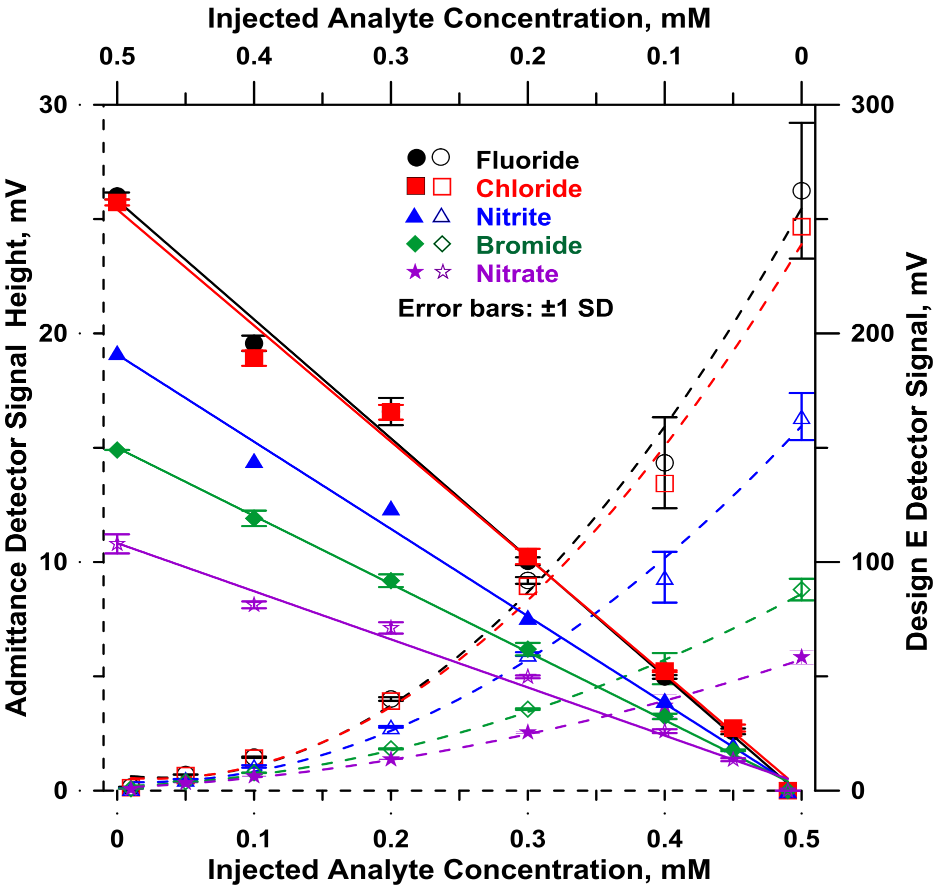

Figure 3-3 Calibration plots for five anions under isocratic elution SOTIC conditions with admittance detection at 38 kHz by a commercial detector (left ordinate, bottom abscissa, hollow symbols, quadratic best fits as dashed lines) and contact conductance detection (design E, top abscissa (note reversed direction for clarity), right ordinate, filled symbols, linear best fits as solid lines). COP column: 28 μm i.d., 370 μm o.d., 782 mm in length. Effective length: 782 + 40 mm (admittance). Suppressor length: 0.80 mm. Suppressor current: 10 μA, Detection frequency: 38 kHz. Eluent: 5 mM KOH. Injection volume: 2.0 nL. Running pressure: 40 psi.

electrode placement (0.2 mm) cannot be any closer to the edge, because of a 9× greater cross-sectional area, there will be unwanted dispersion. Still, Figure 3-4 shows the results of an experiment that illustrates the difficulty of evaluating this, especially with the effects of imbedded filtration in the admittance detector. At first sight, cell A clearly produces wider peaks that are tailing in comparison to the admittance detector. However, it is apparent that the admittance detector behaves very differently when (a) a more conductive solute is injected into a less conductive carrier and (b) vice versa. Flow-injection peaks intrinsically tail; this behavior is not observed in either admittance responses: In Case a, the peak fronts while Case b indicates an almost symmetric peak (see As,0.1, asymmetry values at 10% height). For the injected volume, the base width for a square plug would be computed to be 5.5 s without any dispersion and the observed admittance response width is even smaller- a physical impossibility. While the 10−90% signal rise times and the 90−10% fall times are the same for conductivity cell A, for cases a and b, they are very different for the admittance detector. Note that the staircase response pattern of the conductance detector is a consequence of inadequate sampling rate; the DAQ card used permitted a maximum of 10 Hz.

3.3.2.2 Design B.

Cell designs B−D permit direct insertion into the suppressor and may be preferable in the current implementation of SOTIC. However, this distinction will disappear when on-column suppressors become possible. The shortcoming of the annular tubular design has the fundamental dimensional limitations of available metallic tubing; the minimum i.d. is twice that of the separation columns. Even accounting for less than ideal behavior of the admittance detector as outlined in the previous section, Figure B-S17 in the Supporting Information suggests that dispersion is too large.

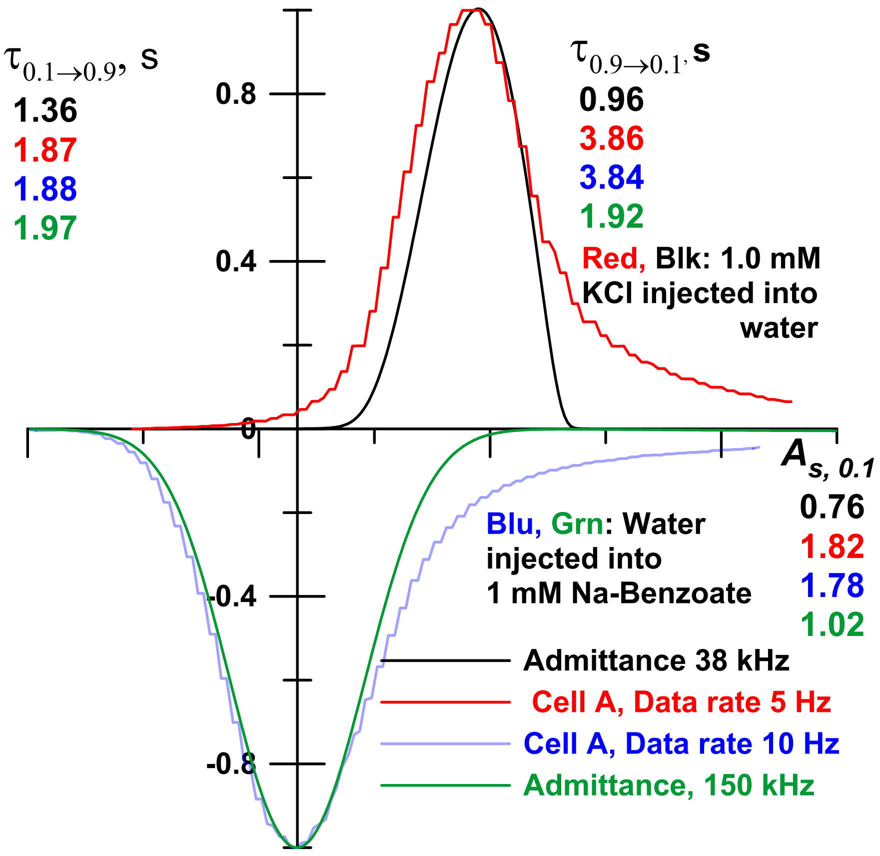

Figure 3-4 Flow injection response comparison: serially placed TraceDec admittance detector (L = 72 cm) and cell A (L = 73.3 cm), 25 μm i.d. capillary, flow 0.46 cm/s, injection 2.7 nL. X-axis span: 14 s, ticks 2 s apart. Peaks were normalized in amplitude and apex locations shifted in time for time-aligned superposition.

3.3.2.3 Design C.

Design C is a ring-disk design, with the central electrode being copper and the ring electrode being the edge of the surrounding SS tubing. It was tested in the SOTIC format. Figure 3-5 shows the chromatograms of a six-anion mixture for the admittance detector (unsuppressed, 450 μM each) and cell C (suppressed, 100 μM each). The separation of adjacent analyte pairs appears to be worse after suppression as detected by cell C. Suppressed chromatograms for different analyte concentrations are shown in Figure B-S18 in the Supporting Information, and illustrative linear calibration plots for two analytes appear in Figure B-S19 in the Supporting Information. The exact dispersion due to the cell itself is difficult to assess, as the dispersion due to the suppressor is unknown. Our choice of a copper wire as the disk electrode was one of convenience, as one of suitable diameter was available in the laboratory. It was anticipated that such an electrode will not last long because of corrosion. This proved to be the case: over a period of several days, the electrode tip dissolved (Figure B-S20 in the Supporting Information). Insulated microwires of corrosion-resistant metals, e.g., nickel, are readily available, and even the copper wire tip can readily be plated with gold. A factor that contributed to the electrode erosion is that the power supplies of the suppressor and the conductivity detector shared a common ground; these are easily isolated from each other.

3.3.2.4 Design D.

The previous bifilar wire design,[67] used very successfully in 75 μm i.d. capillaries, utilized the cylindrical surfaces of the bifilar wires as the electrodes. For use in smaller capillaries, we envisioned the disk-like wire termini faces functioning as the electrodes. A copper bifilar wire of small enough dimensions was already available in the laboratory and was thus used for expediency. As with cell C, the admittance detector and cell D

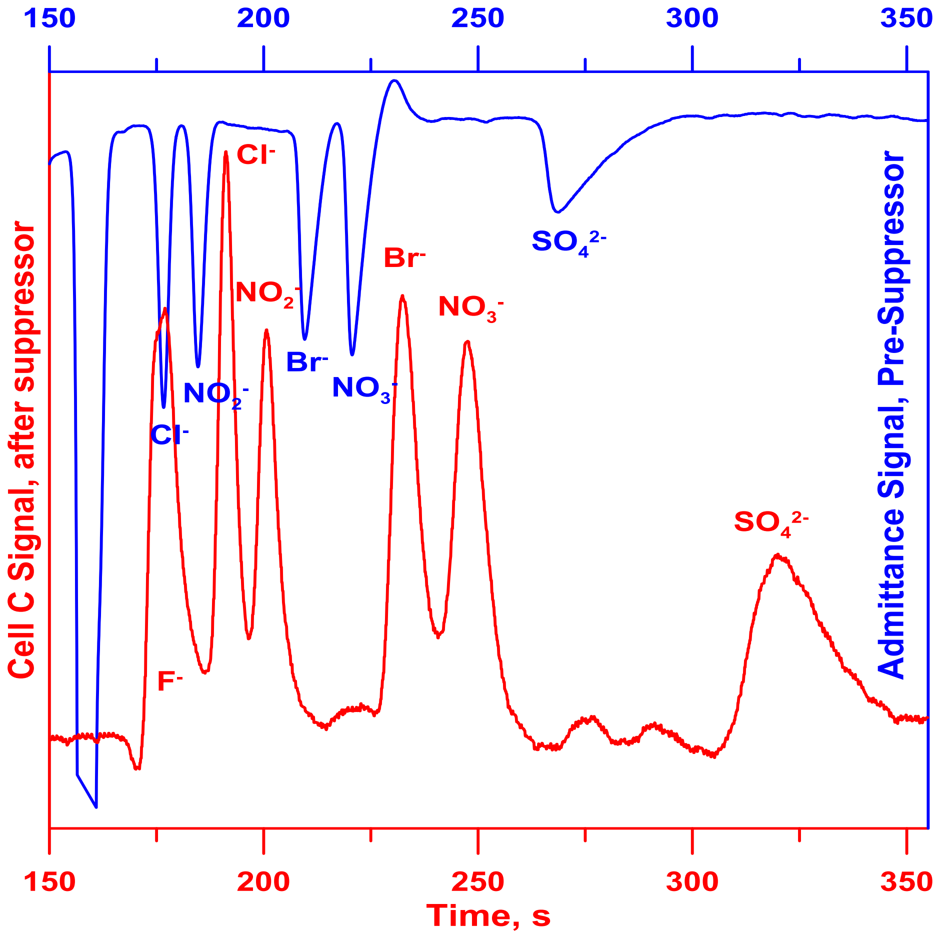

Figure 3-5 Cell C (100 μM each analyte, red trace) vs admittance detector (450 μM each analyte, blue trace); see the Supporting Information for details. Two unidentified impurity peaks (one is likely carbonate) are present between nitrate and sulfate. Injection 4.2 nL, 8 mM NaOH eluent. Cell C preamplification 100×. AS18 coated sulfonated COP column: 28 μm i.d., 370 μm o.d., 906 mm in length. TraceDec admittance detection: voltage, −24 dB; gain, 200%; frequency, 150 kHz; effective length: 850 mm. CDM-1 range: 30 μS. Suppressor active length 0.85 mm, voltage 19.1 V. Running pressure: 40 psi.

respectively preceded and followed the suppressor. Figure B-S21 in the Supporting Information shows the results. The resolution between analyte pairs is markedly better than for cell C. Some low-frequency spikes in the signal output were observed throughout, the cause(s) for this was not investigated at this time. The overall repeatability was excellent, however (Figure B-S22 in the Supporting Information). This attests to the reproducibility of the entire system, including the detector.

3.3.2.5 Design E.

This approach uses closely spaced planar electrodes with a circular aperture through which liquid flows, essentially equivalent to two tubular electrodes facing each other,[74] except that the tubes here are ultrashort. In this experiment, both detectors were located after the suppressor, with the admittance detector following cell E. Figure 3-6 shows the results from cell E and the admittance detector as well as the nonlinear response of the latter linearized by postprocessing of the data. To accomplish the latter, we plotted peak maxima response for various analytes at various concentrations and created a best-fit curve (Figure B-S23 in the Supporting Information) that allowed the transformation of the admittance detector output to what it would have looked like were the response linear. The raw conductivity and admittance responses, respectively in gray and blue, will suggest that admittance response has a greater peak efficiency. This is physically impossible, as the admittance detector follows cell E. This is an artifact of the exponential response behavior: when the exponential response behavior is linearized (dashed green trace), the peak width is seen in fact to be slightly greater than that of the gray trace, as would be expected from additional tubing between the two detection locations.

3.3.3 Comparison among Contact Conductivity Cell Designs.

The present implementation of cells A and B leads to too much dispersion

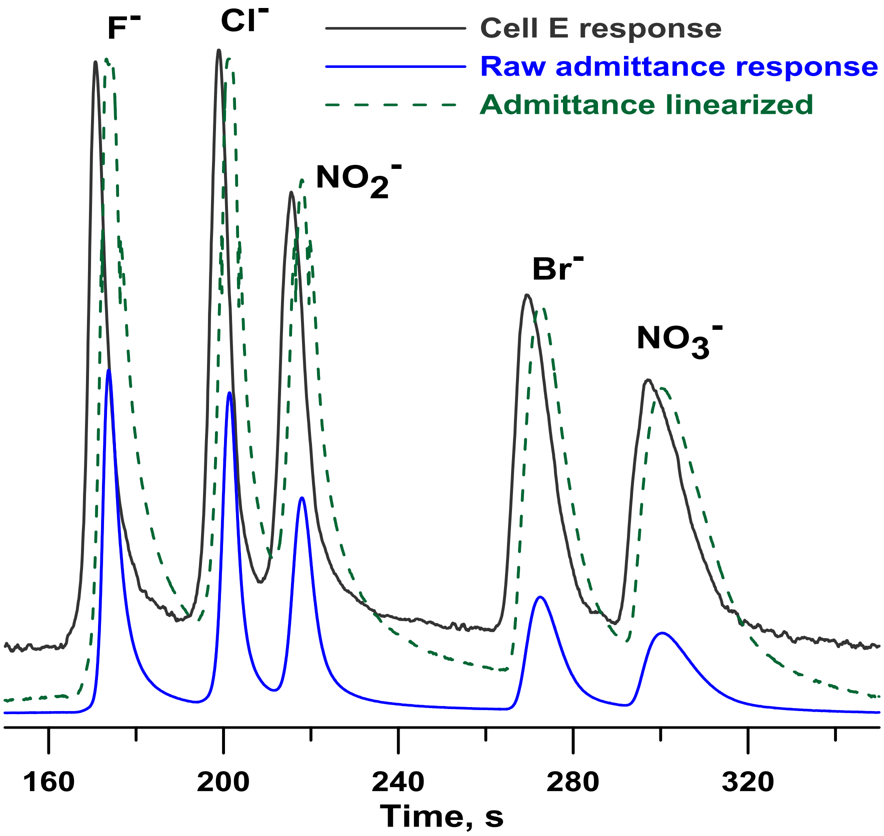

Figure 3-6 Black trace showing the conductivity response of cell E following a 782 mm column and a 0.8 mm active length suppressor (drive current 10 μA), preamplification 565×. Cell E was connected to the suppressor by a 25 mm length and 20 μm i.d. capillary. Exit capillary from cell E: 50 mm length, 25 μm i.d., on which the TraceDec probe center (38 kHz, blue trace) is placed 15 mm after cell E. Eluent: ~5 mM KOH. Injection 2.0 nL, each analyte 0.50 mM. Running pressure: 40 psi. The green dashed line is the linearized TraceDec response; see text for details.

relative to the other designs. It is unlikely that design B can further miniaturized to be practical, given the availability limitations of the minimum diameter of conductive tubing. Design A fundamentally follows the same geometry originally advocated by Zare's group[63,65] and is by far the most common geometry for placement of electrodes for conductometry in microfluidic platforms. It obviously has merits if one can devise an arrangement where microwire electrodes are not prone to movement due to capillary exit flow[65] or a major change in bore diameter, as in the present case, can be prevented. As designs C−E were all tested chromatographically under approximately comparable conditions, chromatographic efficiencies can be compared. The differences are likely to be more marked for a smaller half-width peak than for a larger one, and so it is best to choose a fast-eluting peak. As fluoride is not always completely resolved from the water dip, we chose to look at chloride. All three designs produced efficiencies of 12000 ± 200 plates/m; they could not be distinguished on the basis of experimental error. Our experience indicates that this efficiency is being limited by the dispersion in the suppressor. We hope to report soon on an on-column integrated suppressor with much lower dispersion; this will then give us an added impetus to differentiate between, and hopefully improve on, the described contact conductometric cell designs.

3.3.4 Limits of Detection.

The present electronics was far from optimized to really explore ultimately attainable limits of detection (ambient temperature, no enclosure, unshielded cell leads connected with alligator clips, etc.; see Figure B-S6 in the Supporting Information). However, in comparison to an admittance detector (where the transimpedance amplifier gain for the present capillary dimensions and specific conductance is typically ≥109 V/A), much greater currents result in the direct contact detection mode and in principle better LODs should be attainable. Figure 3-7 with cell E or Figure 3-5 with cell C suggests that,

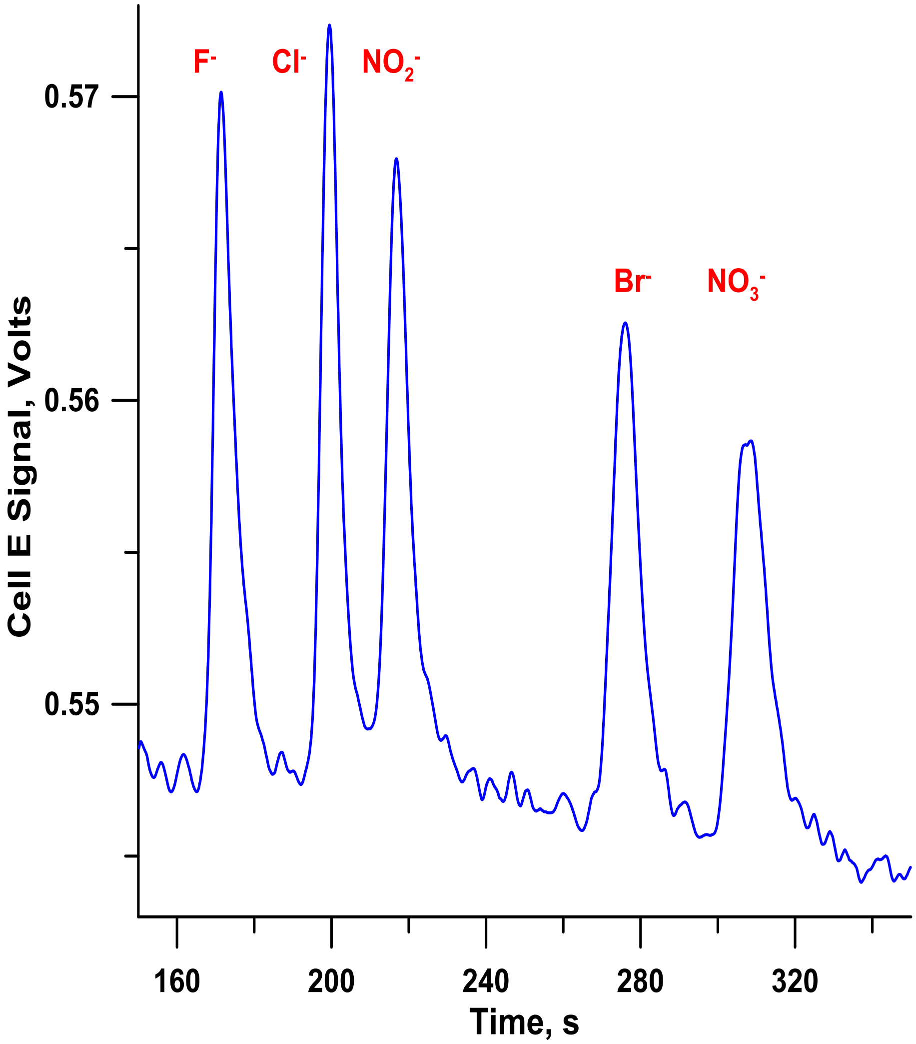

Figure 3-7 Each analyte 50 µM (100 fmol). Conditions as in Figure 3.6. A Gaussian kernel moving average filter (2 s) was applied to the data.

even in the present form, the LODs are in the single digit micromolar in concentration or double-digit femtomoles in amount (Table 3-1).

Table 3-1 Projected Detection Limits[a]

	F^-	**Cl^-**	**$NO2^-$**	**Br^-**	**$NO3^-$**
S/N = 3 LOD; μM (fmol)	7.3 (15)	6.7 (13)	8.3 (17)	10 (20)	13 (26)

[a]Based on data from Figure 3.7 (contact conductometric cell E; suppressed detection).

3.4 Conclusion

We have described the design, construction, and performance of five end-column solution contact conductivity cells for open tubular ion chromatography. While an on-column admittance detector is much more convenient and is commercially available, this approach has a highly nonlinear response with analyte concentration, essentially responding in an exponential manner at very low conductivities. This may lead to a pleasant artifact, with the peaks appearing narrower than they are, but this is a mirage. There have been previous publications in which the same solution volume has been probed by both admittance and optical (absorbance and fluorescence) techniques.[75] Unfortunately, the efficiencies in admittance vs optical detection modes was not simultaneously studied. The nonlinear response of the admittance detector also greatly complicates quantitation. In contrast, all of the contact conductance measurements were linear with concentration. Initial results suggest that attainable LODs are competitive with those from benchtop ICs.

Chapter 4

NANOVOLUME GAS-FREE HYDROXIDE ELUENT GENERATOR FOR OPEN TUBULAR ION CHROMATOGRAPHY

4.1 Introduction

Suppressed Ion chromatography (IC) is the benchmark approach to anion analysis. Alkali hydroxides are the preferred eluents for anion exchange (AEX) chromatography because they generate pure water as the suppressed background. Manually prepared hydroxide eluents contain impurities like Cl^-, CO_3^{2-} etc. Further, additional CO_2 absorption during use, leading to continually increasing carbonate concentration in the eluent, is unavoidable. This leads not only to a background that increases over time, gradient performance and retention time reproducibility are severely affected. Early on, the feasibility of an electrodialytic high purity hydroxide eluent generator (EG) and current-programming such a device to generate eluent gradients were demonstrated.[76,77] Such electrodialytic eluent generators have been in commercial use for some time;[78] for a review, see ref. 79. Small et al.[80] integrated eluent generation and suppression in a novel packed resin bed-based system called “Ion Reflux”. A closely related configuration, also based on packed ion exchange resin beds, was then described; here eluent generation and suppression were physically isolated: the hydroxide normally generated as the suppressor waste was recirculated and sufficient suppression capacity maintained by periodically reversing the roles of the generator and the suppressor.[81] In both above systems, metal electrodes were in direct contact with the resin bed and electrolytic gases travel through the system, albeit their influence on the detection process is minimized by having sufficient backpressure on the detection cell. In a more recent and substantially more elaborate embodiment of these principles, the electrodes were isolated by membranes, avoiding the gas bubble travel through the chromatographic system. The ability of the system to operate reproducibly over long periods using only a limited amount of liquid water as the initial input was demonstrated using synthetic samples.[82] An ultimate merit of such completely (complete except for electrolytic conversion water to hydrogen and oxygen) recycled systems is in environments where external liquid input or waste generation will be undesirable. An alternative to such recycled systems is to operate at a scale where neither eluent consumption nor waste generation is significant. We embarked on open tubular ion chromatography (OTIC) 2 decades ago;[83] a number of other efforts already existed by then.[84-87] Although the superiority of eluent suppression (and on-line generation) were already well-established, extant technologies and associated large dispersion did not permit suppressed OTIC. Suppressed Capillary IC remained limited to the packed column format for decades.[88-90]

Compared to macrocolumns, EGs for smaller columns obviously demand smaller generator internal volume. Even to go from the traditional 4-mm to the 2-mm format, EGs have more recently been custom designed.[91] For 180 μm ϕ packed capillaries, a membrane-based EG with a 3.8 μL internal volume was developed.[89] An even smaller volume cation exchange resin bead-based generator was later described.[92] None of the above are gas-free and a separate degassing tube (whose connective and internal volumes are not included in the above) must be used.[89-92] Gas-free generators that use a cation exchange membrane (CEM) and an anion exchange membrane (AEM) were conceived early on.[76] However, it was already recognized that as measured by suppressed conductance, the eluent generated from such CEM/AEM generators were not as pure as those from single CEM generators, whether because of reductive electrochemical degradation of the AEMs or the permissible passage of adventitious anionic impurities from the AEM feed side. Although high-pressure capable EGs based on cation and anion exchange resin beads with small internal volumes (nominal volume 3.2 μL) have been described, not only for hydroxide eluent generation,[93] but also acids, salts, etc.,[94] purity problems with electrogenerated hydroxide eluents remained in any EG utilizing an AEM or its bead equivalent to render it gas-free. Indeed, until very recently, the only gas-free truly pure hydroxide EG without purity issues relied on CEMs only: a transport barrier resulted in Donnan breakdown.[95] This design, however, requires higher voltages with consequent Joule losses. The patent literature describes porous noble metal electrodes, especially a Palladium cathode directly deposited on a membrane surface to minimize or eliminate the gas evolution problem.[96] The present senior investigator made extensive investigation of Pd cathodes, however, and found that the electrode resistivity dramatically increases as it absorbs H_2. The hydrogen is not effectively released at normal operating temperature. Yang's group has recently provided an elegant solution to this old problem. They used a CEM and an appropriately oriented bipolar membrane (BPM), each backed externally by a stack of CEMs to provide pressure tolerance (and also prevent transmembrane water loss) to make a gas-free hydroxide EG.[97]

As stated, our present interest lies in OTIC using ~25 μm or smaller i.d. functionalized columns.[98] The typical flow rates are < 200 nL/min. The Lu et al. generator[97] is designed for mL/min flow rates. It has an internal volume of ~500 μL and the design cannot be directly scaled down. Nevertheless, the concept is particularly attractive for OTIC as the performance of a degasser in a conventional EG depends in part on the high backpressure the column provides. Such backpressure is not present in OTIC and providing additional restriction to promote degassing will simply negate one of its best virtues, low pressure pumping needs. On the other hand, because OTIC operates against low backpressure, stacks of membranes are not needed in an EG to prevent transmembrane liquid loss. Electrogenerated eluents/eluent gradients have been used in OTIC but only from a conventional benchtop instrument designed for 0.4 mm columns and splitting the output flow: a column/restriction tube is still present in the main flow stream to provide backpressure.[99,100]

We provide here a nanovolume gas-free hydroxide EG that can provide reproducible gradients and demonstrate its performance in a standalone pneumatically pumped chromatographic system in conjunction with PEEK OTIC columns that are also described for the first time. Like the Lu et al. EG, it is also CEM-BPM-based. A BPM is a single ion exchange membrane where one side is composed of a CEM and the other side an AEM. If the CEM side is held positive and the AEM side negative, the BPM is said to be forward-biased. Cations present exterior to the CEM and anions present exterior to the AEM can proceed through the respective membranes to the internal interface. With the opposite polarity of the applied potential, ion transport to the interface is not possible and the applied voltage essentially appears across the very thin interface region. In this reverse-biased condition, the internal membrane interface therefore experiences a very high electrical field strength. The presence of this high field is presumed to enhance dissociation of the interfacial water into H^+ and OH^- due to the Wien effect.[101] The H^+ and OH^- thus generated can migrate out of the interface through the CEM and AEM towards the negative and positive electrodes, respectively. In this paper, we also directly and quantitatively demonstrate the enhanced dissociation of pure water in a high electrical field of exactly known field strength for the first time.

4.2 Experimental Section

4.2.1 Water Dissociation at High Fields.

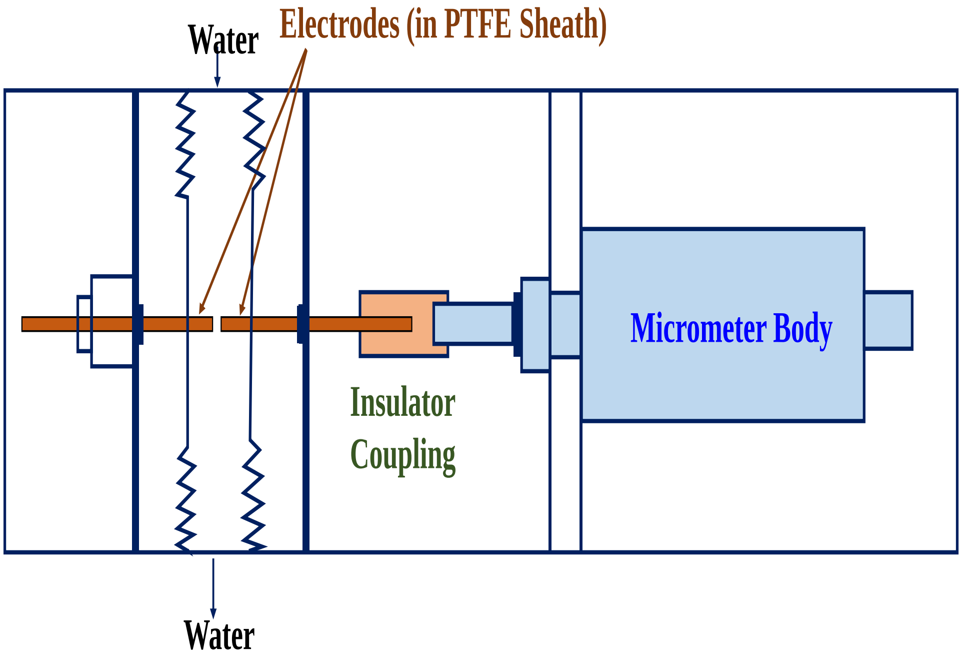

Figure 4-1 Arrangement for high-field specific conductance measurement. Electrode separation ranged from 0.02-0.50 mm with 3-12 V applied, resulting in field strengths of 6 x 103 – 6 x 105 V/m.

The arrangement utilizes two stainless steel rod electrodes ($^1/_{16}$" dia.) face polished to a mirror finish and provided with tightly fitting PTFE tubular sleeves such that only the face of the electrode was exposed to the water. The electrodes were placed in a flow conduit machined from Plexiglas. One electrode was fixed in place; the other, movable electrode, was placed directly facing the stationary electrode with its other end connected (via an O-ring seal to prevent liquid leakage) to a micrometer head (Mitutoyo, 0-25 mm, 0.001 mm accuracy, Figure 4-1). The position of the micrometer at which the two electrodes touched (dry cell, shorting as indicated by a multimeter) was taken to be zero spacing. The interelectrode spacing was varied from 0.02-0.50 mm, by backing off the movable electrode. Some experiments were conducted where the electrode faces were pulse-plated with rhodium using a nickel interlayer [102] The water flow was perpendicular to the common cylindrical axis of the two electrodes through a 3.2 mm ϕ bore channel (see photograph in Figure C-S1 in the Supporting Information (SI)). To ensure that the water was as pure as possible and minimize effects from gas evolution, electrode corrosion or heat generation, water was directly supplied from the water purification system and flowed through a short length (~30 cm) PEEK tubing through the device at the maximum feasible flow rate (without further adding pumps, etc. that can add to contamination) of 7.0 mL/min. For sub-electrolytic DC voltages, the current flow was undetectable (in the noise limit, unrelated to the precise applied voltage). Experiments were therefore conducted only above the electrolytic threshold (3-12 V). Voltage and current were measured by a Keithley model 2400 sourcemeter. Conductance was also measured by a bipolar pulse technique, as used in a Dionex CD25 detector (28 V p-p square wave, 8 kHz).

4.2.2 Nanovolume EG.

The device is shown schematically in Figure 4-2 (see also Fig. C-S2 in the SI). The EG is fabricated using a commercially available miniature polyetherimide (Ultem®) cross (C360-204, www.labsmith.com). As shown here, the device in Fig. 4-2 uses two further tees (acrylate, C360-203A) for liquid circulation behind the EG membranes. The internal center of the cross occupies a 0.75 x 0.75 mm region with 0.25 mm ϕ connecting passages. The horizontal passages were opened to 0.6 mm ϕ and the conical ferrule seat region was milled to have a flat seat with a 1.65 mm dia. bore, enough to accommodate a 1.6 mm o.d. tube (see Figure C-S3 in the SI). The vertical passage in the central cross is also bored out just sufficiently for 0.36 mm o.d. PEEK tubes to directly go to the central cavity and additional volume is avoided. Membranes used in the EG were punched out as 1.5 mm discs from sheets (CEM: FKM-PK, 0.13 mm thick; BPM: FBM-PK, 0.16 mm thick, both PEEK-reinforced, www.fumatech.com). The membrane discs are retained at the outer edges of the central EG chamber (ca. 0.75 mm long x 0.6 mm ϕ, ~210 nL in volume) by a 1.5-2 mm long PEEK spacer (cut from a 0.76 mm i.d. 1.6 m o.d. tube (green PEEK tube)) while PEEK nuts (Labsmith C360-100, ferrule end cut off to provide a flat end) press the membranes in place via the spacers on each side of the cross. All of the horizontally shown nuts in Figure 4-2 (C-S2) have been similarly treated, also the bores have been opened to 0.75 mm to permit passage of the metal tubes. Terminal ends of both the PEEK spacers and these nuts are polished flat for a good fit and exerting even pressure on the membrane disc edges. Short lengths of the same green PEEK tube provide low pressure connections between the cross and the tees. The heads of the relevant nuts are bored out a short distance to 1.5 mm to push fit the PEEK tubing into these nut heads. A little epoxy adhesive secures the tee-cross transit tubes to the nut

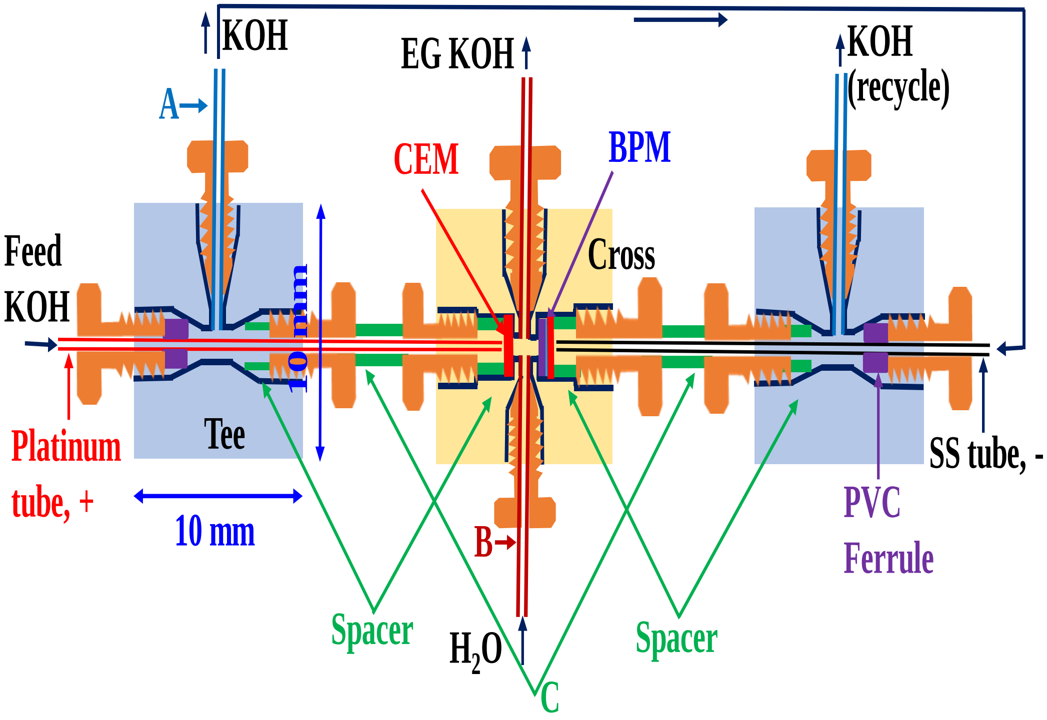

Figure 4-2 Nanovolume EG. A, B and C are PEEK tubing, respectively 100/360, 25/360, and 760/1600 µm i.d./o.d.; Anode/cathode tubes are Platinum/Stainless steel 38 x 0.70 x 0.32 mm and 44 x 0.57 x 0.37 mm L x o.d. x i.d. respectively. Ports are 2-56 threaded.

heads. The AEM side of the BPM faces the central cavity for appropriate polarity. The device can also be fabricated just with the cross, without the additional tees, with vertical holes drilled to access the region behind each membrane (see Figure C-S4). Except as explicitly stated for static operation, the outer sides of the CEM and the CEM side of the BPM are serially bathed by the same KOH feed solution (flow rate ~ 2 µL/min). The KOH feed solution (200 mM) enters through the blunt-ended Pt Needle tube (22 ga., www.hamiltoncompany.com), which is sealed in place in the left tee using a deformable PVC tube segment that acts as a ferrule. The channels in the tees are bored out to 1 mm to facilitate liquid passage. The feed KOH flows through the Pt tube (that ends just short of the CEM), bathes the CEM and flows around the needle to the vertical exit of the tee. Then tube A connects the KOH flow to the stainless-steel tube and the KOH bathes the back of the BPM and flows around the SS tube to the tee exit. Either a Keithley model 2450 sourcemeter was used as the constant current source or a PSoC 5LP programmable system on a chip was used, both as a current source (see Figure C-S5) and for data collection.

4.2.3 Preinstallation Cleanup of BPM.

The BPM is supplied with the CEM side in Na^+-form and the AEM side in Cl^--form. Simple short-term immersion in KOH was not particularly effective in removing the chloride. If the membrane is installed without removing the chloride, the generated eluent contains chloride and the amount appearing in the eluent becomes particularly noticeable when subjected to a current gradient. In principle it is possible to run it for a long time to remove the chloride in the membrane in an assembled EG, but this can be a slow process. Only a small fraction of the membrane (0.6 mm out of 1.5 mm, ca. 16%) is actually exposed to the central cavity, the rest leaches from the edge only slowly. A two-compartmented chamber, with electrode and flow provision on both sides, was constructed with a 6 mm dia. BPM separating them. Arrangements were made to flow 0.2 M KOH on both sides while a Pt wire electrode (+) is disposed on the AEM side and a SS electrode (-) on the CEM side. The membrane was subjected to 5 mA for 7-8 h before disassembly. Smaller discs were then punched out from the cleaned area of this BPM for use in the EG.

4.2.4 Measurement of Electrogenerated KOH Concentration.

This was carried out conductometrically. A relatively high cell constant (464 cm^{-1}, as calibrated with 10 mM KCl) small-volume flow-through cell was made by inserting two 75 μm Pt wires close and parallel to each other radially through a 190 μm i.d. PVC tube,[28] 360 μm od tubes are readily push-fit into this tube. We used KOH specific conductance data from Thermo Fisher Scientific (courtesy Dr. Yan Liu) for interpreting our specific conductance data to concentrations (See Table C-S1 and Figure C-S6 in the SI).

4.2.5 Reagents.

Analytical grade reagents were used as such without further purification. All water used was from a high purity water system (resistivity ≥ 18 MΩ.cm, www.ariesfilterworks.com/). Test analytes were solutions of sodium or potassium salts.

4.2.6 Open Tubular Columns.

Anion exchange OT columns were prepared from PEEK tubes (https://www.idex-hs.com/) 25 μm i.d., 360 μm o.d. The tube internal surface is first sulfonated by filling a 5 ft length (as supplied) of the tube with 80 % (w/w) H_2SO_4, sealing both ends with hot-melt adhesive and keeping it at 70 °C for 120 h. At each terminus, 1 cm of the tube is then cut off, the liquid inside purged out by N_2 and the tube is flushed with deionized water (DIW) for 30 min. The cleaned surface-sulfonated tube is then coated with AS18 anion exchange latex suspension (65 nm particle diameter, courtesy Thermo Fisher Scientific, the 10% w/v supplied suspension is diluted 10-fold before use) by pneumatically pumping the suspension back and forth for ~40 min whereupon the latex attaches electrostatically to the oppositely charged wall. The column was then flushed with DIW for 30 min to remove all unbound latex particles. Before use, the column is trimmed to the desired size and converted to the OH^--form by pumping 10 mM KOH through it for 30 min. The measured AEX capacity of such a column was ~30 peq/mm^2.

4.2.7 Ion Chromatography System.

Shown in Figure 4-3 below, the present system uses a 4-nL volume internal loop 4-port injector (IV, C74MPKH-4574-.004, www.vici.com) The digital pressure controller DPC (model P/N 990- 005123-100, Parker, http://ph.parker.com/us/12051/en/oemepminiature-pressure-controller) uses nitrogen pressure as input and provides programmable pressure to the DIW reservoir (which can also be rapidly vented through vent valve VV) that supplies influent water to the nanovolume EG. The EG outlet tube (6 cm long, 25 μm i.d. PEEK) directly connects to injection valve IV, to which the column (750 mm long) is directly connected. The column directly enters the suppressor, this is a simpler version of the electrodialytic suppressor described in ref. 23 but has a single 200 μm channel drilled through a 2 x 2 x 5 mm Nafion block. A tapered column end and a tapered exit capillary are inserted through each end of the channel until the tips are 0.6-0.8 mm apart. The block is immersed in 2 mM H_2SO_4 for chemical regeneration. The suppressor exit tube (25 μm i.d., 360 μm o.d.; 12 cm long PEEK) directly enters an admittance detector (TraceDec, www.istech.at); a 75 kHz probe frequency was used.

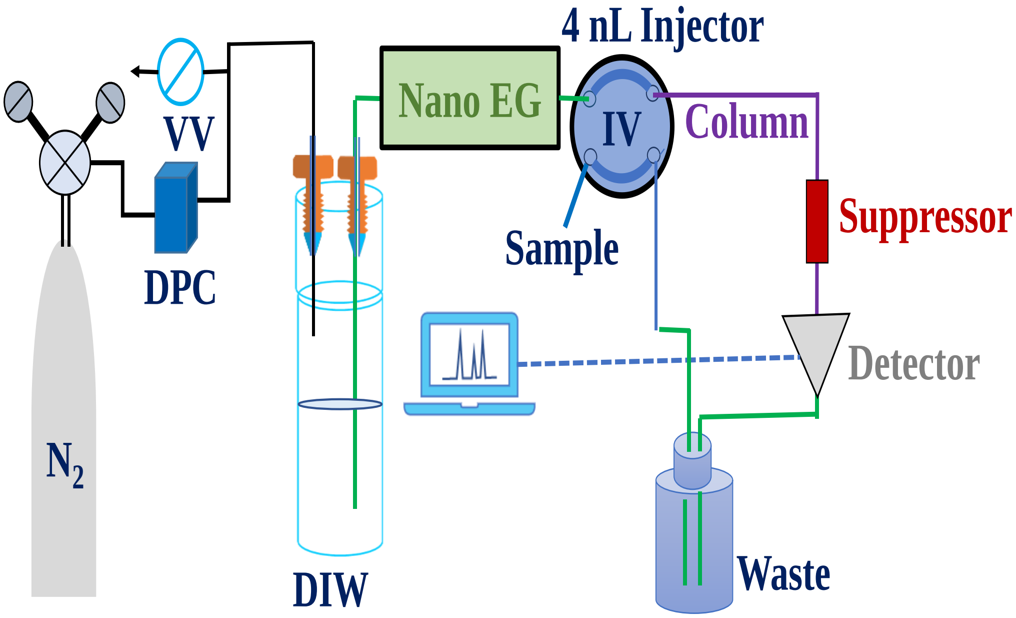

Figure 4-3 OTIC test system schematically shown. For gradient operation, the source meter is capable of a linear sweep gradient or other programmed time-stepped gradient operations. The operation of the PSoC as a programmed current source is itself of capable of minimum current steps of 125 nA but the maximum possible applied voltage is 5 V. With auxiliary circuitry, greater voltage and a 5 nA step resolution (22 µA maximum current or 4x higher with 4x poorer step resolution) is possible, see SI.

4.3 Results and Discussion

4.3.1 Enhanced Water Dissociation at High Field Strengths.

The Wien effect manifests itself by the increase in conductance of an electrolyte solution under high field strengths. For a weak electrolyte there are two different underlying processes,[104,105] often referred to as the first and second Wien effect. It is well known that an ion in aqueous solution is surrounded by oppositely charged ions (ca. the ion atmosphere[106]) which shields it from fully experiencing the external electric field. In a high enough electric field, an ion (whether derived from a strong or weak electrolyte) moves too fast for an ion atmosphere to fully form around it, effectively increasing exposure to the field and thus increasing the observed mobility. The second Wien effect pertains only to a weak electrolyte, which can always be regarded as a polarized/polarizable molecule with a non-zero dipole moment. It is intuitive that ionization will be facilitated whenever such a molecule is oriented appropriately in a high enough electric field. Although the effect has been quantitatively measured for classic weak electrolytes such as CH_3COOH or $ClCH_2COOH$[107] or more esoteric ones such as $HgCl_2$,[108] it has never been measured for water. The first Wien effect would be especially interesting for water because it is well known that unlike for other ions, the mobilities of H^+ and OH^-, the primary charge carriers derived from water ionization, rely on a charge hopping mechanism[109,110] where involvement of the ion atmosphere should be different than with other ions. Essentially all of the experimental measurements on the Wien effect were based on low μs duration, single shot high voltage (up to 20 kV) pulses between two electrodes typically placed at mm-scale distances and evaluating the conductance from the decay curve.[111] Alternatives that involve much lower voltages between electrodes separated by μm scale distances have long been available but the experimental study of the Wien effect has ceased to be an area of interest. However, dated as they may be, extant experimental data suggest that the effect quantitatively differs from one analyte to another even for strong electrolytes. The magnitude of the overall effect is certainly expected to differ further for weak electrolytes as their individual dissociation constants differ[107] making a revisit worthwhile as this may potentially be used in the future for confirming analyte identities. Figure 4-4 shows our experimental data for water.

A field-enhanced increase in the specific conductance of water clearly begins by a field strength of 10^5 V/m whereas below a field strength of 7×10^4 V/m, the specific resistivity remains nominally at 18 MΩ.cm, the usual low-field value for pure water. The exact quantitative estimation of the field strength is admittedly dependent on the micrometer accuracy, and the parallelism of the electrodes but the observed effect is clearly dependent on the field strength rather than the absolute value of the applied voltage as the breakdown occurrence begins almost as the same field strength in all cases while the interelectrode distance is varied over a 25 x range. These observations, augmented by others, such as that within experimental uncertainties, the results were the same if the electrodes were Rh-plated, or the water flow rate was modestly changed (both of which would change the effect of any corrosion products on the observed conductance), as well as pre/post microscopic examination of electrode surfaces, testify to lack of involvement of electrode corrosion products accounting for the observations. AC (bipolar pulse) measurements show a similar effect but at nominally higher fields (See Figure C-S7 in the SI).

In BPMs, it is often argued that the field strength in the interfacial layer may be as high as 10^8 V/m (this is the highest sustainable field before the dielectric breakdown of water) with 0.8 V applied,[112] implying an interfacial layer thickness of <10 nm. There has

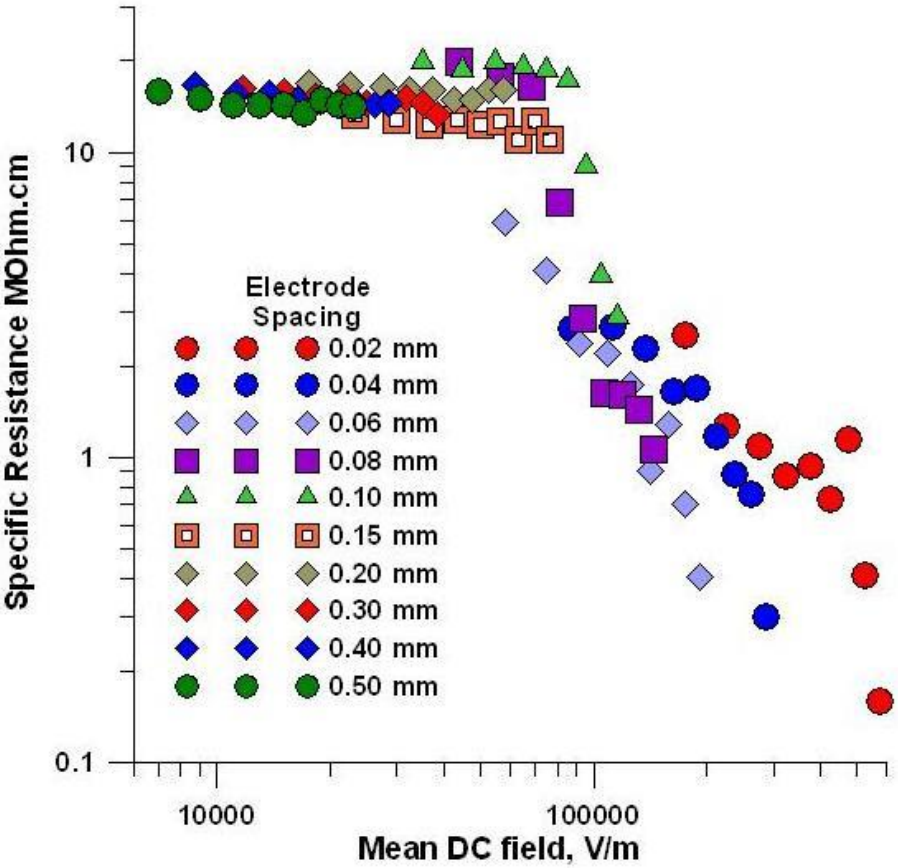

Figure 4-4 Enhanced dissociation of water as a function of applied DC Field. Note at low fields, the expected resistivity is observed.

never been any experimental evidence for this, nor the need for the field strength to be this high has ever been justified other than theoretical expectations. The present data indicate that the interfacial layer need not be so thin, enhanced ionization is actually observed at much lower field strengths.

4.3.2 Packed Columns to Open Tubes in Ion Chromatography.

A typical flow rate for a 4 mm packed column is 1 mL/min. Assuming the packing fraction is 0.64, the linear velocity is 3.7 mm/s. In an open tube of 25 μm ϕ, a flow rate of 200 nL/min represents a linear velocity of 6.8 mm/s, ~2x higher. Previous OTIC studies[113] have shown that these systems exactly follow the simplified Van Deemter equation (without the A-term), enabling the determination of the analyte mobile phase diffusion coefficient D_m from the plate height minimum. For chloride, the computed D_m was in perfect agreement with the known diffusion coefficient; the optimum velocity (u_{opt}) for a 20 μm ϕ column was determined to be ~1.1 mm/s. The Gormley-Kennedy equation[114] indicates that mass transfer efficiency is independent of the diameter of the tube at the same volumetric flow rate, u_{opt} for a 25-μm ϕ column should be ~0.7 mm/s, almost an order of magnitude lower than operational flow rates presently used. Packed column practitioners also need to appreciate the great difference in the effective eluting power of the same concentration of an eluent even when the nature (type) of the stationary phase is the same in an OT column.[115] Consider a 4x250 mm AS18 column that has a stated capacity of 285 μeq/column. If we assume chromatography is being conducted with 10 mM KOH, the stationary phase is in equilibrium with 11.3 μeq KOH present in the 1.13 mL void volume of the column. This is a static ionic equivalents phase ratio (stationary/mobile) of 285/11.3 ≈ 25. An 1-m long 25-μm ϕ OT column, of 230 peq/mm^2 surface ion exchange capacity has an overall capacity of 2.4 neq/m and given the internal volume of such a column being 0.49 μL/m, 10 mM KOH will make the same phase ratio to be 0.47, favoring the mobile phase some 50x compared to the packed column case. The difference in higher linear velocity is largely offset by the longer column lengths used in OTIC. Thus, while the concentrations generated and used here for OTIC are much smaller than their packed column counter parts, the eluting power covers the range of what is used in the macroscale.

4.3.3 Characterization of the Eluent Generator.

For 25-μm ϕ OT columns, typical flow rates we use are 150-200 nL/min. The EG was therefore operated near the high end of this range. The back pressure, well below 50 psi, is well tolerated by the reinforced membranes used and no significant transmembrane loss of water is observed even at 100 psi. Electrical characteristics and generated KOH concentrations are shown in Figure 4-5. Note that the power consumed ($i*V$) is not linearly related to i^2, as the rising concentration of the EG KOH in the generator cavity decreases the solution resistance proportionally (but not the membrane resistance) and there is a finite threshold for the electrolytic breakdown voltage. The computed temperature rise is the maximum possible in that it assumes that the eluent flow is the only coolant and ignores the cooling effect of the substantially larger feed KOH flows on the other side of the membrane. In any case, this rise is negligible.

EG [KOH] increases linearly with the applied current (Figure 4-5). Faradaic behavior would mandate the generation of 3.17 mM KOH/μA for a flow rate of 0.196 μL/min. The observed slope of 2.26 mM KOH/μA represents a current efficiency of 71 %. The efficiency is less than ideal because of two reasons. First, a parallel current path exists between the two feed reservoirs through the recirculation loop. This can be eliminated by operating off independent reservoirs not in fluid contact. In the present case

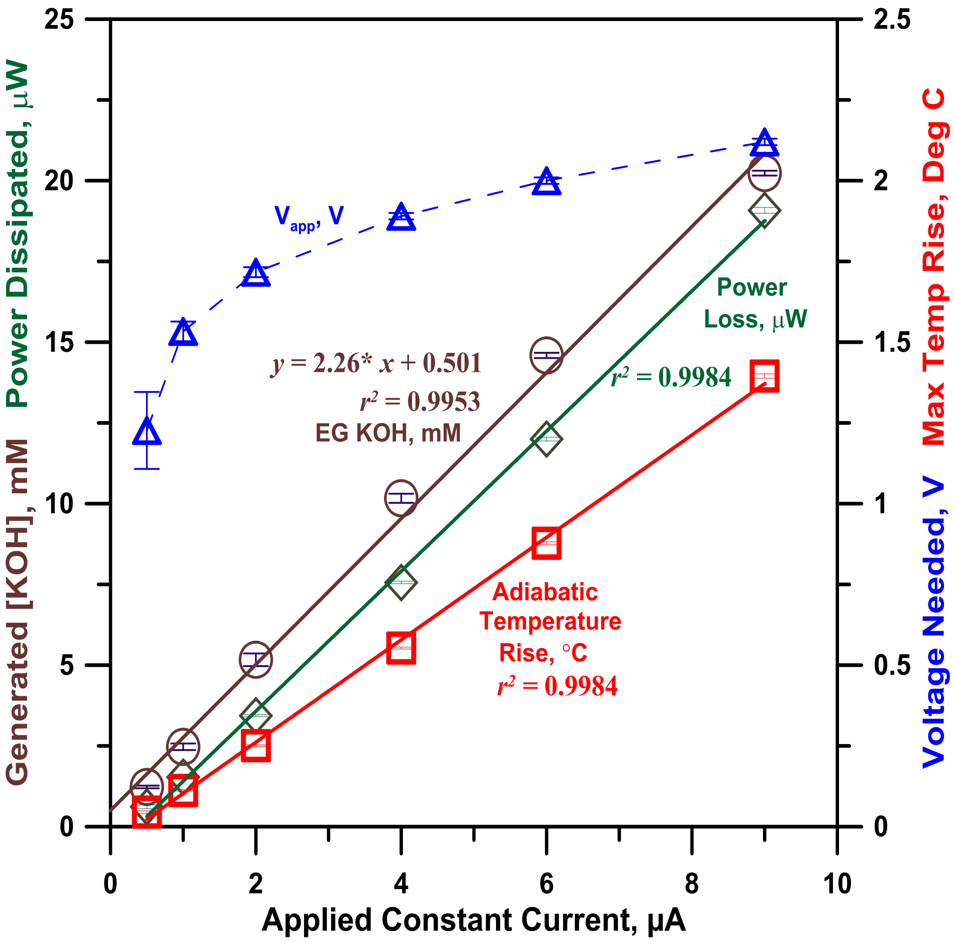

Figure 4-5 Operational characteristics of the nanovolume EG; flow rate 196 nL/min. Solid lines: linear fits, Dashed line: spline fit. The temperature rise is computed from the dissipated power (*i***V*) for which the eluent flow is assumed to be the only sink.

we opted to retain this arrangement, as efficiency was still relatively high and was constant over long periods. If one desires to reduce the internal EG volume further and the cross cavity is not bored out, the EG resistance will increase, increasing the relative importance of the parallel path via the recirculation loop. In this case, direct electrical contact through the recirculation loop will need to be eliminated. The second reason of less than quantitative current efficiency lies in the intrinsic behavior of BPMs themselves.[116,117]

4.3.4 Open Circuit Penetration (OCP).

The current – EG [KOH] relationships indicate that at zero current a 0.5 mM KOH output is predicted. Even when a power source is not connected to the system, some KOH appears in the generator output; we refer to it as the OCP or zero current penetration (ZCP) value. The high [K^+] gradient across the CEM results in some K^+ - H^+ exchange on the EG product side. The OCP value increases with increasing feed [KOH] and decreasing membrane thickness. With 0.2 M KOH feed and 0.2 μL/min influent water flow, the measured OCP was 0.25 mM. While this value would be acceptable in most applications, the minimum [KOH] from the EG can be reduced by decreasing the feed concentration or increasing the CEM thickness (or using multiple layers of it). In the present case, incorporating an additional CEM disk on the CEM feed side (a layer of two membranes rather than one) reduces the open circuit specific conductance of the output to 26.8 μS/cm @178 nL/min, tantamount to just below 0.1 mM KOH. Unlike conventional generators based on a single membrane (or a single stack of CEMs), a reverse potential of 1 V had no effect on the output KOH concentration.

Figure 6 shows multiple traces that illustrate the generator characteristics, including output stability over several hours, gradient response times (40 mm long 25 μm i.d. tube connected to the EG output) and duration of operability with a static feed KOH solution. The experimental data were obtained at 22 °C; data relating specific conductance to KOH concentration appear in Table C-S1 in the SI. Additional values, computed from (mostly) higher concentration literature data suggest the specific conductance of 10 mM KOH to be 2290 and 2430 μS/cm at 20 and 25 °C, respectively,[118] see Table C S2. The lag time (the interval between an applied current step and a change in the generator output first becoming discernible) was ~30 s. The 10-90% rise time at the operational flow rate (180-190 nL/min) was ~3.5 min. This would be much greater if a degasser had to be used. An even faster response may be desirable as a future improvement; this should be possible with a further reduction in generator internal volume. The 90-10% fall time (5.7 min) is considerably higher than the rise time but this is of little consequence in actual chromatography and can be easily reduced by increasing flow rate after the desired run period is over. Results for triangular or square wave current ramps applied to the generator are illustrated in Figure C-S8 in the Supporting Information. Our intended application for an eventual complete chromatographic module is in extraterrestrial applications. In this case it is not anticipated that a large number of samples will be available for analysis at any one time. Rather, it is likely that once a given sample (extract) is analyzed, perhaps in a replicate fashion, the instrument will hibernate for a period before another sample is available. As it is vital in such applications to minimize system architecture, it was of interest to know the limitations of operating without feed flow: how long can the system generate a constant concentration of an eluent before the feed solution behind the CEM is depleted enough to affect the generated concentration?. At ~5 mM KOH level, an isocratic eluent concentration typically used in our systems, the EG can produce a constant eluent concentration for >1 h without requiring any feed flow. As the concentration is replenished by diffusion if

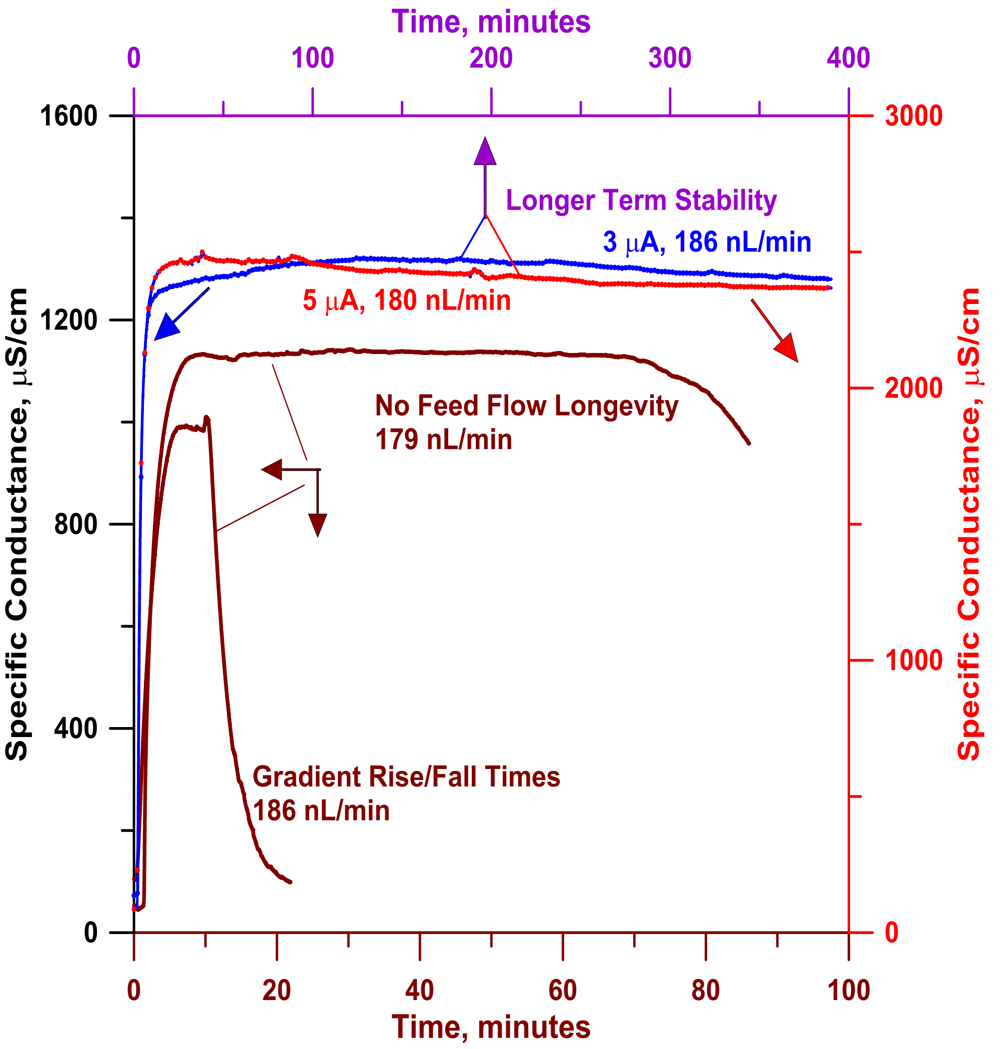

Figure 4-6 Nanovolume EG characteristics. Top two traces depict long term stability (top abscissa), with drive currents of 3 µA (blue trace, left ordinate) and 5 µA (red trace, right ordinate), respectively. Of the lower two traces (brown, both bottom abscissae, left ordinate), the lowest one illustrates step gradient rise and fall times while the other illustrates stable operation for < 1 h without feed KOH flow.

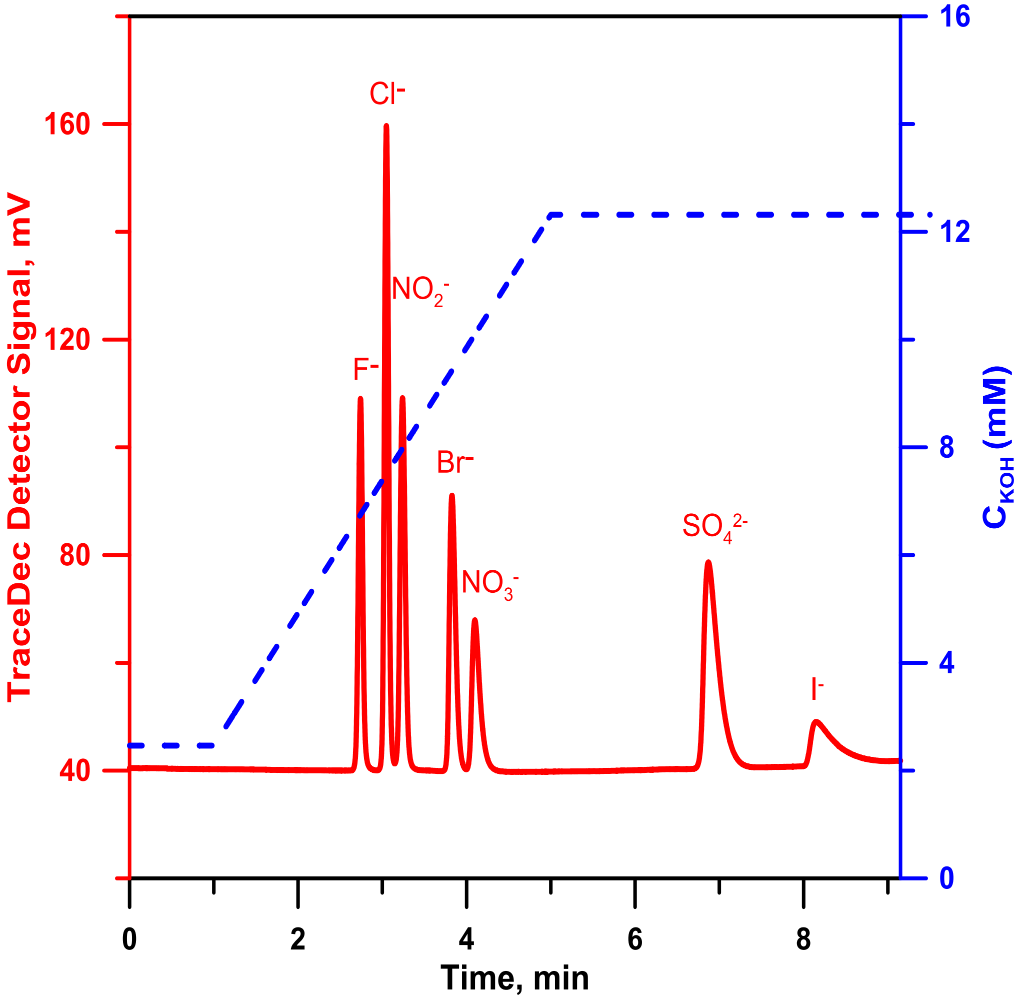

Figure 4-7 Gradient separation of mixture of anions using eluent generated KOH and suppressor placed ahead of the detector. Column: sulfonated PEEK tube coated with AS 18 latex nanoparticles, 360 µm o.d., 25 µm i.d., 750 mm long; analyte concentration: 200 µM each; Flow rate: 180 nL/min. Injection volume: 4 nL. TraceDec Detector settings: Voltage: 0 dB; Frequency: 75 KHz; Gain: 200 %, Offset: 0.00. The detector probe is situated at the exit PEEK tube at ~4 cm away from the center of the suppressor. Linear gradient expressed as time, min and (KOH concentration, mM): 0 (2.5), 1 (2.5), 5 (12.3), 9 (12.3), 9.5 (2.5).

sufficient time is allowed before next use, feed solution flow is not essential. Much as is done in commercial macroscale EGs, providing a greater reservoir volume behind the CEM compartment and an orifice for gas exit may be all that is needed for prolonged static operation.

4.3.5 Chromatography

The performance of the device was tested using both isocratic and gradient modes to separate a mixture of inorganic anions. Under isocratic conditions, retention time RSDs varied from 0.4 % to 0.6 % for six consecutive injections. For gradient separation, the corresponding RSDs (n = 3) ranged from 0.4 % to 1.2 %. Considering the fact that the retention time also depends on the flow rate, this performance suggests good eluent generation stability. Figure 4-7 shows a representative gradient chromatogram for the separation of a mixture of anions.

4.4 Conclusion

We have demonstrated the feasibility of an eluent generator suited for open tubular ion chromatography without splitting the flow of the generated eluent. The generator is miniaturized within a 1 cm x 1 cm LabSmith microfluidics cross and optionally two more similar tees are used for KOH recycling. This has opened the door that the generator can be a part of an efficient, automated, compact portable Ion Chromatographic (IC) system for on-site analysis of ions, which is one of our future goals. This will eliminate the need of preparing KOH manually and because of the small volume of the device, it can readily be used for gradient chromatographic separation using small bore open tubular columns.

Chapter 5

SUMMARY AND FUTURE WORK

5.1 Summary

In this dissertation, a new technique was explored to measure the total light energy absorbed. In contrast to the existing methods for photothermal absorbance measurement where heat generated is detected by measuring either refractive index changes or electrical conductivity changes, it was shown that the heat change can be measured directly. The change in the temperature of the solution was detected by using a single, two-junction thermocouple wire. The complete detection system, including associated electronics, is small and simple. While the utility of the device as a detector in a liquid chromatography system was established, it can also be used in microthermometry, for example, to measure the quantum efficiency of fluorophores and many other applications where a small change in temperature is to be measured in a microscale flow system.

Open tubular ion chromatography was conducted using solution-contact conductivity measurement in small-bore capillaries. Different end-column conductivity cell geometries were investigated to test the degree of dispersion. The data also established the superior sensitivity and linearity of such detectors over commercially available admittance detectors on a fully suppressed background, especially at the low end of analyte concentrations. The feasibility of using end-column solution contact conductivity measurement in capillary scale open tubular ion chromatography was clearly demonstrated.

This dissertation also describes the design, construction, and successful characterization of a Nanovolume EG appropriate for use in an open tubular ion chromatography system. The EG is very compact and small, a suitable component of an efficient, portable, and automated ion chromatography for remote applications. This EG is first of its kind to be coupled with an OTIC system for executing isocratic and gradient separations without flow-splitting.

5.2 Future Work

Directly measuring the temperature change resulting from light absorption using a simple, low-cost device was an important achievement. But to be competitive with current absorbance detectors, future work should center on improving how small a temperature difference can be measured. An order of magnitude improvement over the present system would be desirable. Similarly, the solution-contact conductivity cell design needs to be further improved as the presently described cells still leads to measurable loss of chromatographic efficiency. An easy to fabricate solution-contact conductivity detector for capillary scale IC systems is much needed. Overall, the overarching goal should be to integrate the separation column, suppressor, and the conductivity cell to make a robust working unit; this will facilitate actual commercialization. To be comparable to current packed column systems, open tubular systems also require greater column capacity. This can likely be accomplished in many different ways, increasing the porosity of the column inner wall may be one way to achieve that end.

Appendix A

SUPPORTING INFORMATION FOR CHAPTER 2

EXPERIMENTAL SECTION

Materials

Methanol (HPLC grade, www.emdmillipore.com), Disodium 6-hydroxy-5-[(2-methoxy-5-methyl-4-sulfophenyl)azo]-2-naphthalenesulfonate (Allura red, www.tcichemicals.com), 2-(Phenylazo)chromotropic acid disodium salt (Chromotrope 2R), 5,5′-indigodisulfonic acid sodium salt (Indigo carmine), disodium 6-hydroxy-5-[(4-sulfophenyl)azo]-2-naphthalenesulfonate (Sunset yellow), ammonium acetate (ACS grade, all foregoing from www.sial.com), and Methylene blue chloride (www.alliedchemcorp.com) were obtained as indicated. The dyes were dissolved individually in water to make separate stock solutions.

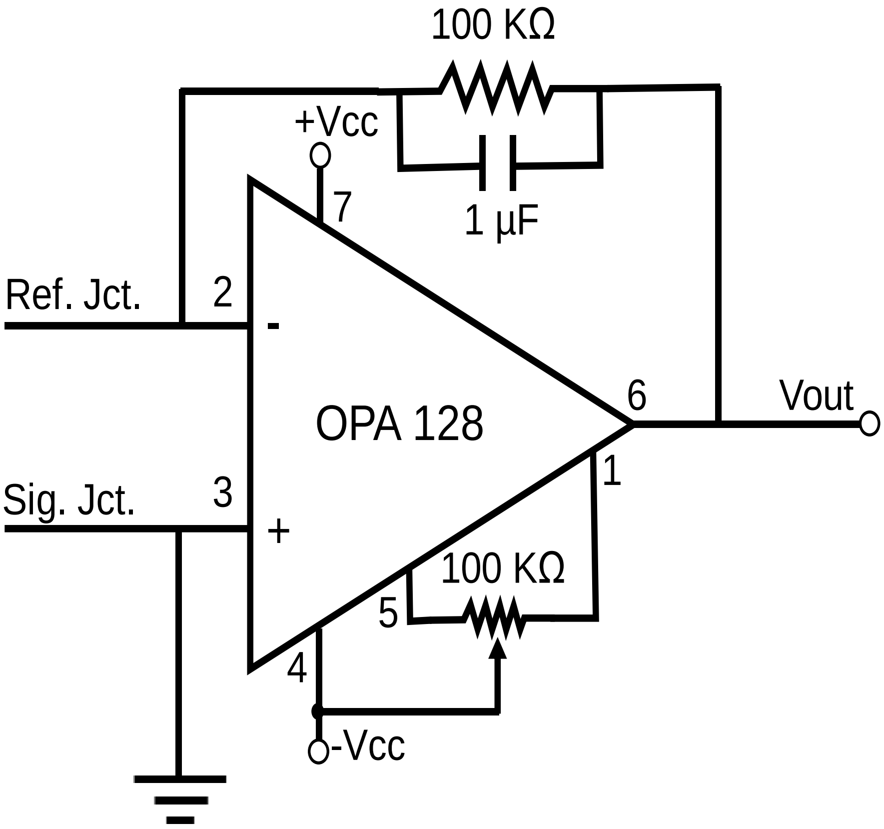

Figure A-S1 Electronic Circuitry. An additional operational amplifier (TL082) was occasionally used to provide additional gain and offset capabilities.

Figure A-S2 The hemispherical lens end fiber is coupled at the large chip LED end to harvest more light into the fiber. More light is coupled into the fiber compared to no modifications, but the gain is less at higher LED currents as the emission angle apparently increases, See Table AS1 below.

Table A-S1 Light throughput gain observed for lens-ended vs. regular optical fiber.

LED driving current, A (voltage, V)	Photodiode reading (mA) for regular optical fiber	Photodiode reading (mA) for optical fiber with lens	% increase in light throughput
0.12 (3.0)	0.94 ± 0.02	1.32 ± 0.03	40
0.48 (4.0)	3.80 ± 0.06	5.05 ± 0.03	33
0.94 (5.0)	7.64 ± 0.05	9.13 ± 0.10	20
1.31 (6.5)	12.98 ± 0.07	14.02 ± 0.04	8

Figure A-S3 The delivery fiber is firmly coupled to the LED chip through a hole in the front plastic face. The LED lead wires are brought out through the sides to connect to a standard power supply.

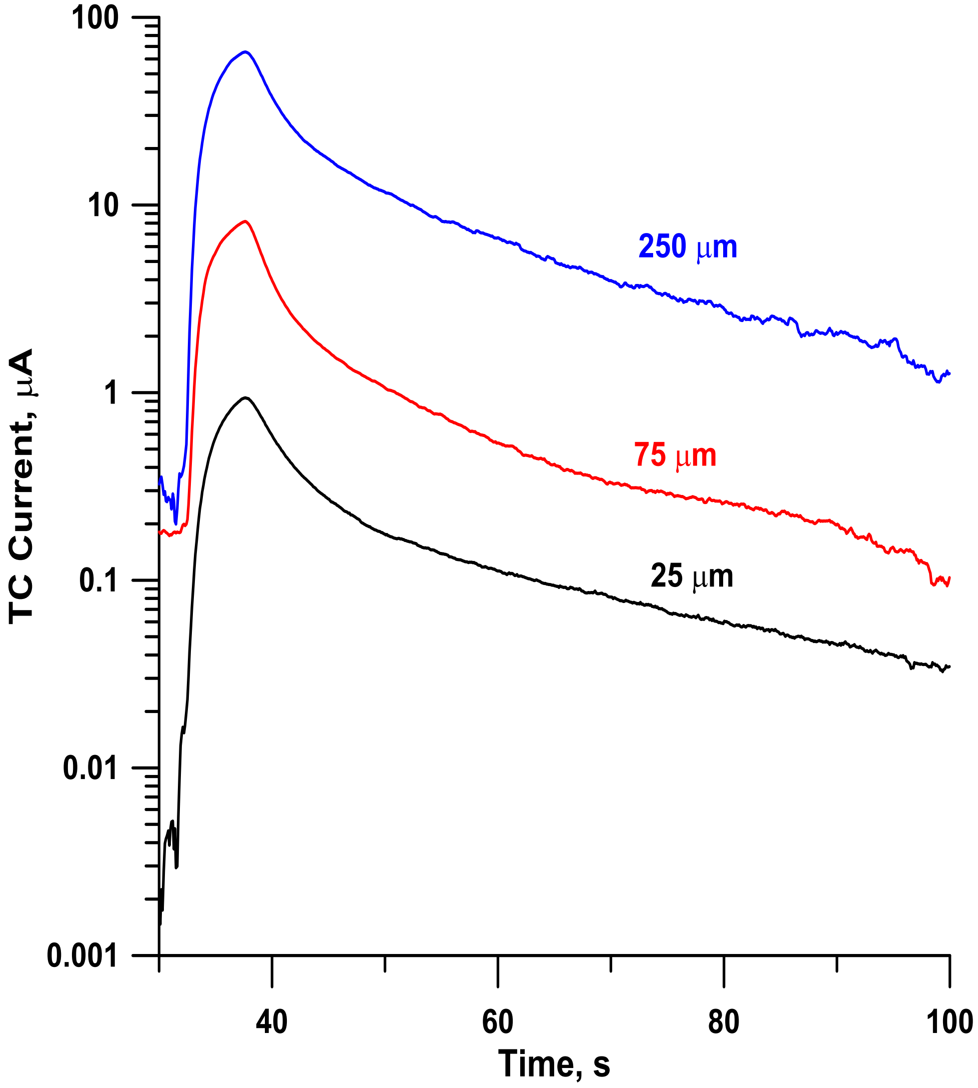

Figure A-S4 Current response of three different diameter iron-constantan thermocouples to a 7.00 V, 5.00 s pulse applied to a 1.00 kΩ thin film SMD resistor Just upstream of the signal Junction in Fig. 2. The pulse was applied at ca. 30 s. The peak positions were temporally synchronized. Note logarithmic ordinate.

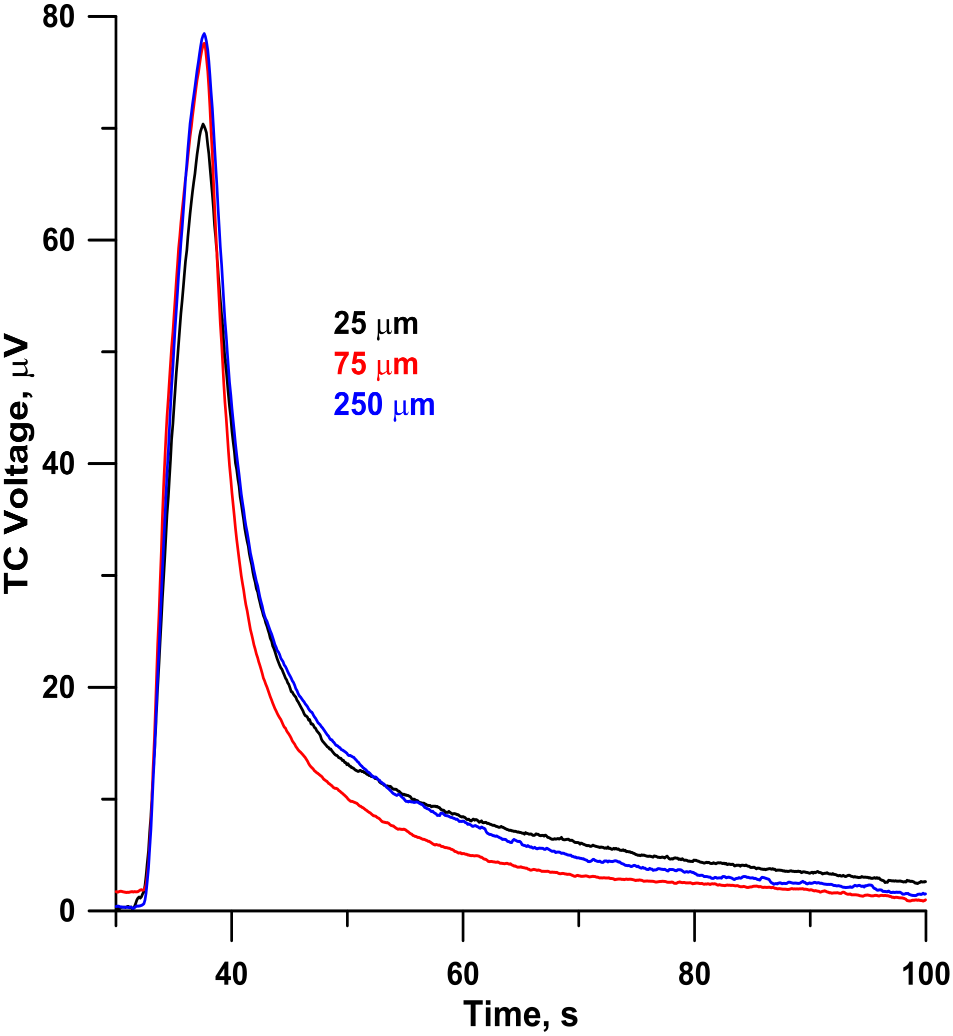

Figure A-S5 Inferred voltage response of three different diameter iron-constantan thermocouples to a 7.00 V, 5.00 s pulse applied to a 1.00 kΩ thin film SMD resistor Just upstream of the signal Junction in Fig. 2.2. The pulse was applied at ca. 30 s. The peak positions were temporally synchronized. The data in Figure 2.3 were multiplied by the resistance of the individual sensor assemblies that were measured at the op-amp inputs.

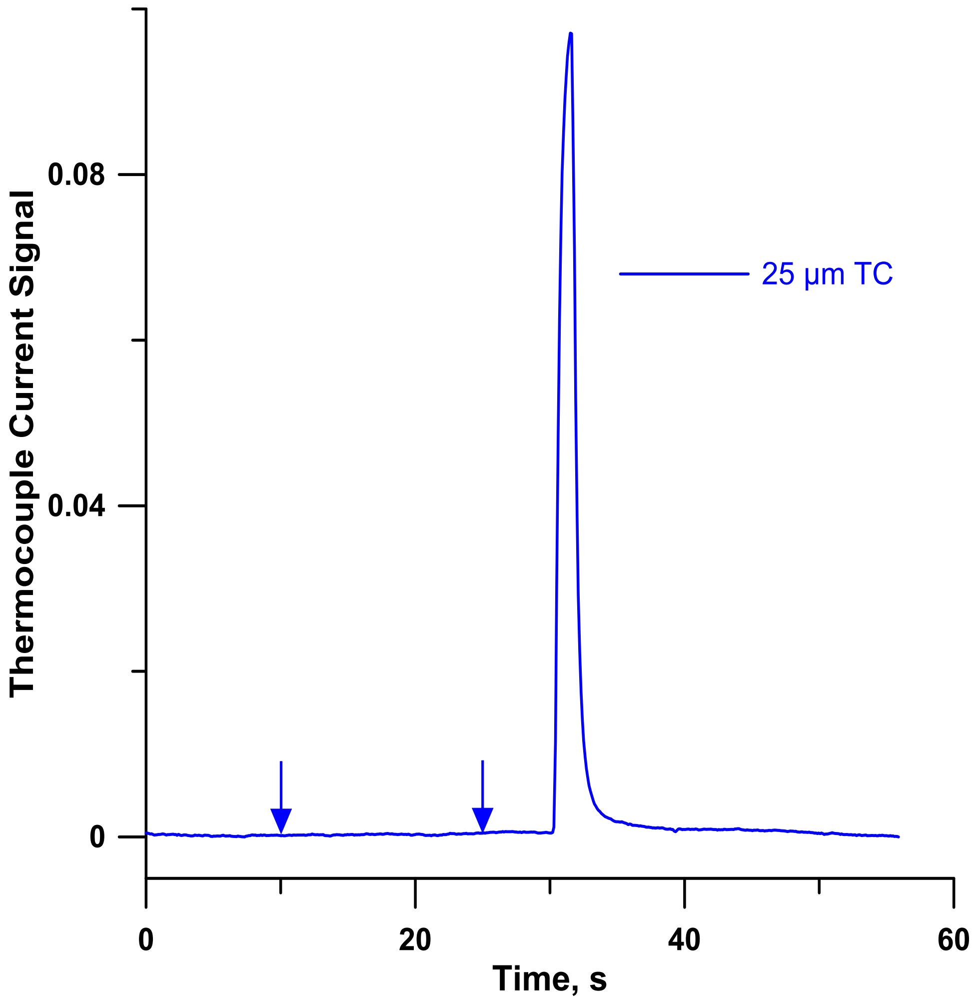

Figure A-S6 The baseline standard deviation is computed in the 15 s interval marked by the arrows prior to the laser pulse.

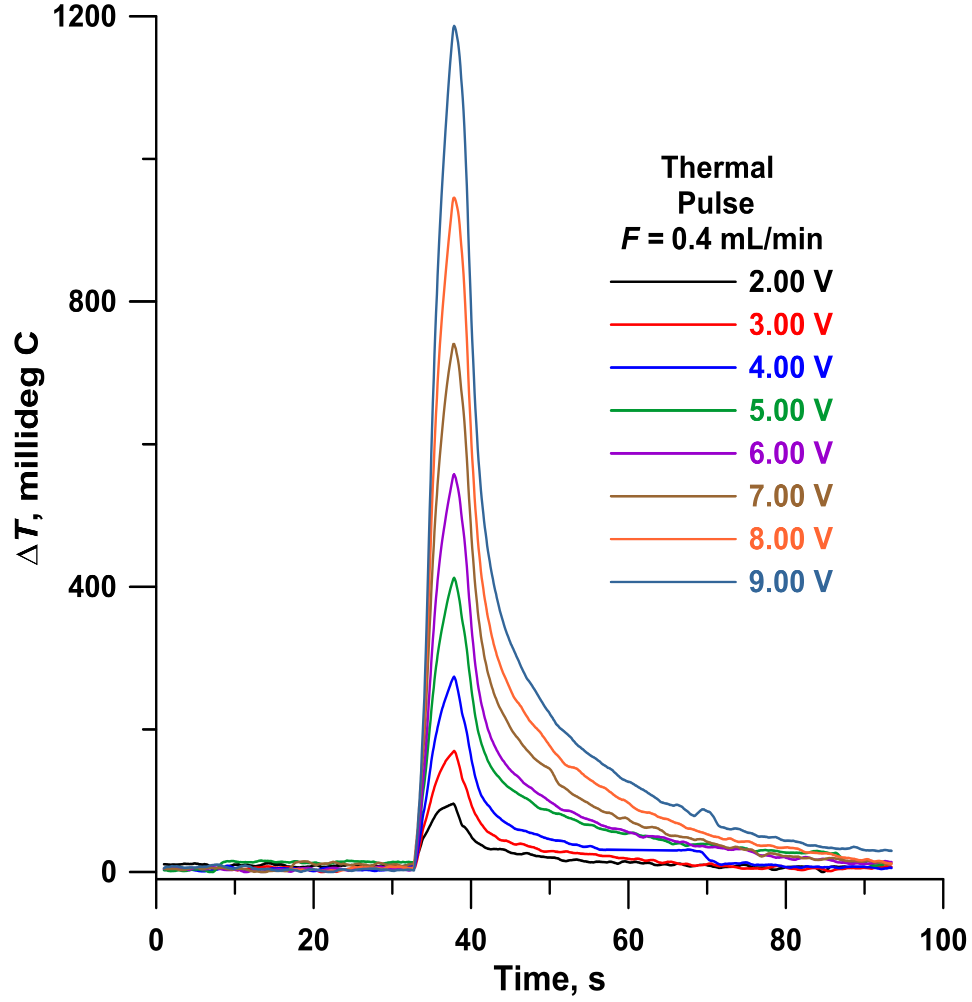

Figure A-S7 Illustrative temperature rise signals from resistor experiment. Flow rate 0.4 mL/min. t_{pulse} = 5 s.

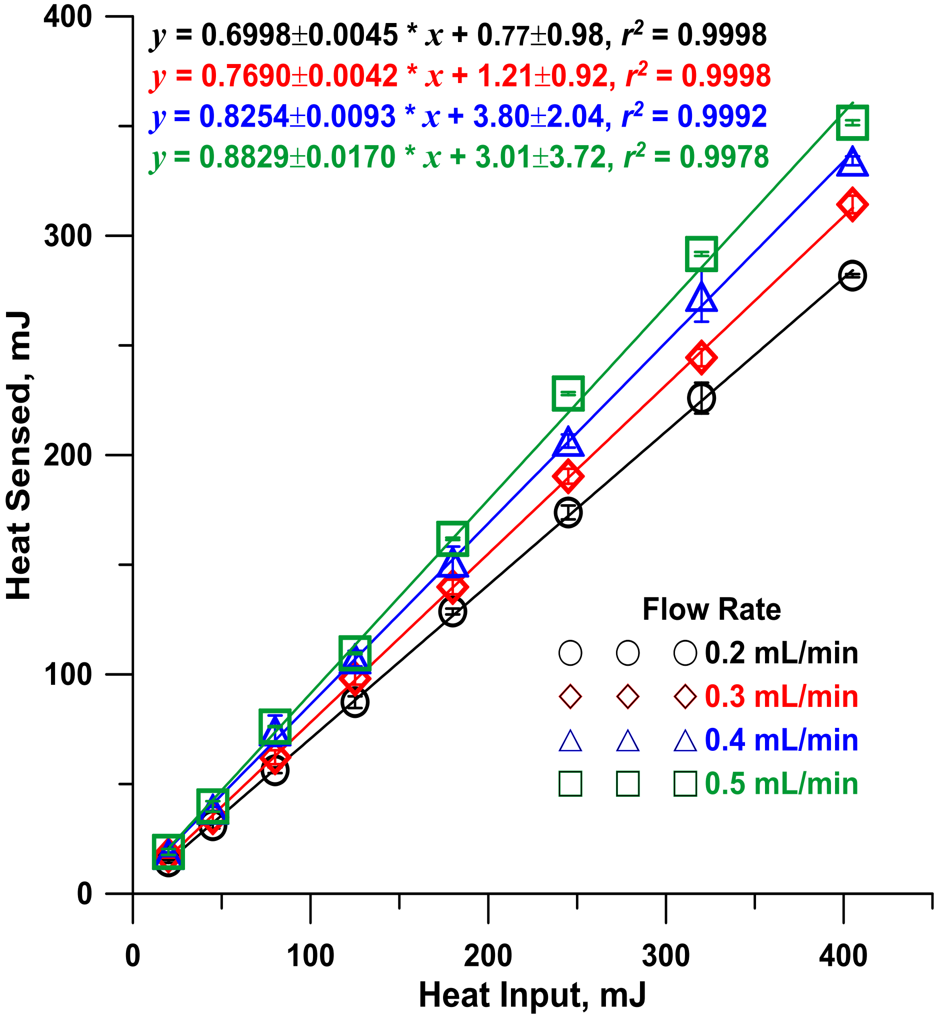

Figure A-S8 Heat recovered as computed from the temperature rise indicated by the sensor (based on peak area of *ΔT* vs. time, See text) vs. the pulsed heat input (as computed from electrical parameters) at various flow rates. The slope of each line represents the fraction of the energy input registered by the sensor; the rest is lost to the wall. Predictably more of the energy input is seen by the sensor at higher flow rates (lower residence time), as there is less time for the heat to be lost to the walls. At a flow rate of 0.5 mL/min, >88% of the input heat is sensed.

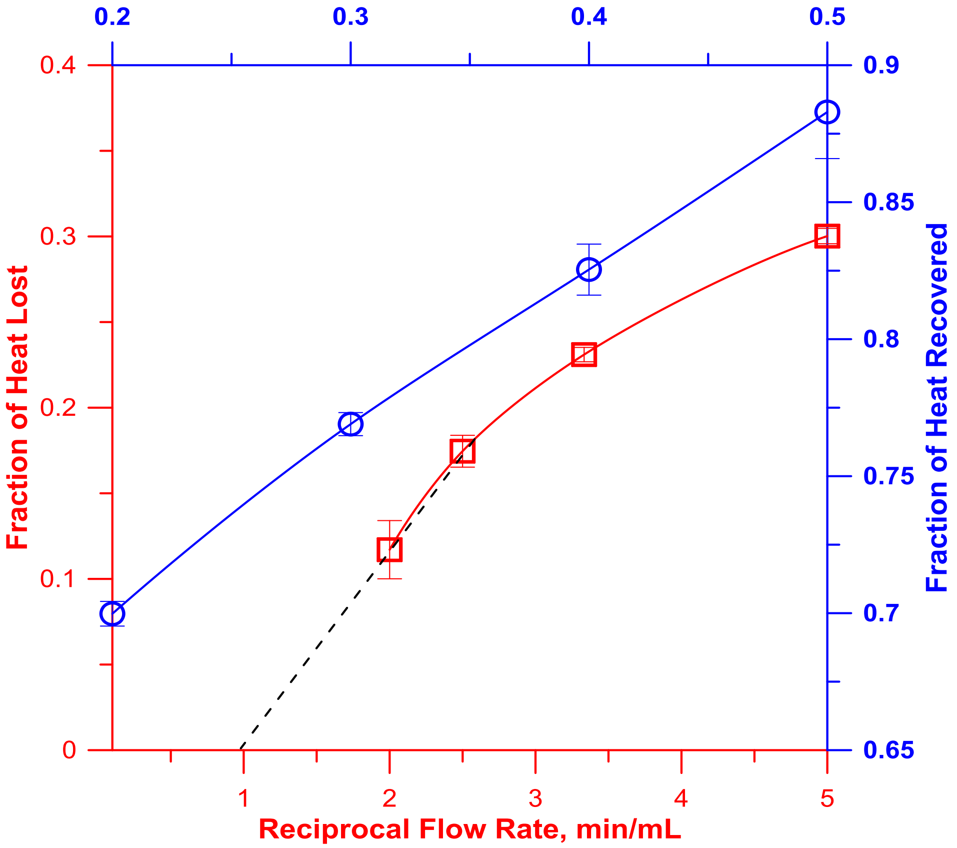

Figure A-S9 Blue trace (top abscissa, right ordinate): Fraction of heat input as sensed by the sensor as a function of flow rate. Red trace (bottom abscissa, left ordinate): Fraction of heat lost as a function of reciprocal flow rate. Note that the abscissa-intercept for a linear fit increase with increasing flow rate. Extrapolating the two highest flow rate points suggests that by a flow rate of ≳ 1 mL/min, a negligible amount of heat will be lost to the walls. This is also the prediction of the Gormley-Kennedy Equation that applies to heat or mass transfer to the walls of a cylindrical tube for the dimensions of the parameters in the present system.

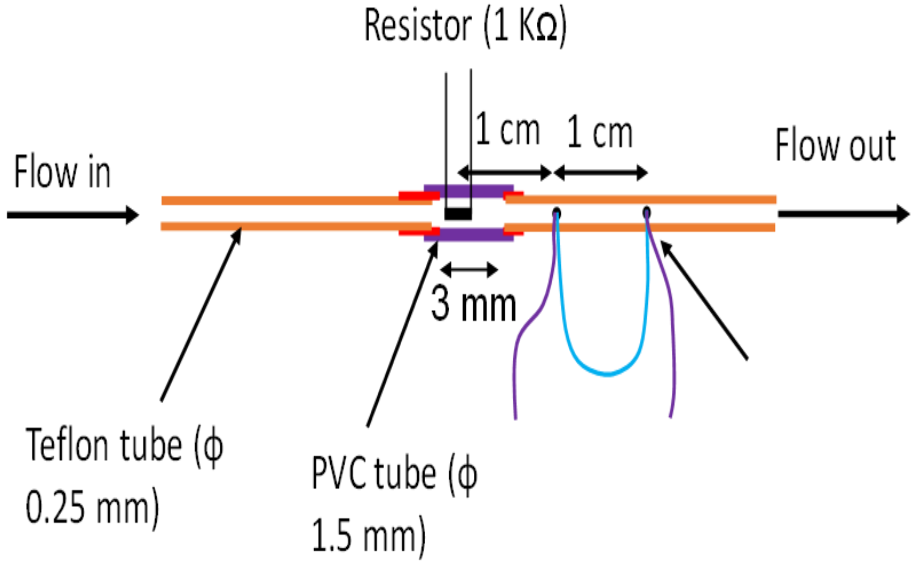

Figure A-S10 Arrangement for the experiment in Figure 2.4 (black trace).

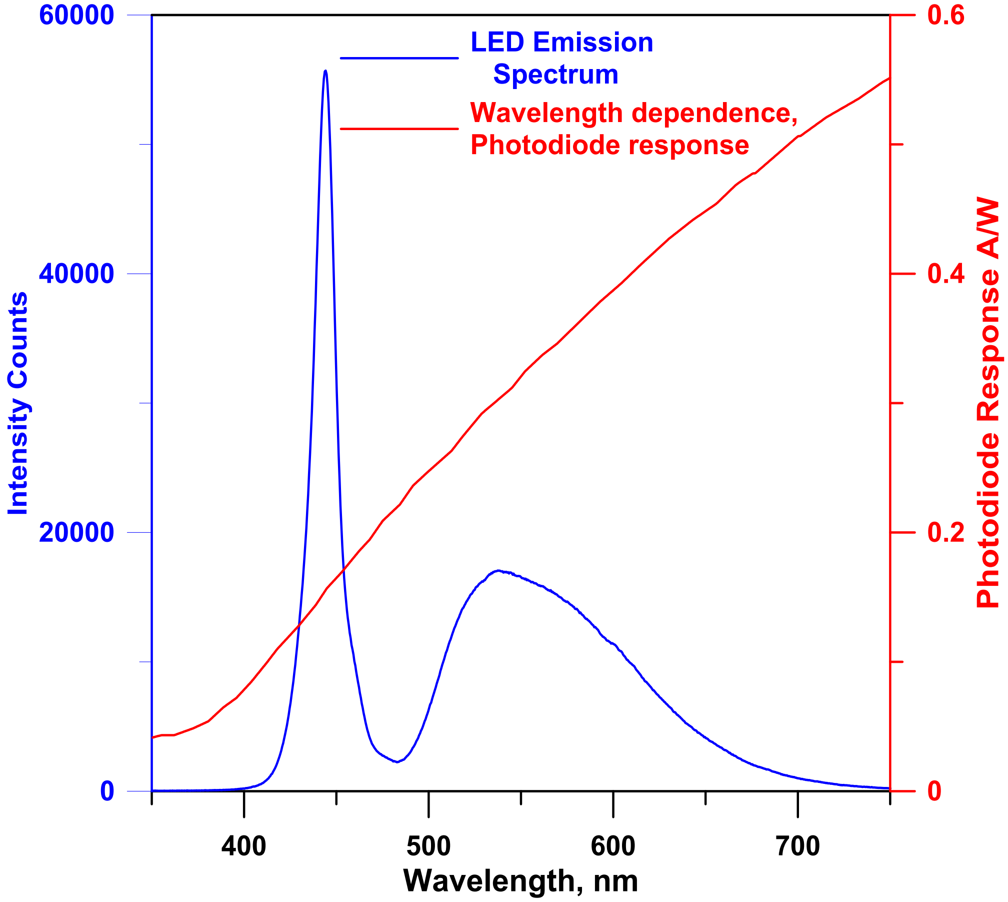

Figure A-S11 LED Emission Spectrum and Silicon Photodiode (in power meter) response as a function of wavelength.

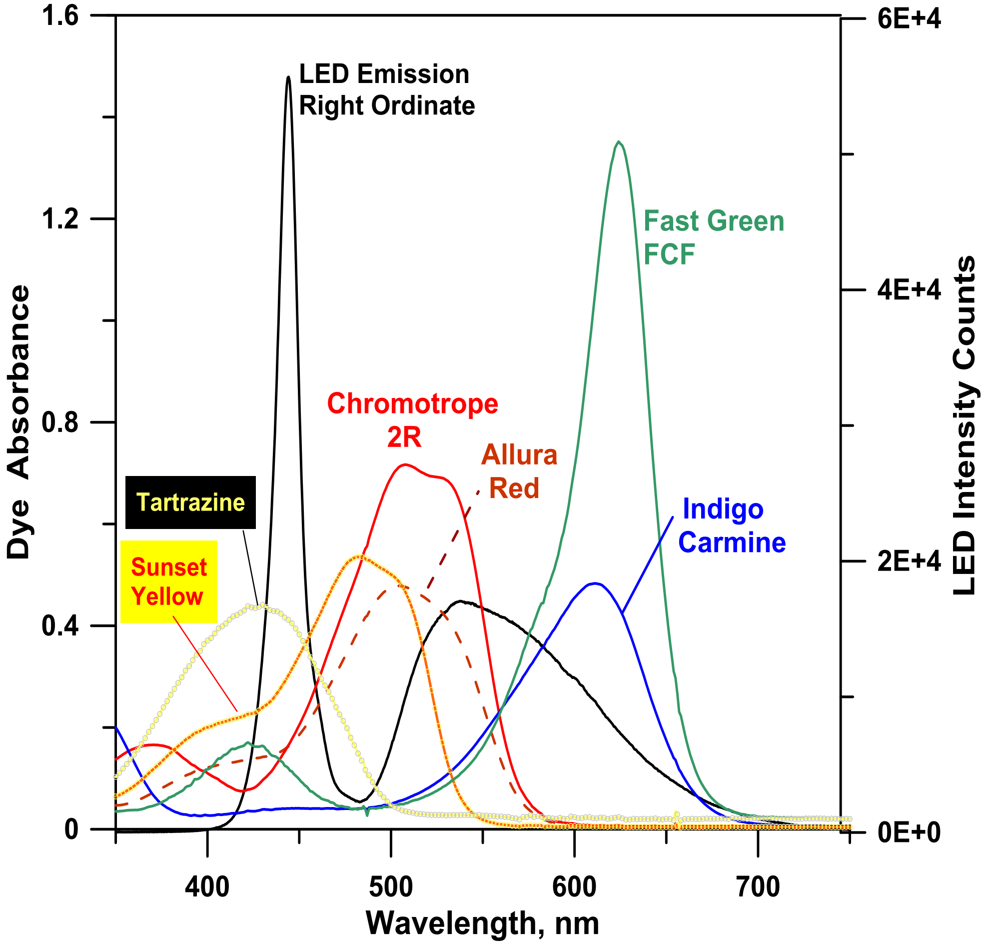

Figure A-S12 The spectral absorption of various dyes (10 mg/L solution, 1 cm pathlength cell) used in the chromatographic superimposed on the LED emission spectrum (right ordinate).

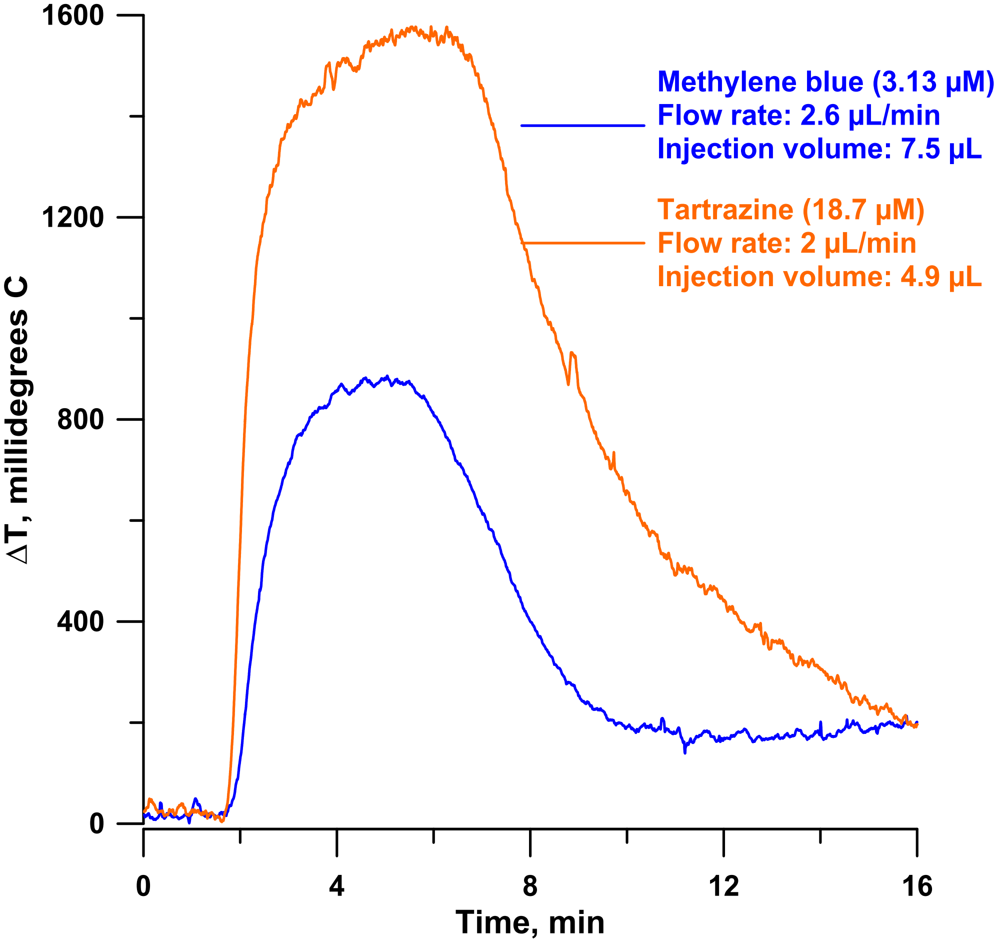

Figure A-S13 Blue trace: Large volume flow injection experiment with 3.13 µM Methylene blue irradiated with 660 nm 19 mW laser. Based on short term (15 s) noise, the S/N was ~300, suggesting an estimated LOD of 30 nM. **Orange Trace:** Similar experiment with 18.7 µM Tartrazine irradiated with a 449 nm 90 mW laser, the S/N was ~540. In both cases, the laser was incident on a 100 µm ϕ capillary and the laser spot size was 0.5 mm.

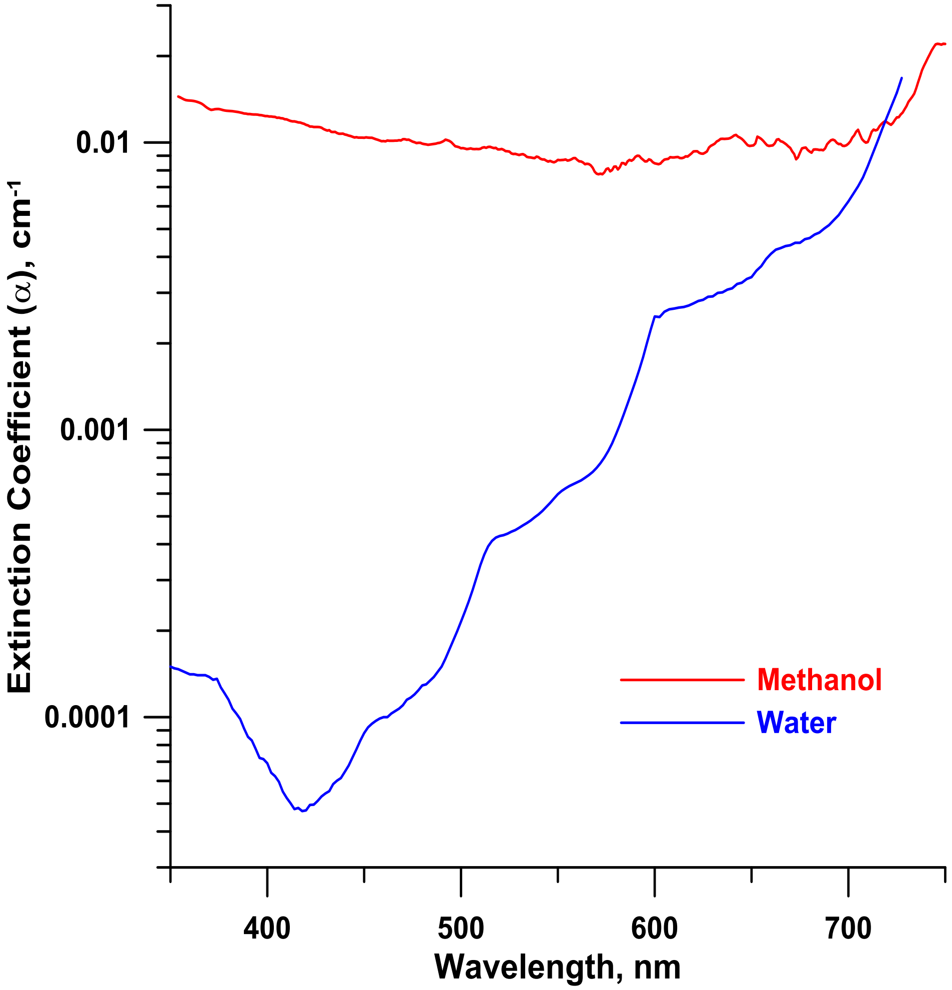

Figure A-S14 The extinction coefficient of methanol and water in the 350-750 nm region, note logarithmic ordinate (Courtesy of Karsten G. Kraiczek (Agilent Technologies, Waldbronn, Germany). Both were HPLC grade solvents; the data were obtained by a pathlength difference measurement technique.

Table A-S2 Observed vs. Model Predicted Effective Quantum Efficiencies for MB[a]

MB, µM	**BTB, µM**	**Q_{eff}**	**Calcd QE**
1.56	11.0	0.565 ± 0.032	0.582
3.13	21.9	0.570 ± 0.034	0.560
7.82	55.3	0.538 ± 0.025	0.510
15.63	110.5	0.431 ± 0.024	0.453

[a] In each row, the MB and BTB solutions have the same absorbance at 660 nm.

(1) Gormley, P. G.; Kennedy, M. *Proc. Roy. Ir. Acad.* **1948,** *52*, 163-169.

Appendix B

SUPPORTING INFORMATION FOR CHAPTER 3

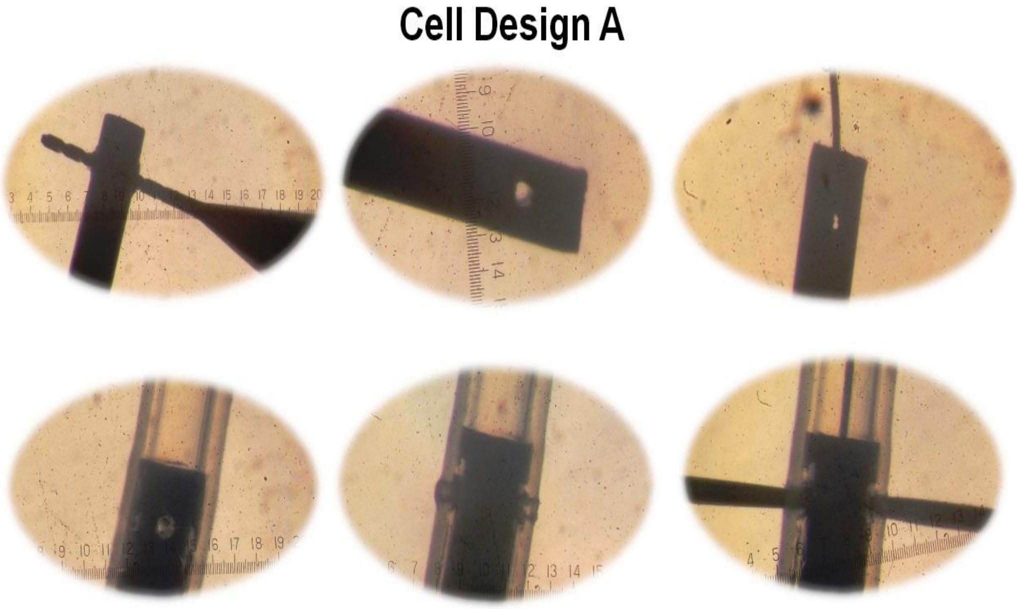

Figure B-S1 Figure 3-1a shows a capillary contact conductivity cell in which two 100 μm diameter tungsten wires are fixed at the very end of a 75 μm i.d., 360 μm o.d. blank PEEK capillary. To prepare such a detector, a 100 μm hole was drilled through the blank PEEK capillary at a right-angle position which is very close to one end of the capillary. This capillary end was then fitted in a thin wall PTFE tubing with an i.d. a little small than 360 μm. A 100 μm drill bit was used to hand-drill through the PTFE tubing along the hole in the PEEK capillary. One 50 μm diameter tungsten wire was then inserted into the 75 μm i.d. PEEK capillary while two 100 μm diameter tungsten wire electrodes were pushed into the drilled hole against the 50 μm diameter tungsten wire from the opposite direction. The two electrodes were fixed in positioned by epoxy. After cure, the 50 μm diameter tungsten wire was pulled out of the PEEK capillary, leaving 50 μm between two electrodes.

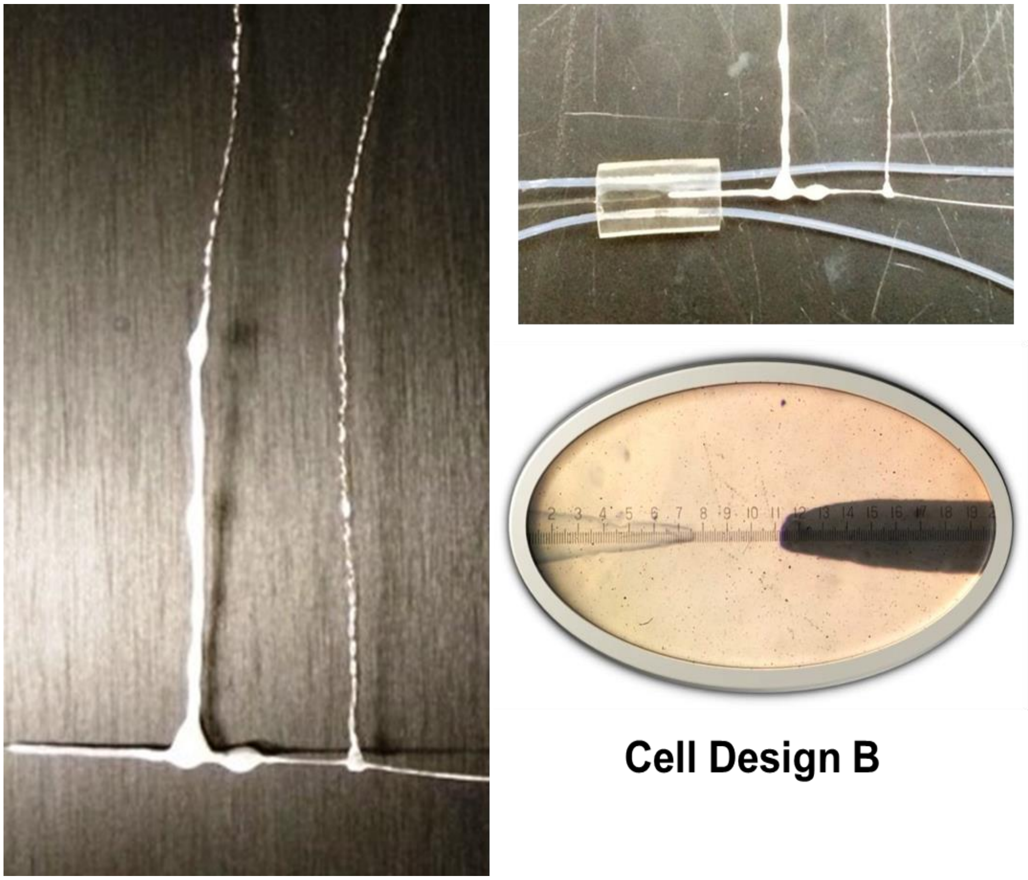

Figure B-S2 Photographs of detection arrangement in Design B.

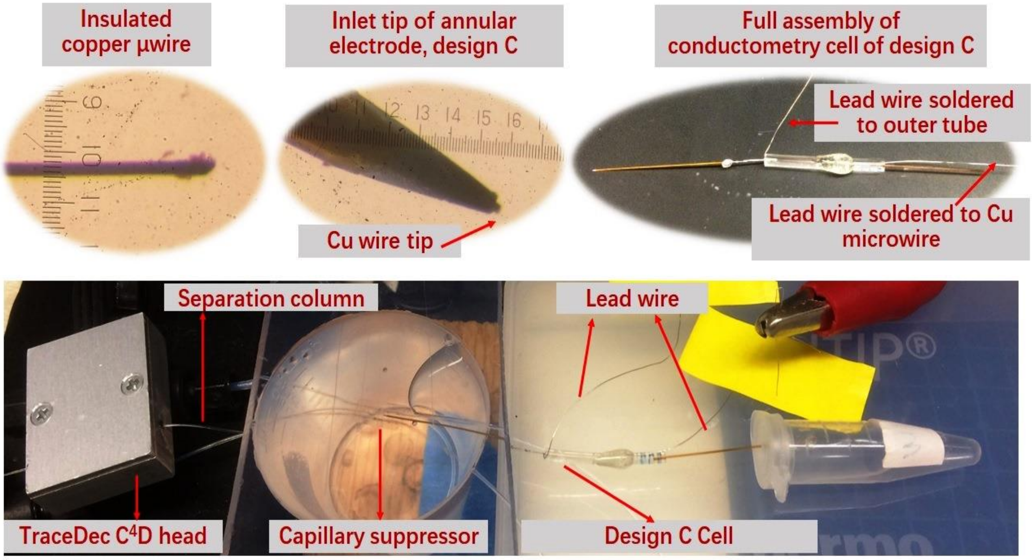

Figure B-S3 Contact conductivity cell of design C assembled with a capillary suppressor.

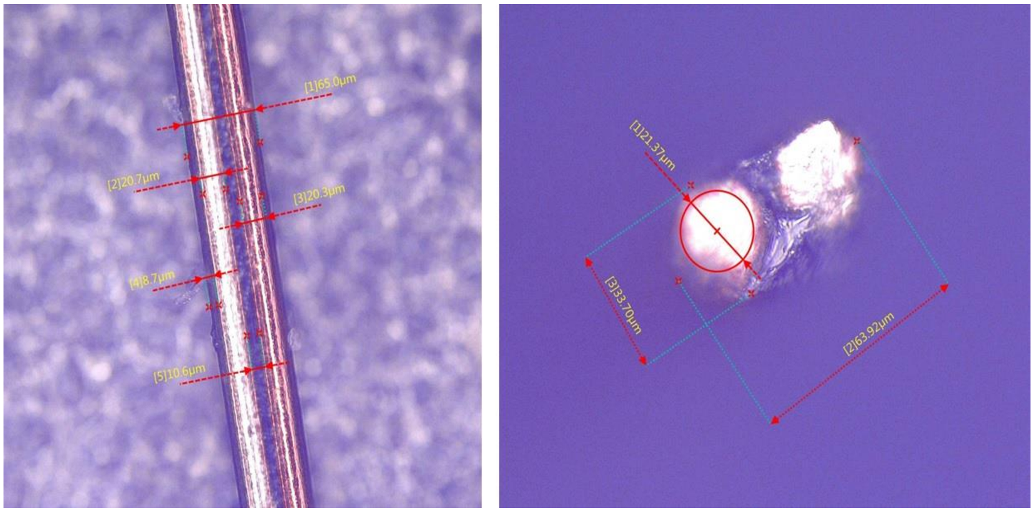

Figure B-S4 Design D. Bifilar wire. Left: Viewed with wide edge flat. Right: Viewed end-on.

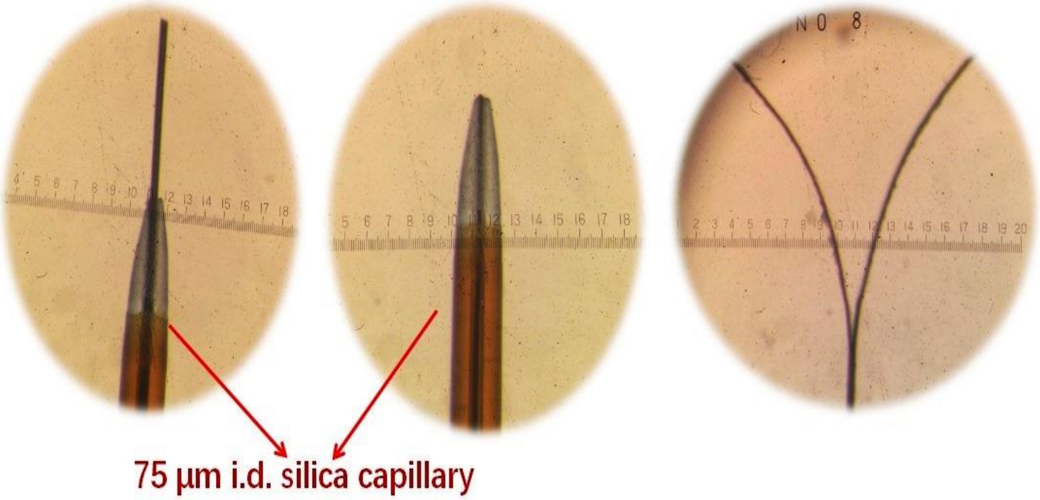

Figure B-S5 Design D probe. Left: bifilar wire protruding from honed capillary tip Middle: Excess wire cut off; Right: Entrance end of wire is split to individual strands.

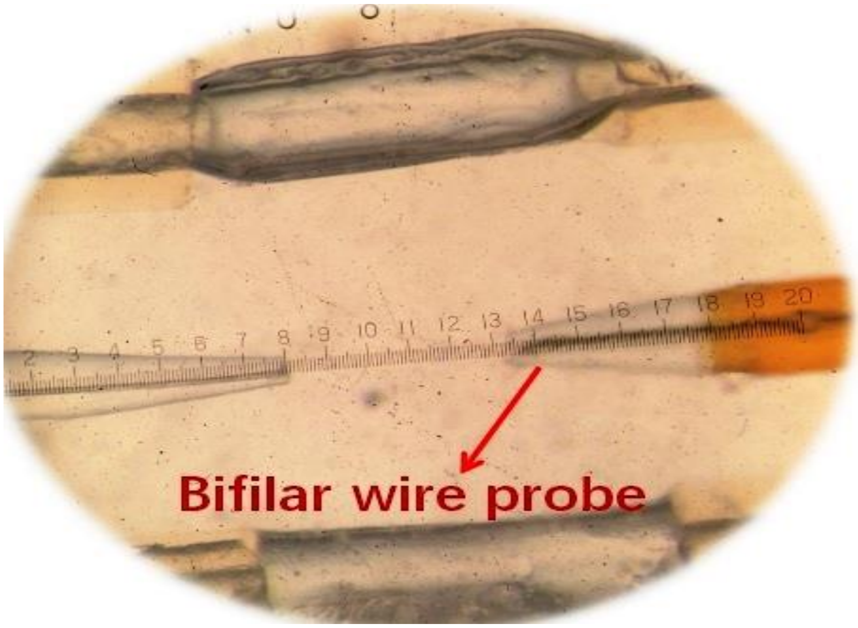

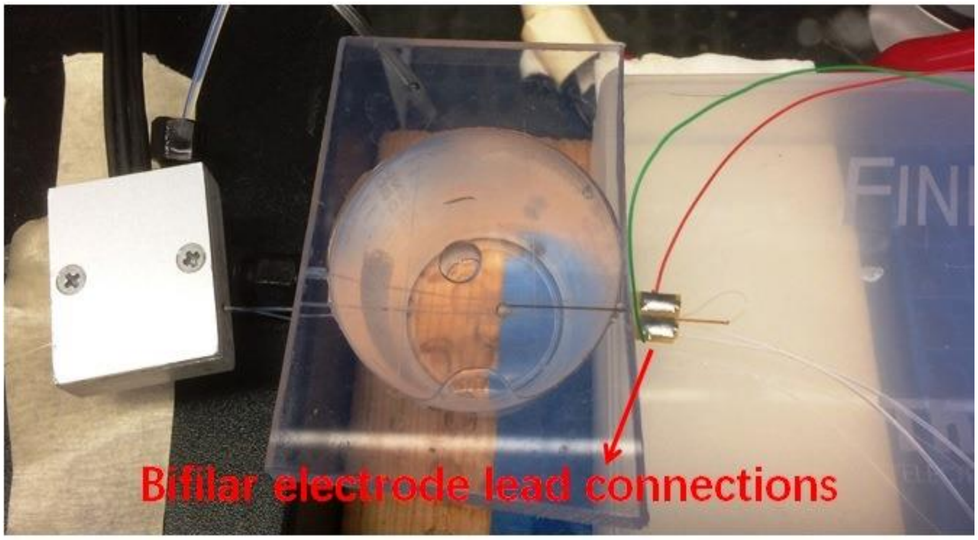

Figure B-S6 Bifilar wire electrode probe (Design D). Top: Shown inserted in suppressor. Bottom: The aluminum admittance detector block is placed before the suppressor, which is immersed in water in the cup. The back end of the probe with the lead wires are outside the cup.

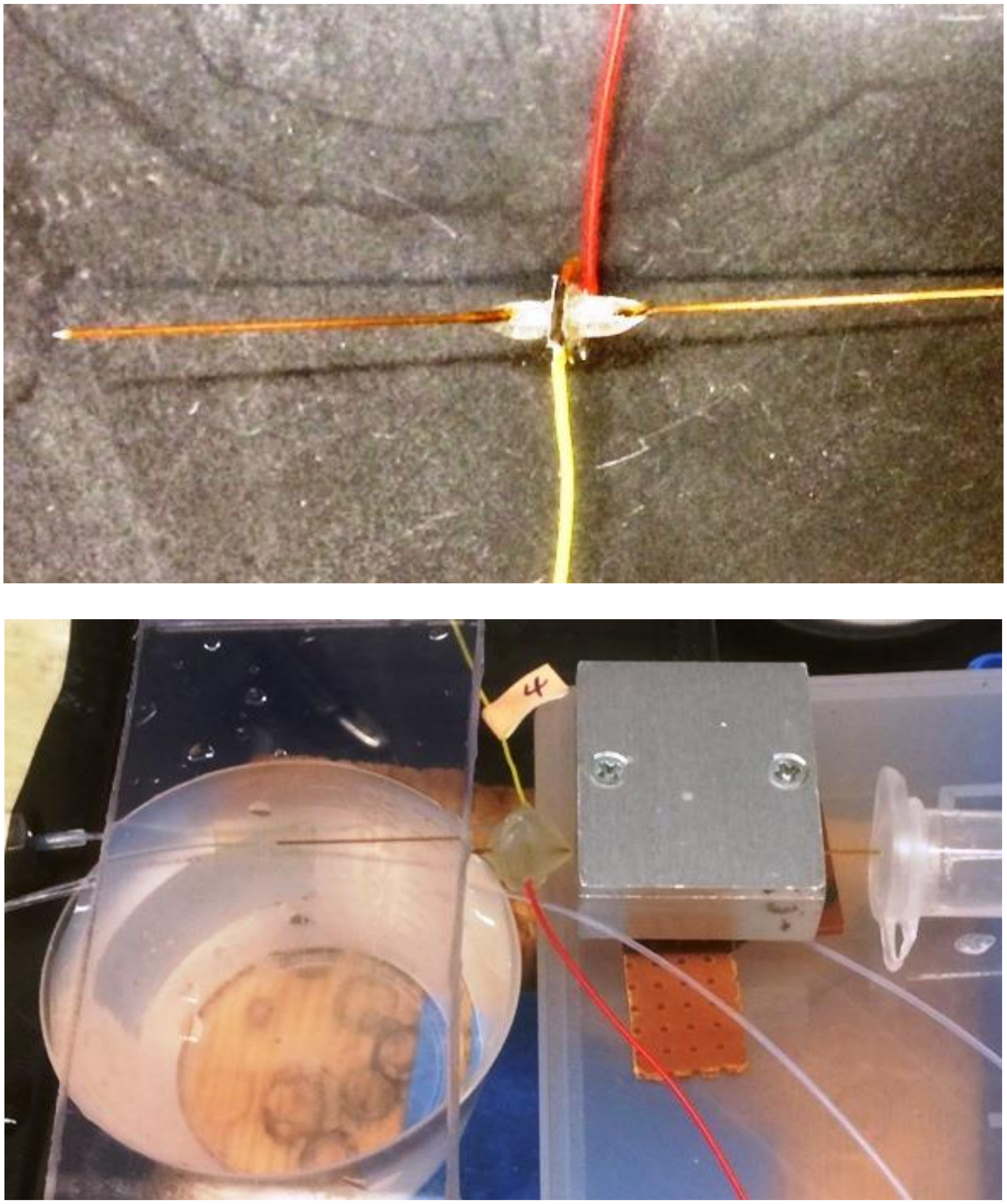

Figure B-S7 Design E: Foil electrode cell. Top: Cell alone, with 20 µm and 25 µm i.d., inlet and exit capillaries. Bottom: Deployment: Column to suppressor to foil electrode detector to TraceDec admittance detector.

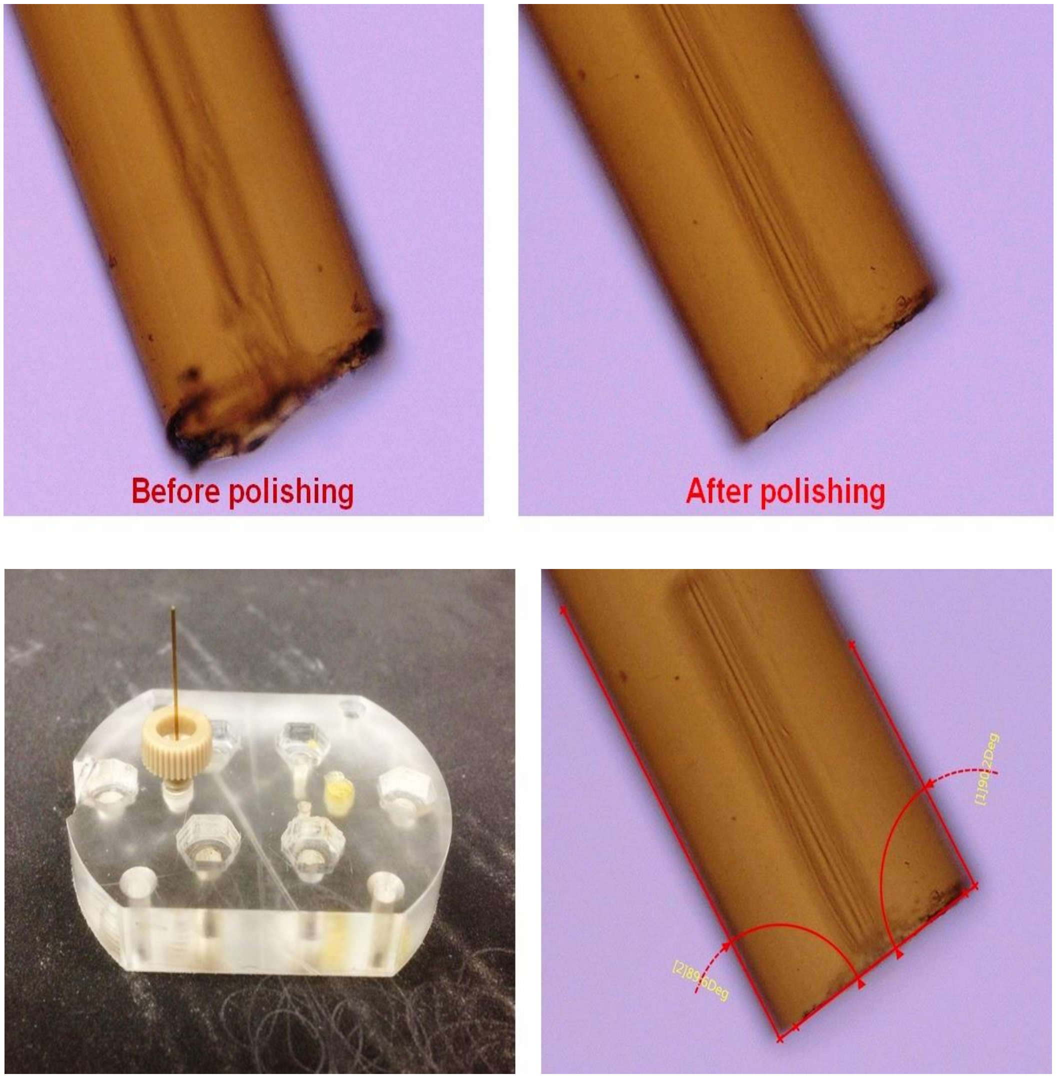

Figure B-S8 Polishing of the silica capillary tip.

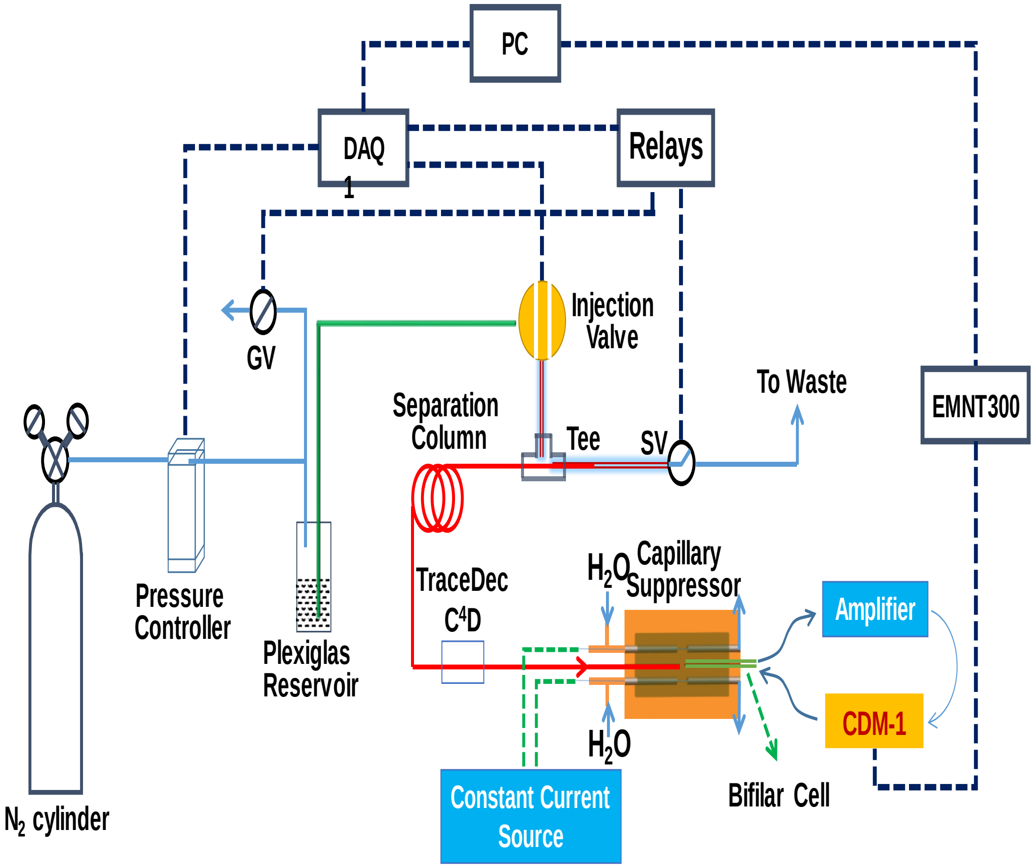

Figure B-S9 System setup for testing the conductometric cells. Here the admittance detection probe is shown positioned before the suppressor and the contact conductivity test cell after the suppressor.

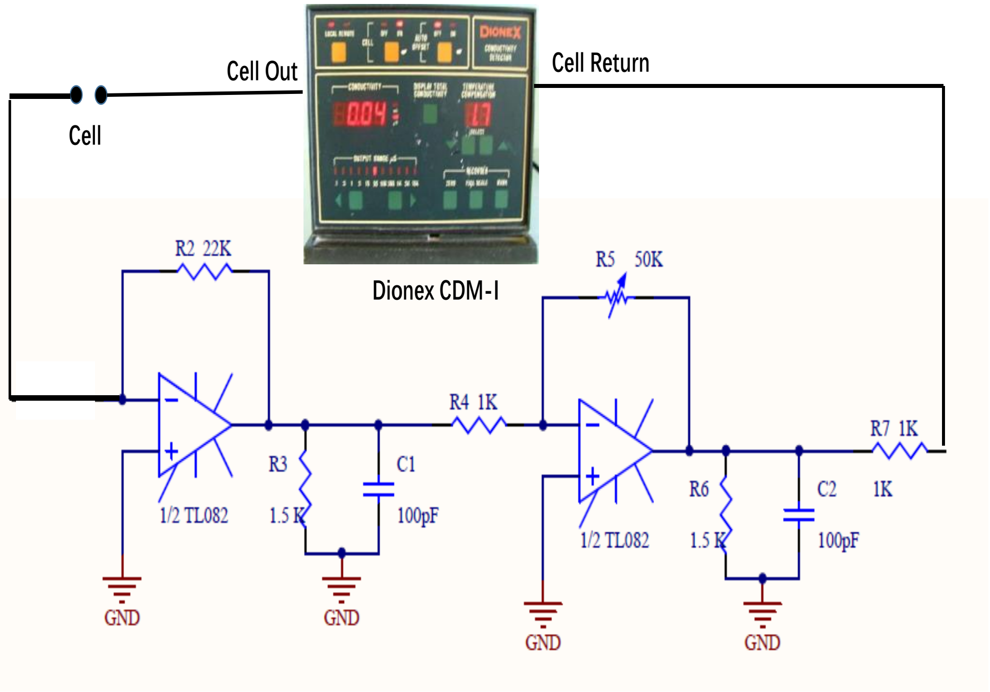

Figure B-S10 Contact conductivity detection cells, detection arrangement with TL082 as preamplifier, amplification range: 20-1000.

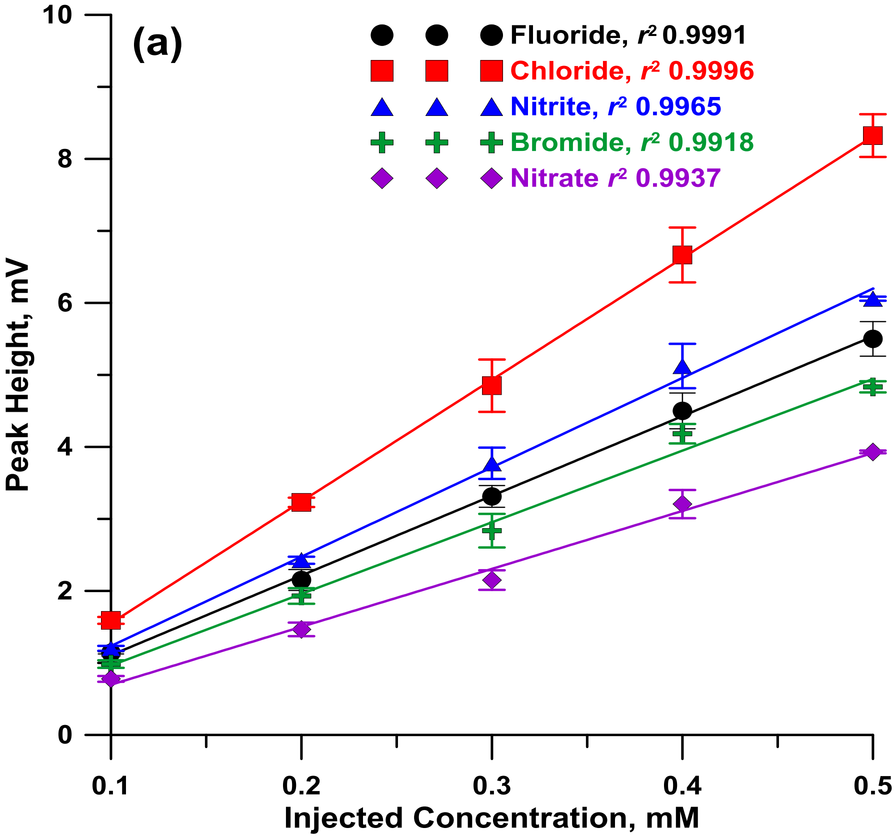

Figure B-S11 (a) Height response to injected concentration. Non-suppressed Detection. TraceDec admittance detector. Column: 19 μm i.d., 370 μm o.d. Cyclic Olefin Polymer, 1007 mm in length; Effective length: 300 mm; CEX capacity before latex AS18 coating: 0.77 peq/mm2; AEX capacity after latex AS18 coating: 24.1 ± 1.8 peq/mm2. Sample: 5 anions (F−, Cl−, NO2−, Br−, NO3−) in a mixture, 0.10, 0.20, 0.30, 0.40, and 0.50 mM in concentration. Eluent: 5.0 mM sodium benzoate (NaBz). Injection time: 1500 ms @15 psi; Injection volume: ~ 0.35 nL; Linear velocity: 0.34 cm/s (45 psi); TraceDec admittance detector: 0 dB attenuation in voltage; gain, 200%; frequency, 150 kHz; offset: 0.

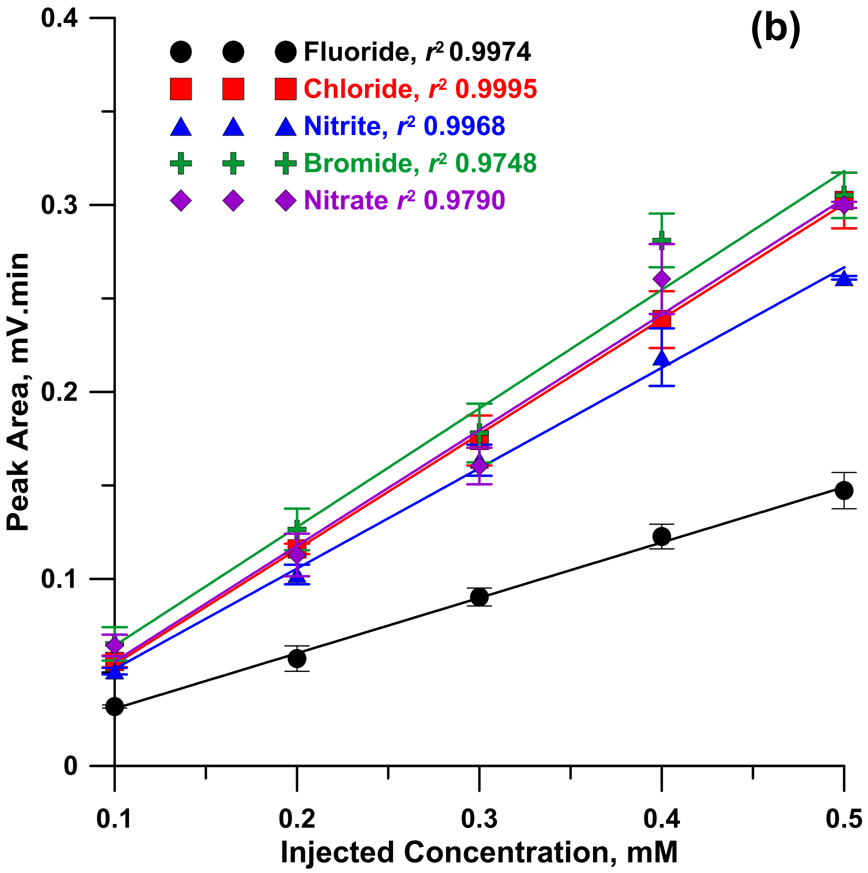

Figure B-S11 (b) Area response to injected concentration. Non-suppressed Detection. TraceDec admittance detector. Column: 19 μm i.d., 370 μm o.d. Cyclic Olefin Polymer, 1007 mm in length; Effective length: 300 mm; CEX capacity before latex AS18 coating: 0.77 peq/mm2; AEX capacity after latex AS18 coating: 24.1 ± 1.8 peq/mm2. Sample: 5 anions (F^-, Cl^-, NO_2^-, Br^-, NO_3^-) in a mixture, 0.10, 0.20, 0.30, 0.40, and 0.50 mM in concentration. Eluent: 5.0 mM sodium benzoate (NaBz). Injection time: 1500 ms @15 psi; Injection volume: ~ 0.35 nL; Linear velocity: 0.34 cm/s (45 psi); TraceDec admittance detector: 0 dB attenuation in voltage; gain, 200%; frequency, 150 kHz; offset: 0.

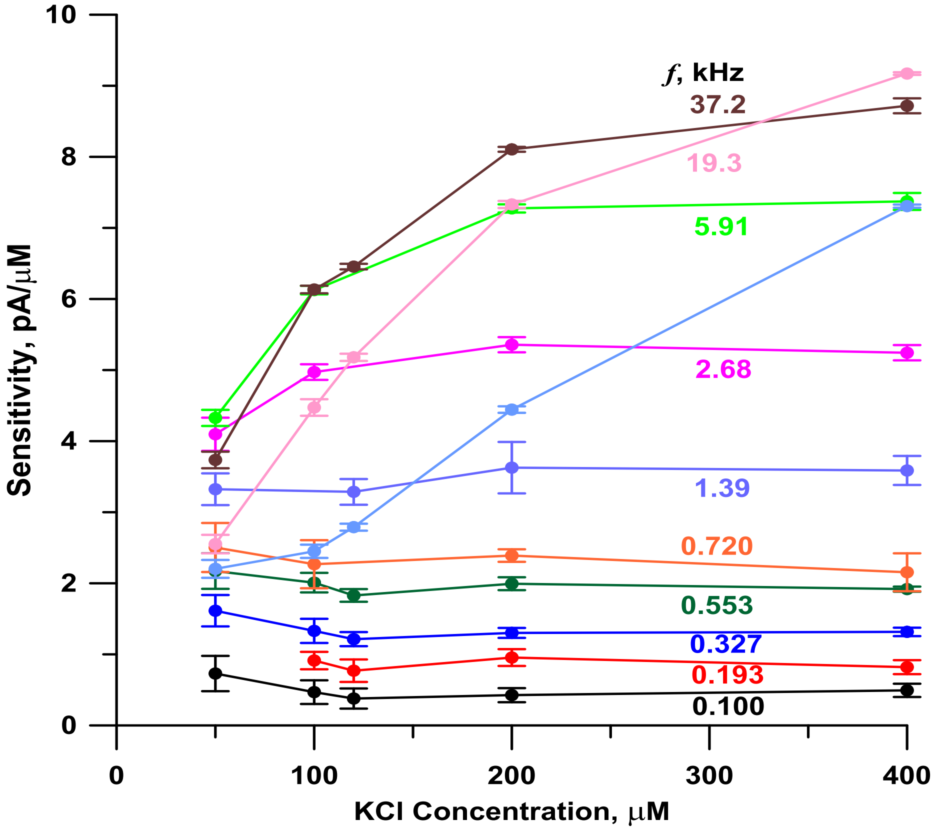

Figure B-S12 Sensitivity plot for low concentrations (0.05 - 0.4 mM) of KCl solution observed with a specific laboratory-made admittance detector. Flow injection response to a blank capillary (i.d.: 15 µm; o.d.: 365 µm). Absolute sensitivity values vary based on applied voltage (data shown are for 27 V p-p sine wave), electrode spacing (here 0.4 mm), etc., but the pattern remains the same. A linear response will be reflected in a flat response curve. Responses below 50 µM KCl are not shown because the results are affected considerably by contamination from atmospheric CO2. Nevertheless, the sensitivity clearly decreases greatly at the higher frequency end with decreasing concentration, essentially becoming zero.

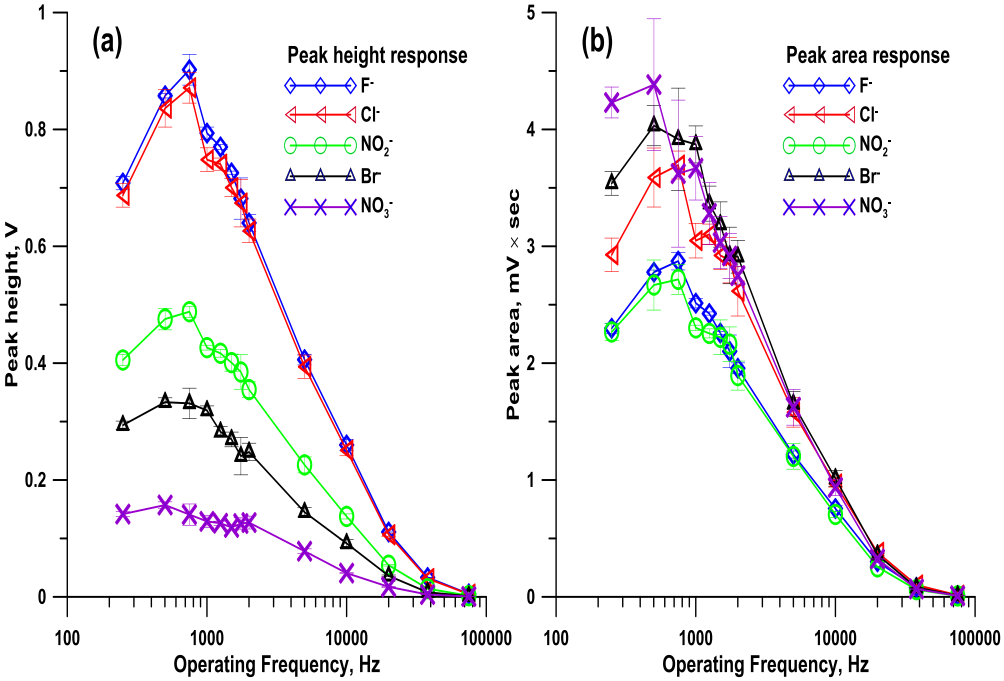

Figure B-S13 Response Bode plots for (a) Height and (b) Area for 0.5 mM concentrations of each anion injected into a suppressed OTIC system (Figure 3 in reference 15). Laboratory-made admittance detector detection probe located 70 mm from suppressor center. AS18 coated sulfonated COP column: 19 μm i.d., 370 μm o.d., 784 mm in length. Exit capillary: silica, 25 μm i.d., 370 μm o.d., ~ 11 cm in length. Eluent: 5.0 mM NaOH. Suppressor active length 0.62 mm, suppressor current 20 μA. 0.8 nL injection, linear velocity: 0.71 cm/s.

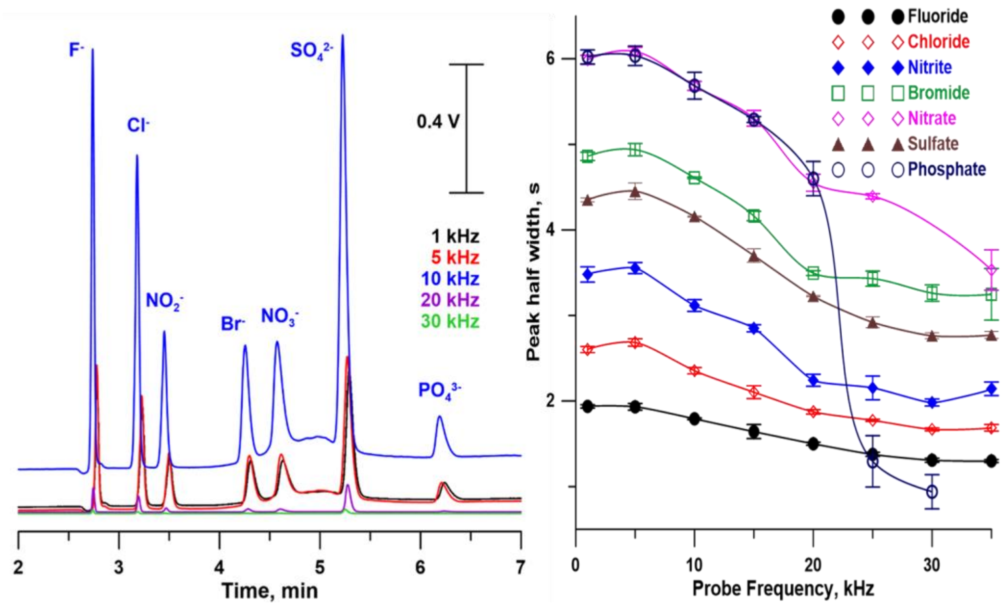

Figure B-S14 Left panel: Response of a laboratory-built admittance detector at various frequencies. Chromatographic conditions: COP column: 28 µm i.d., 370 µm o.d., 744 mm in active length; Detector placed 33 mm after suppressor on exit capillary (silica, 25 µm i.d., 370 µm o.d. Suppressor active length 0.65 mm, flow rate 172 nL/min, Sample: F^-, Cl^-, NO_2^-, Br^-, NO_3^-, SO_4^{2-}, $H_2PO_4^{3-}$, 0.10 mM each in water; injection volume: 6.8 nL; Eluent: LiOH, gradient, 8.0 - 40.0 mM (0 - 3 min); 40 mM (3 - 7 min); 40 - 8 mM (7 - 7.5 min); 8 mM (7.5 - 10 min); Suppression current: 15.0 µA. Right panel: peak half-widths as a function of frequency.

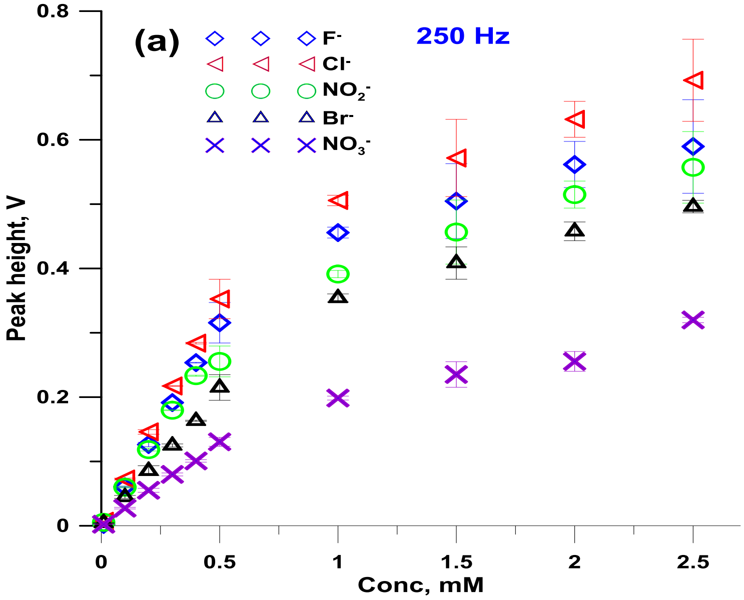

Figure B-S15 (a) Changes in height-based calibration in SOTIC as a function of probe frequency (250 Hz).

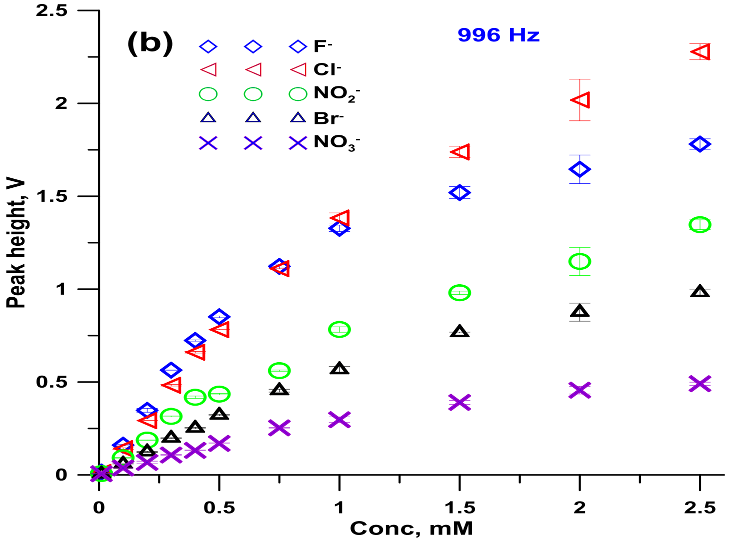

Figure B-S15 (b) Changes in height-based calibration in SOTIC as a function of probe frequency (996 Hz).

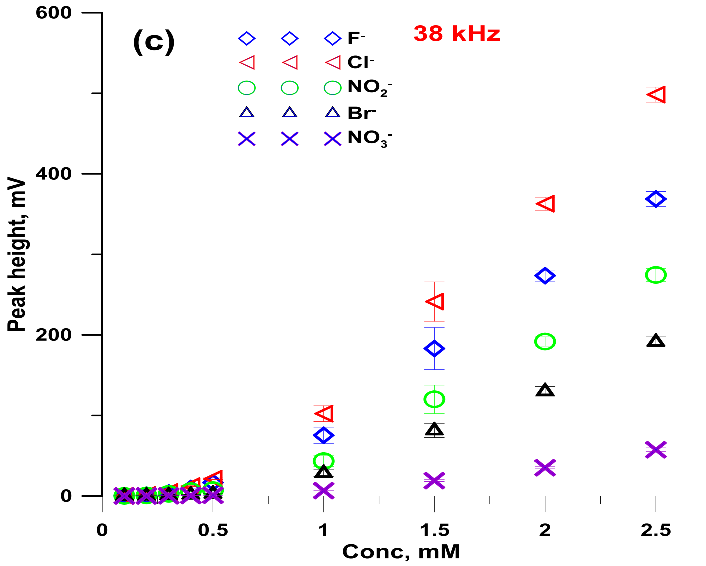

Figure B-S15 (c) Changes in height-based calibration in SOTIC as a function of probe frequency (38 kHz).

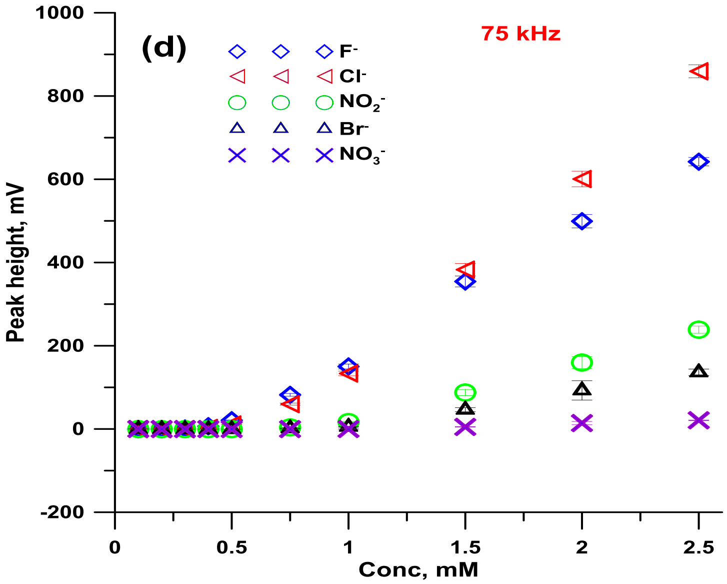

Figure B-S15 (d) Changes in height-based calibration in SOTIC as a function of probe frequency (75 kHz).

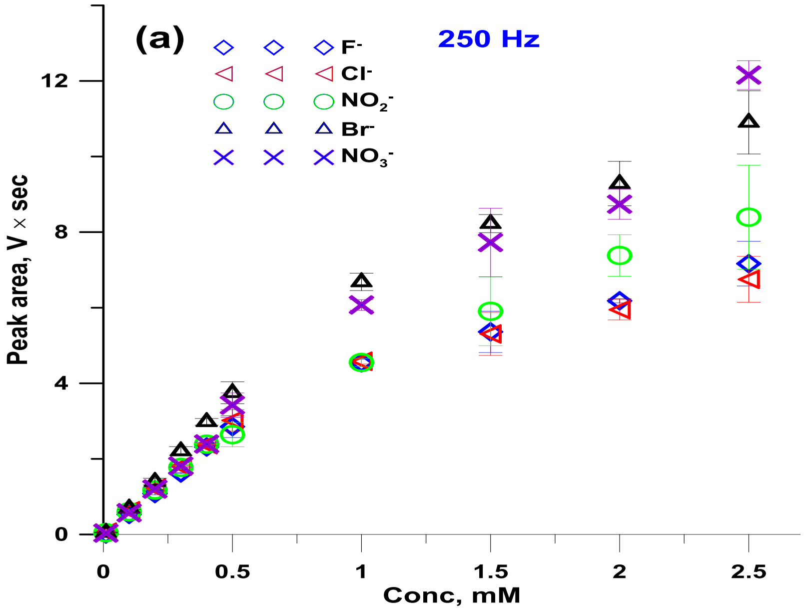

Figure B-S16 (a) Changes in area-based calibration in SOTIC as a function of probe frequency (250 Hz).

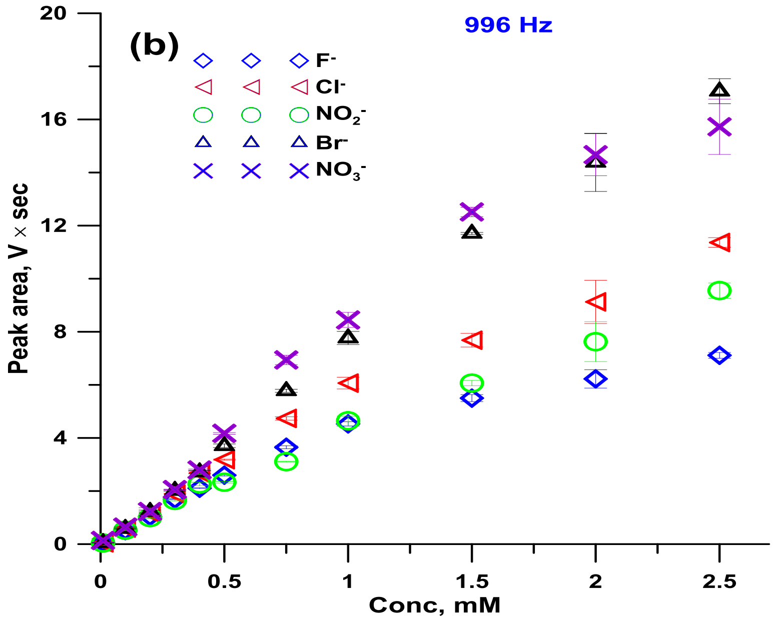

Figure B-S16 (b) Changes in area-based calibration in SOTIC as a function of probe frequency (996 Hz).

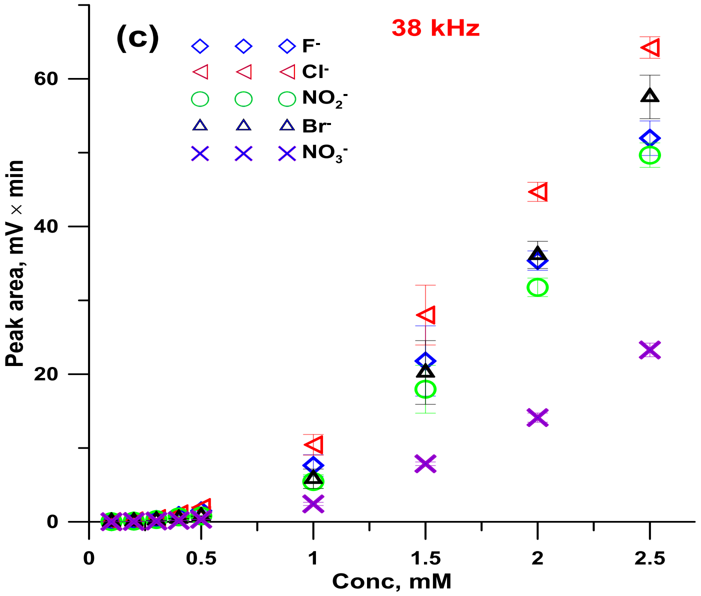

Figure B-S16 (c) Changes in area-based calibration in SOTIC as a function of probe frequency (38 kHz).

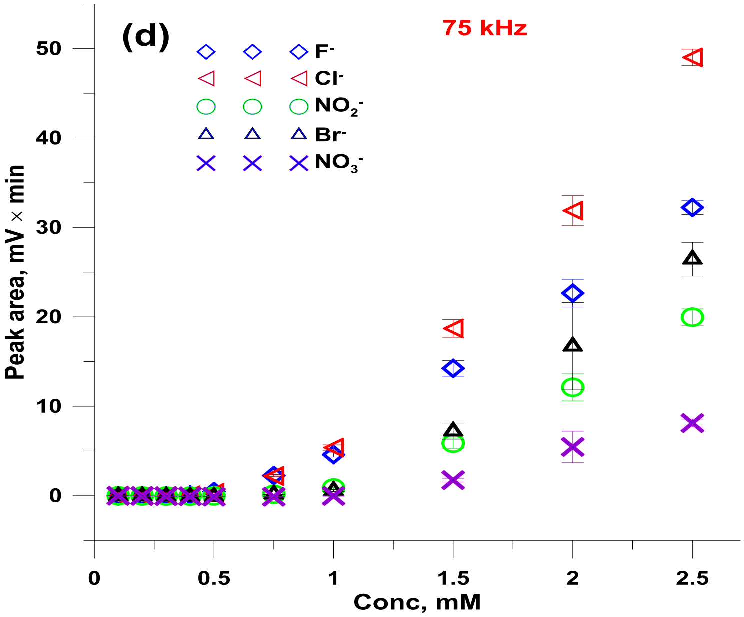

Figure B-S16 (d) Changes in area-based calibration in SOTIC as a function of probe frequency (75 kHz).

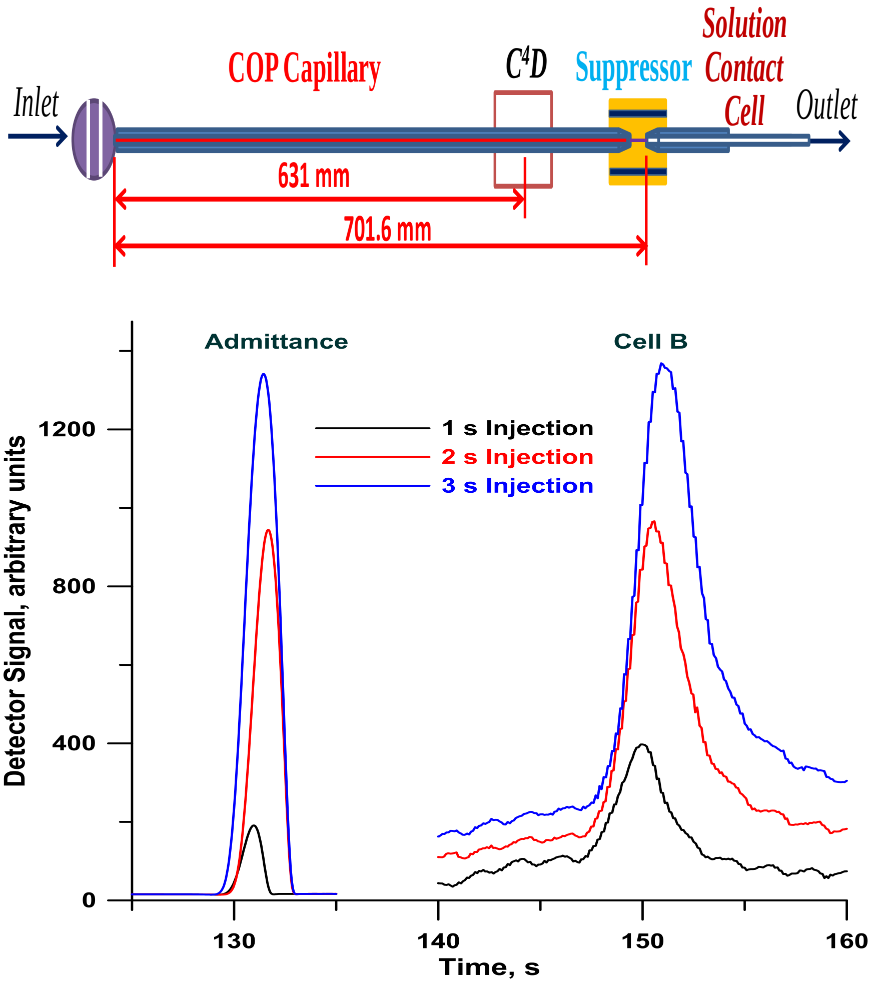

Figure B-S17 Admittance detector vs. Cell B response. Top panel indicates experimental arrangement. Flow Injection mode. Untreated COP capillary, 28 µm i.d., 370 µm o.d., 701 mm long; Suppressor active length 0.55 mm, current 5.0 µA. Effective length: TraceDec, 631 mm; contact conductivity cell, 701.6 mm; TraceDec: voltage, 0 dB; gain, 200%; frequency, 75 kHz; offset: 0; Cell B: Dionex CDM-1, Eluent: DI H2O. Sample: Cl-, 1.0 mM. Running pressure: 35 psi. Injection pressure: 14 psi, hydrodynamic injection, 1, 2, and 3 s.

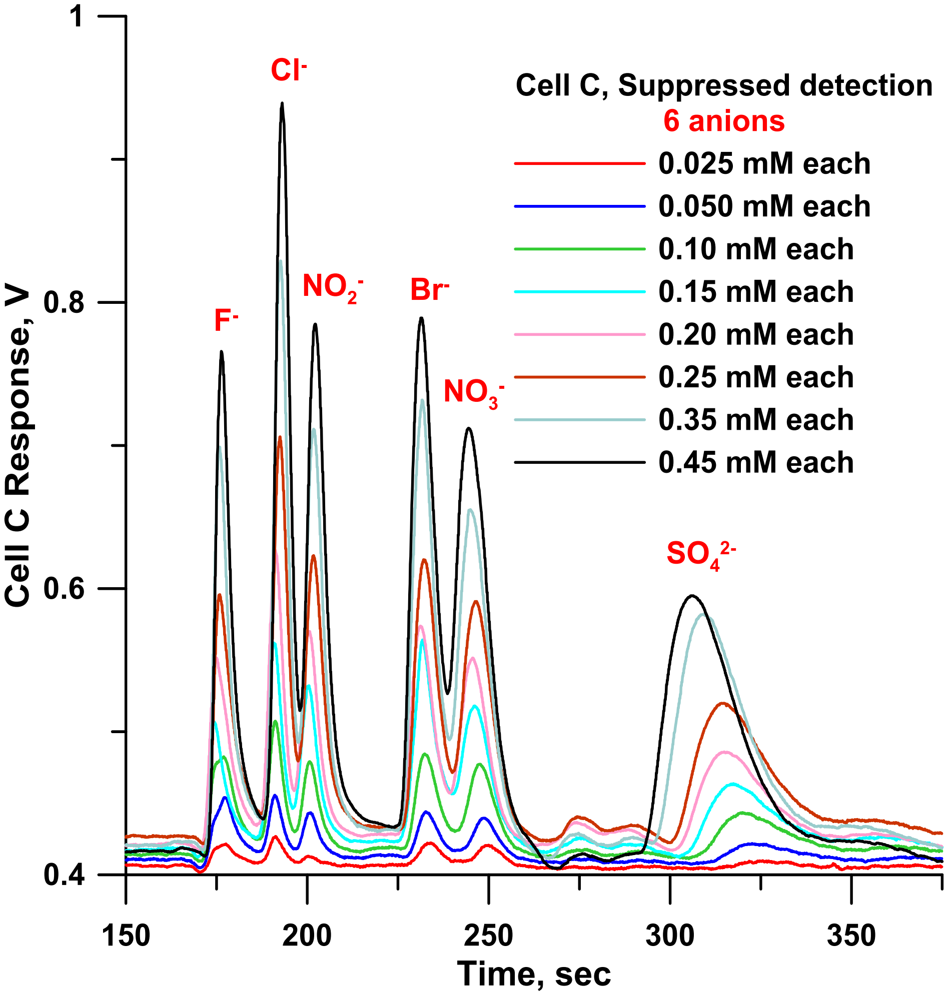

Figure B-S18 Cell C response to 6 anions at concentrations ranging from 25 µM to 450 µM. AS18 coated sulfonated COP column: 28 µm i.d., 370 µm o.d., 906 mm in length. Electronics: Dionex CDM-1, with range set at 30 µS. Amplification: ~ 100-fold by OPA128. Suppressor active length 0.85 mm, voltage 19.1 V. 4.2 nL injection, each analyte 0.45 mM. Running pressure: 40 psi.

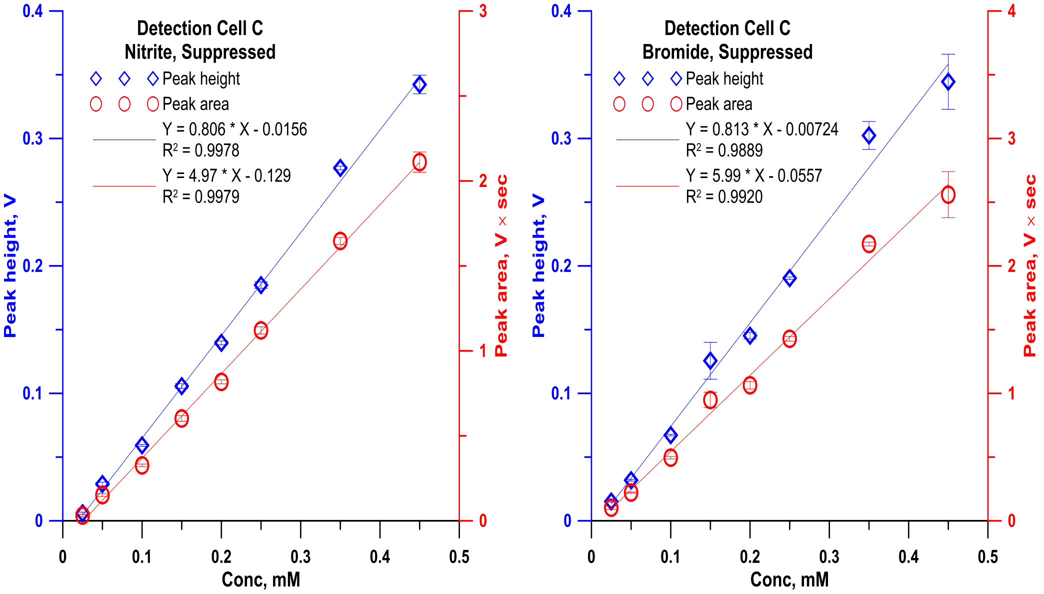

Figure B-S19 Height and area-based calibration data for nitrate and bromide, data taken from Figure BS18.

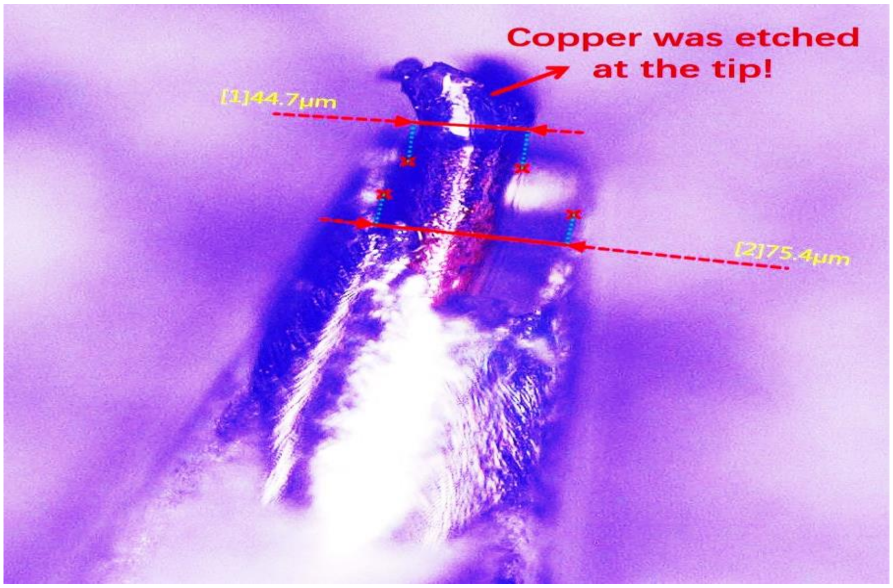

Figure B-S20 In Cell C, Center copper electrode is etched over a period of time, leaving the enamel shell and reducing sensitivity.

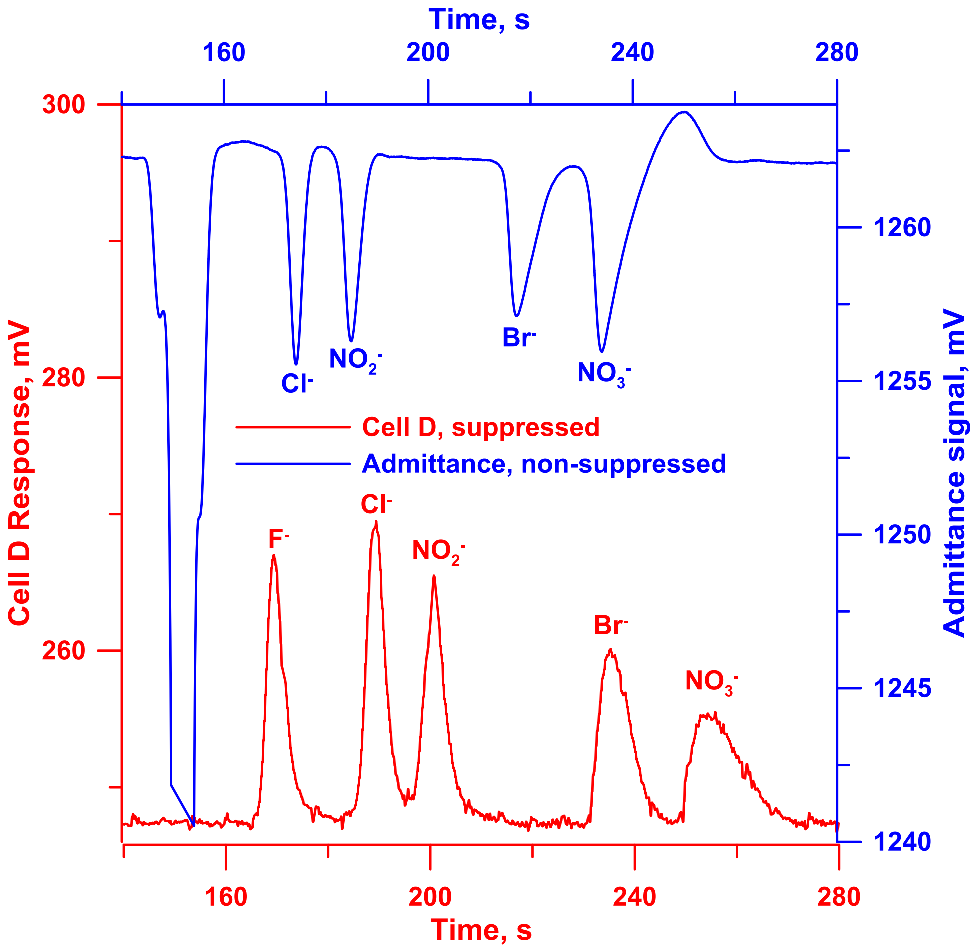

Figure B-S21 Chromatogram comparison between admittance detection and Cell D from the same injection. AS18 coated sulfonated COP column: 28 µm i.d., 370 µm o.d., 906 mm in length. Exit capillary: silica, 75 mm i.d., 360 mm o.d., ~35 mm in length. TraceDec admittance detection: voltage, -24 dB; gain, 200%; frequency, 150 kHz; effective length: 850 mm. Electronics: Dionex CDM-1 10 µS full scale. Preamplification: ~ 200x. Suppressor active length 0.62 mm, current 10 µA. Eluent: ~ 10 mM NaOH. ~ 5 nL injection, each analyte 0.50 mM. Running pressure: 40 psi.

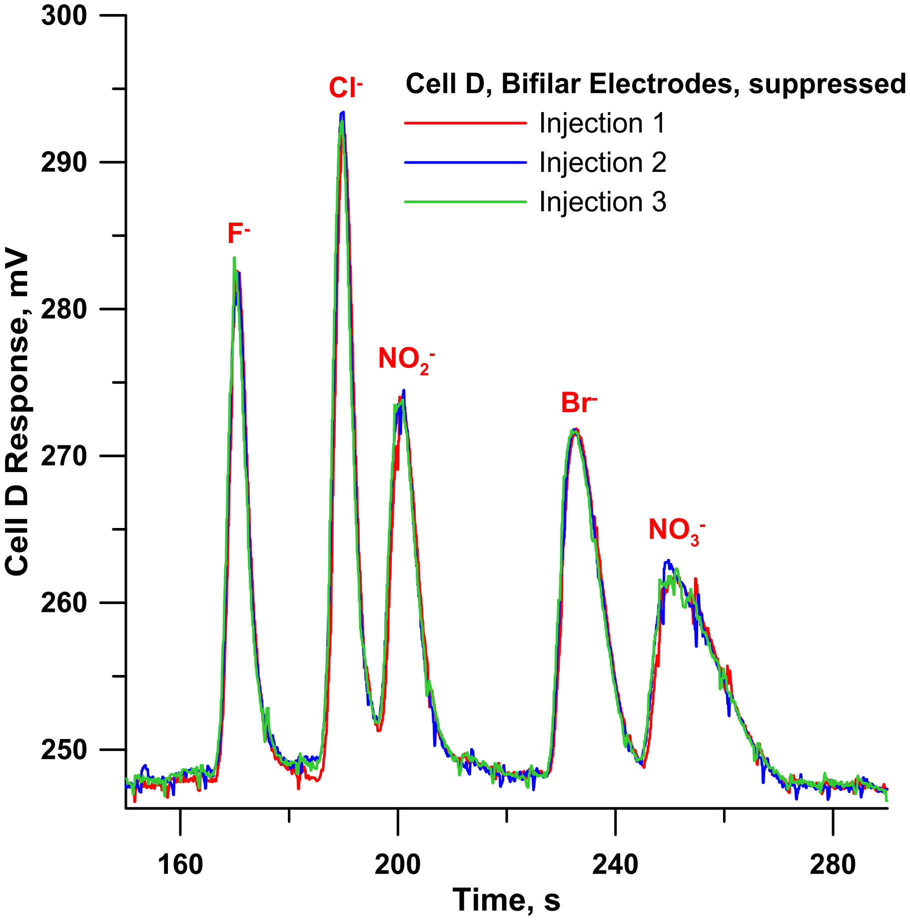

Figure B-S22 Reproducibility of overall system and Cell D. Chromatographic conditions same as Figure S21. Each analyte 1.0 mM.

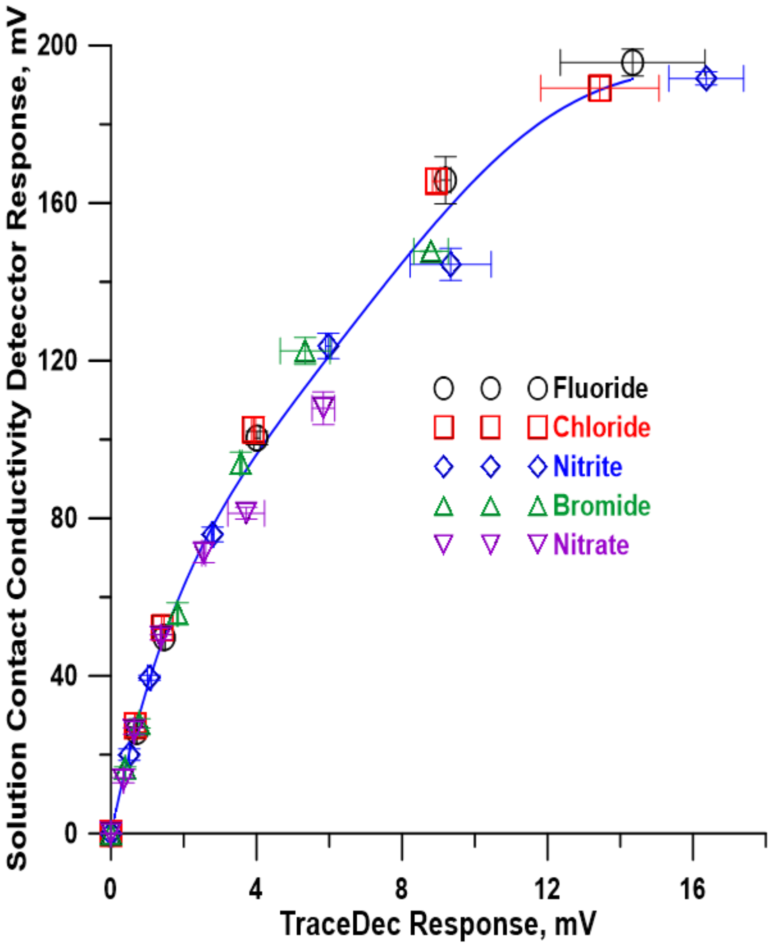

Figure B-S23 Relationship between the serially placed admittance detector response (@ 38 kHz) vs true conductivity response based on peak height of various analytes at various concentrations. The best fit line shown is that from a 5th order polynomial fit.

Appendix C

SUPPORTING INFORMATION FOR CHAPTER 4

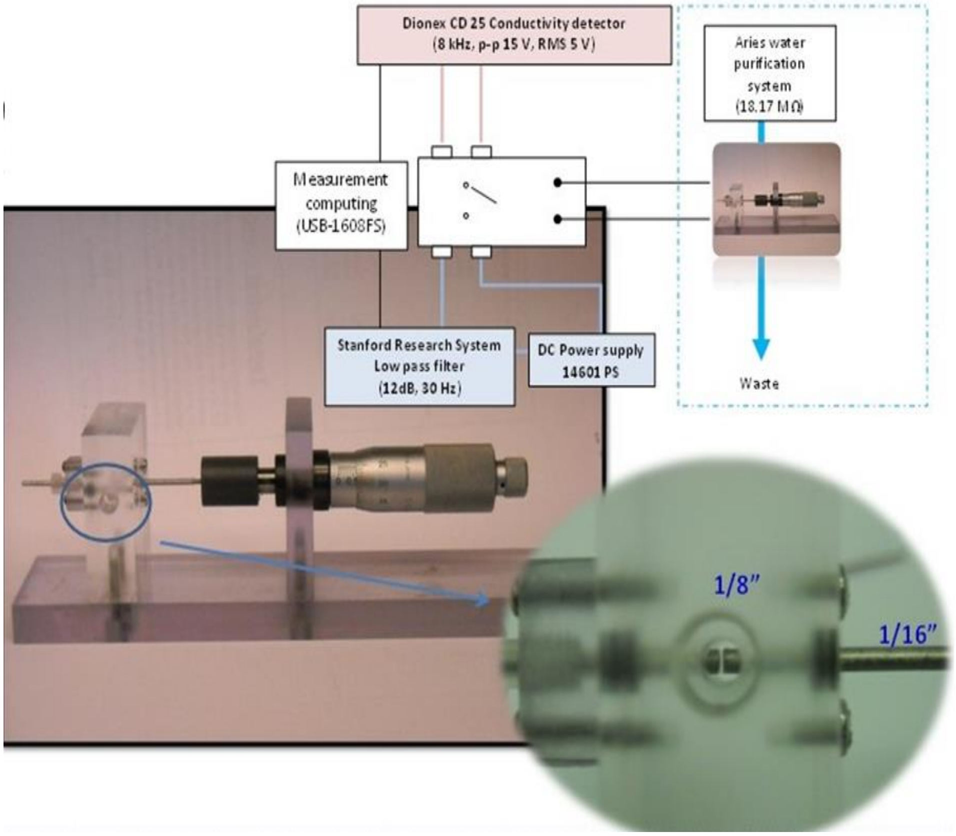

Figure C-S1 Experimental arrangement for determining the effect of the applied field strength photographically shown. Water passes horizontally through the ¼-28 threaded 1/8 in bore flow path at ~ 7 mL/min. While the electrodes are visible when the fittings to the bore are removed, note that the electrodes have transparent thin PTFE sleeves – only the faces are in contact with the fluid. A DPDT switch allows interrogation in the DC or bipolar pulse mode.

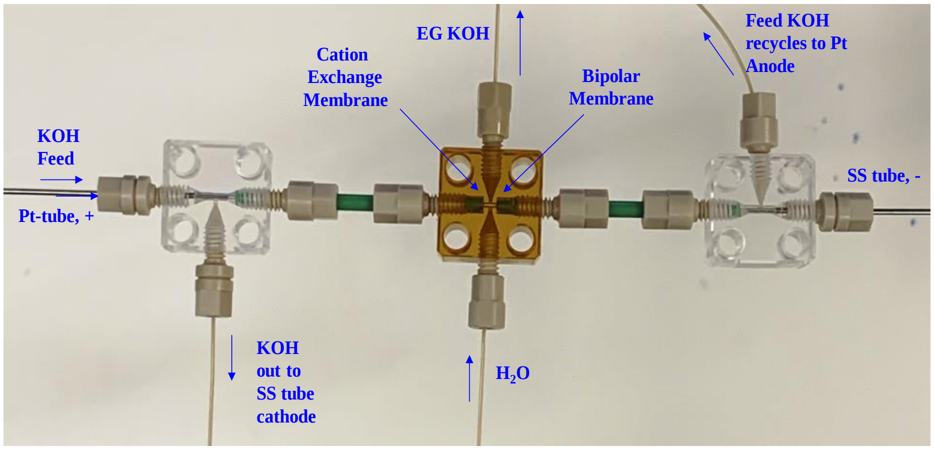

Figure C-S2 Photograph of the Nanovolume EG

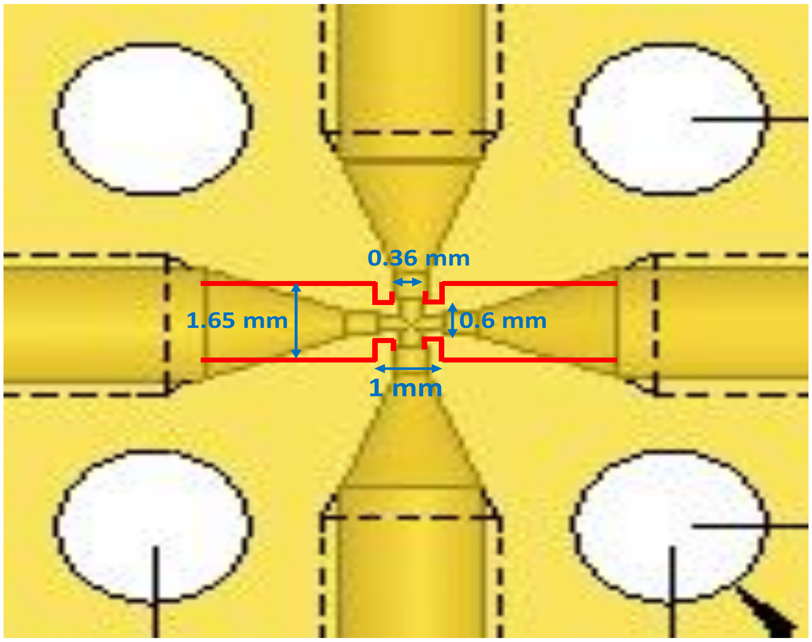

Figure C-S3. The red lines indicate modifications made to the commercial cross.

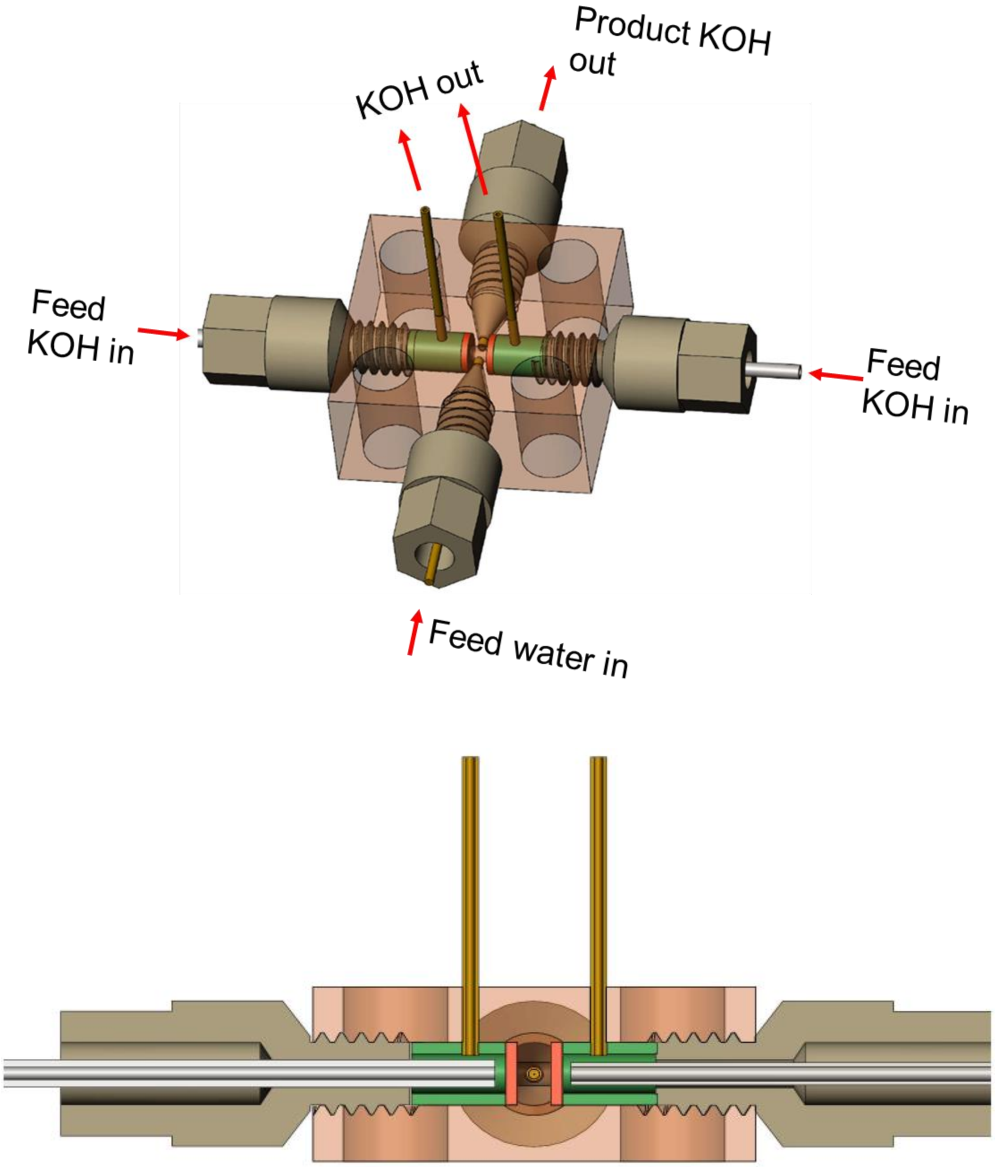

Figure C-S4 The nanovolume EG built on a single cross without the need for further tees. The overall view is shown in the top figure where 360 μm o.d. 150 μm i.d. PEEK tubes access the compartments behind the membranes. The bottom figure shows the cutaway view from the front edge.

Using PSoC 5LP as a Programmable Current Source: The PSoC 5LP programmable system on a chip is a versatile inexpensive ($10) USB-powered device that has many attractive attributes (https://www.cypress.com/documentation/development-kitsboards/cy8ckit-059-psoc-5lp-prototyping-kit-onboard-programmer-and).
It can be directly used as a current source using its digital to analog current (Current DAC) capability but with somewhat limited resolution. The current DAC has 8-bit resolution and permits operation in three ranges: 0-32, 0-255, and 0-2040 μA. The respective (approximate) resolution is 0.125, 1, and 8 μA/bit. It can be set to positive (source) or negative (sink) current. The range can be software programmed in a manner to both have the highest resolution in the low end and still use the full 2.04 mA capability, albeit for the present application, the current needs are not likely to exceed that provided by the lowest range. The main practical limitation that may arise about using the PSoC directly as the current source is its maximum voltage output capability of 5V, especially if the EG inner bore is limited to the original passage diameter of the cross.

Using the PSoC Programmable Voltage Output DAC Through an Operational Amplifier. The PSoC provides multiple 12-bit voltage DACs which can be used as current DACs as used in conjunction with one of the on-board operational amplifiers. The rest of the external circuitry follows an application note from Analog Devices (see Figure 2, Application Note CN-0151, https://www.analog.com/en/design-center/reference-designs/circuits-from-the-lab/cn0151.html). The analog voltage output from the PSoC) goes directly to one of the on-board op-amps with an external pin used for dithering the VDAC output to obtain 12-bit resolution. The op-amp is connected to an N-type MOSFET (BSH103, https://assets.nexperia.com/documents/data-sheet/BSH103.pdf) as shown.

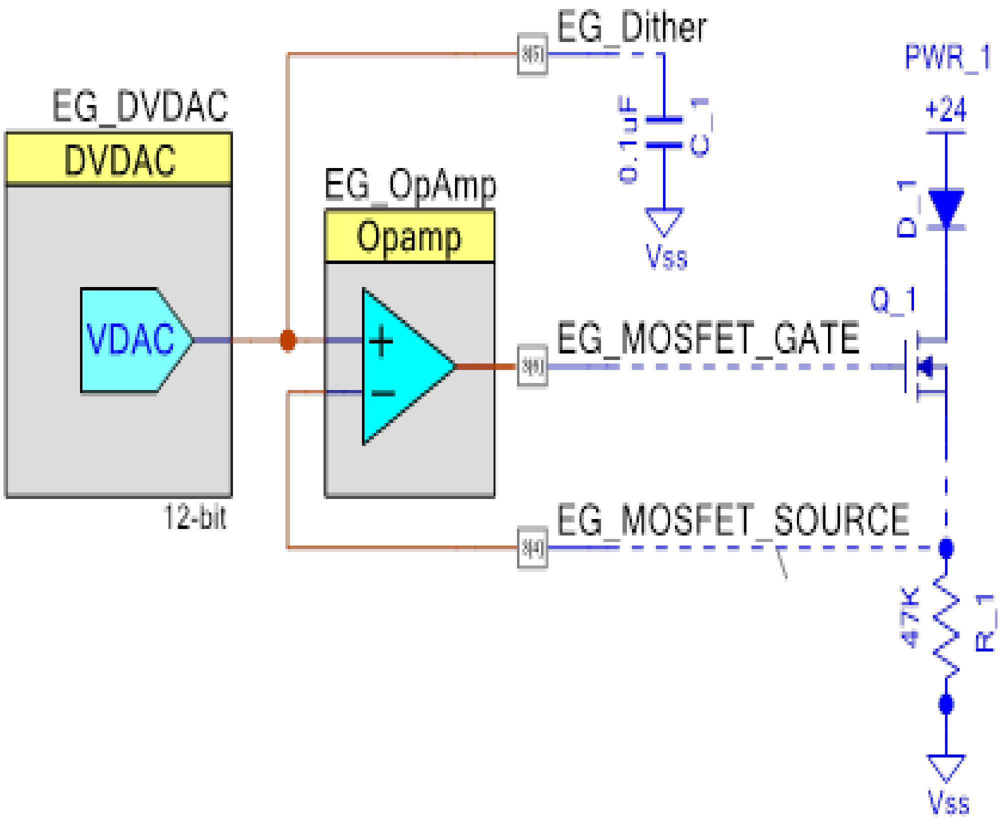

Figure C-S5 Using the 12-bit Voltage DAC on the PSoC 5 LP and the on-board op-amp in conjunction with external MOSFETs to provide a current source capable of applying much higher voltages than the PSoC itself can.

The controlled current is I = V*D/R_1 where V is the analog voltage output and D is the fractional bit setting (actual bit setting/4095). R1, the current range setting resistor in this case is 47,000 ohms. With the maximum analog voltage output being 4.08 V, the maximum current will be 4.08/47000 = 86.8 μA, controllable with 12-bit resolution. In the present application it is preferable to reduce maximum V_{out} to 1.02 V for higher resolution with a current ceiling of 21.7 μA with a step resolution of 5.3 nA.

Specific Conductance Data for KOH. The following data for the KOH specific conductance of KOH at 25 °C was supplied by Dr. Yan Liu, Thermo Fisher Scientific. Any departure from 25 °C in the measurement was corrected using a temperature coefficient of 1.7%/°C. For the specific conductance for 0.1 mM KOH, the tabulated infinite dilution equivalent conductance data for K^+ and OH^- (see ref. 31 in main text) are assumed to be applicable.

Table C-S1 Specific Conductance of KOH

KOH Concentration mM	**Specific Conductance μS/cm @ 25 C[a]**	**Polynomial Prediction μS/cm**
0.1	27.21	29.13
1	271.2	267.9
2	530.2	529.7
3	786.2	788.3
4	1044	1044
10	2536	2536
20	4928	4928
30	7221	7221
50	11560	11560
80	17580	17600

[a]If actual temperature differed from 25 °C, this was corrected assuming a 1.7% /°C temperature dependence of conductance. The best fit (four significant digits limited) 6th order polynomial equation is given as

Specific Conductance (μS/cm) = $2.391 + 267.6\,c - 2.146\,c^2 + 9.648 \times 10^{-2}\,c^3 - 2.838 \times 10^{-3}\,c^4 + 3.964 \times 10^{-5}\,c^5 - 2.027 \times 10^{-7}\,c^6$

where c is the concentration of KOH is in mM. A plot of the data and the polynomial best fit is shown overleaf as Figure S6.

A log (c, mM) vs. log (*specific conductance,* μS/cm) plot has the best fit relationship

log (specific conductance, μS/cm) = 0.9684 * log (c, mM) + 2.425

This much simpler equation fits all the data except that at the lowest and highest concentration with less than 2.5% error and may be acceptable for most purposes. The specific % errors of prediction, from lowest to highest concentration, respectively, are: 5.2, -1.9, -1.8, -1.9, -2.4, -2.4, -1.8, -0.7, 1.7, 5.4%.

Gilliam et al. (main text, ref. 43) provides *calculated* values of KOH specific conductance at various temperatures for 10, 20, 30, 50, and 100 mM KOH (and higher concentrations) based on a literature review of data that are generally *at much higher concentrations*. Throughout the above concentration range, the temperature coefficient for the specific conductance of KOH from their calculated values is in the range of 1.2-1.3%. Values for 10-50 mM are within 5% of the values in Table C-S1.

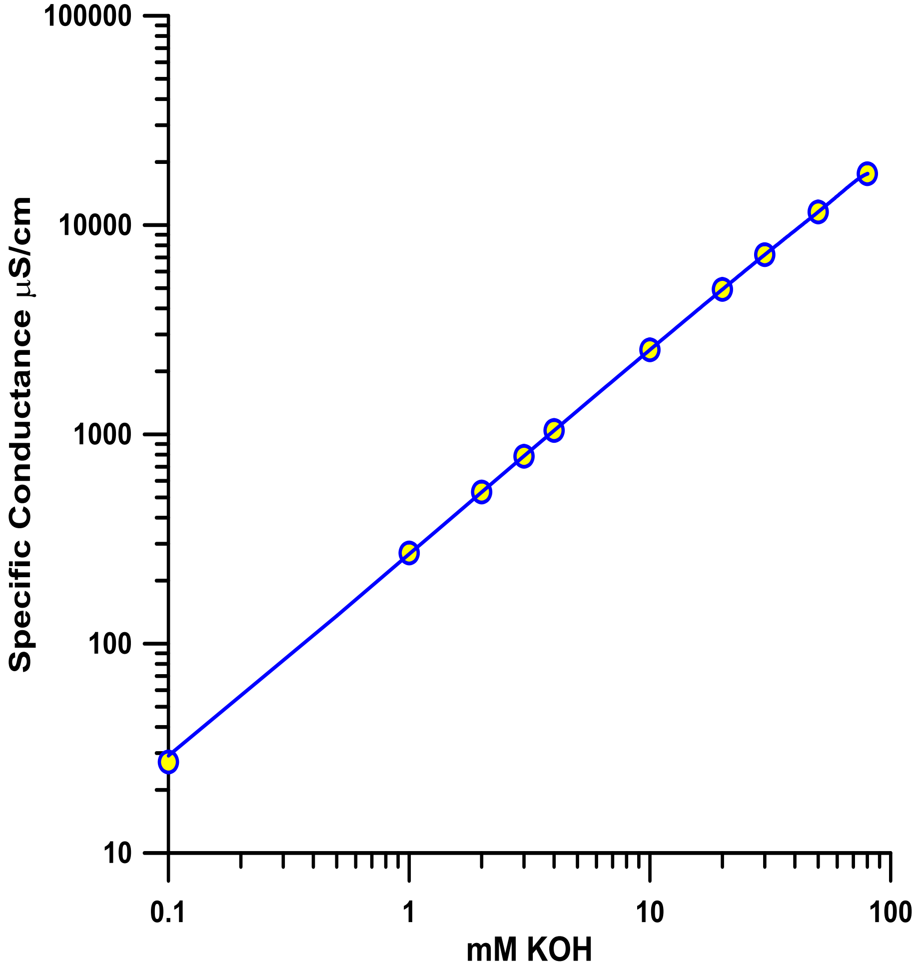

Figure C-S6 The specific conductance of KOH solutions. The blue line is the 6th order polynomial fit for the data in the first two columns in Table C-S1; the values are in col. 3.

Table C-S2 Calculated KOH Specific Conductance (µS/cm)[a]

mM KOH	**20 C**	**25 C**	**30 C**
10	2290	2430	2590
20	4570	4860	5170
30	6840	7280	7740
50	11400	12100	12900
100	22600	24100	25600

[a]From ref. 43

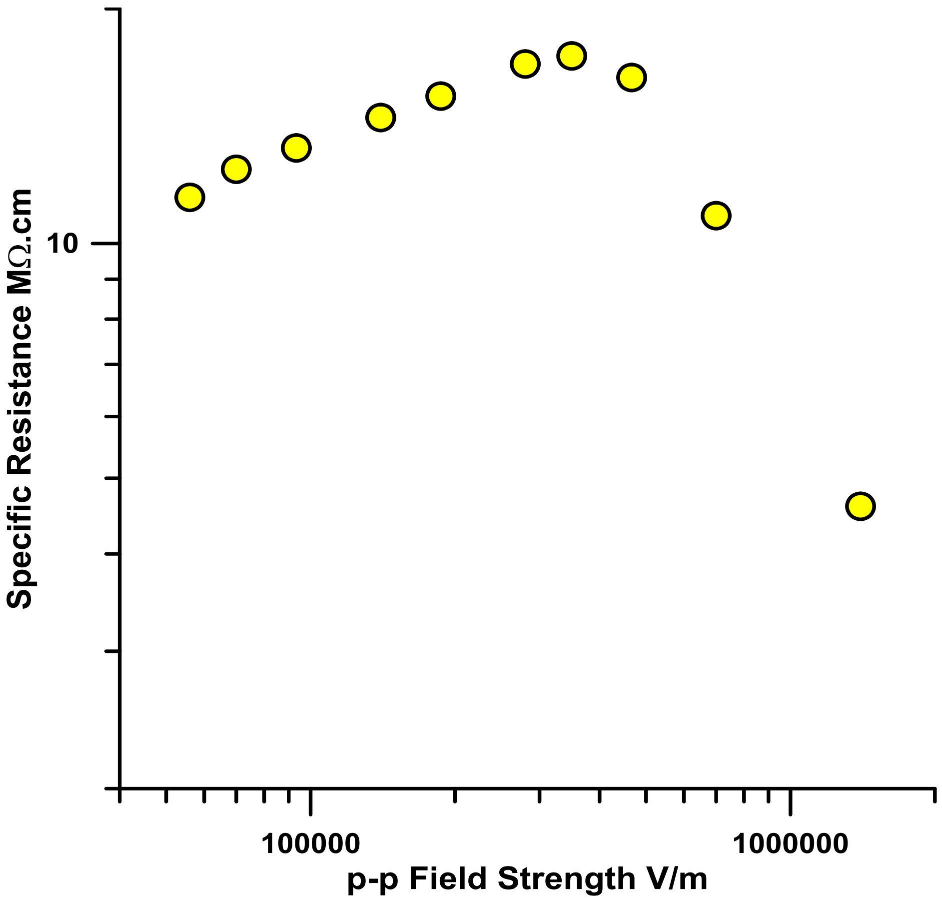

Figure C-S7 Specific resistance of pure water as measured with a Dionex CD25 bipolar pulse conductance detector. The applied voltage was fixed at 28 V p-p; the field strength was varied as the interelectrode distance was changed. There is uncertainty related to absolute accuracy of the electrode distance and the parallelism of the electrode faces but at lower fields the measured resistivity remains within 12-17 MΩ.cm and starts decreasing abruptly at field strengths ≥ 4 x 105 V/m. The difference between DC and AC measurements may lie in the finite time needed for ion atmosphere formation.

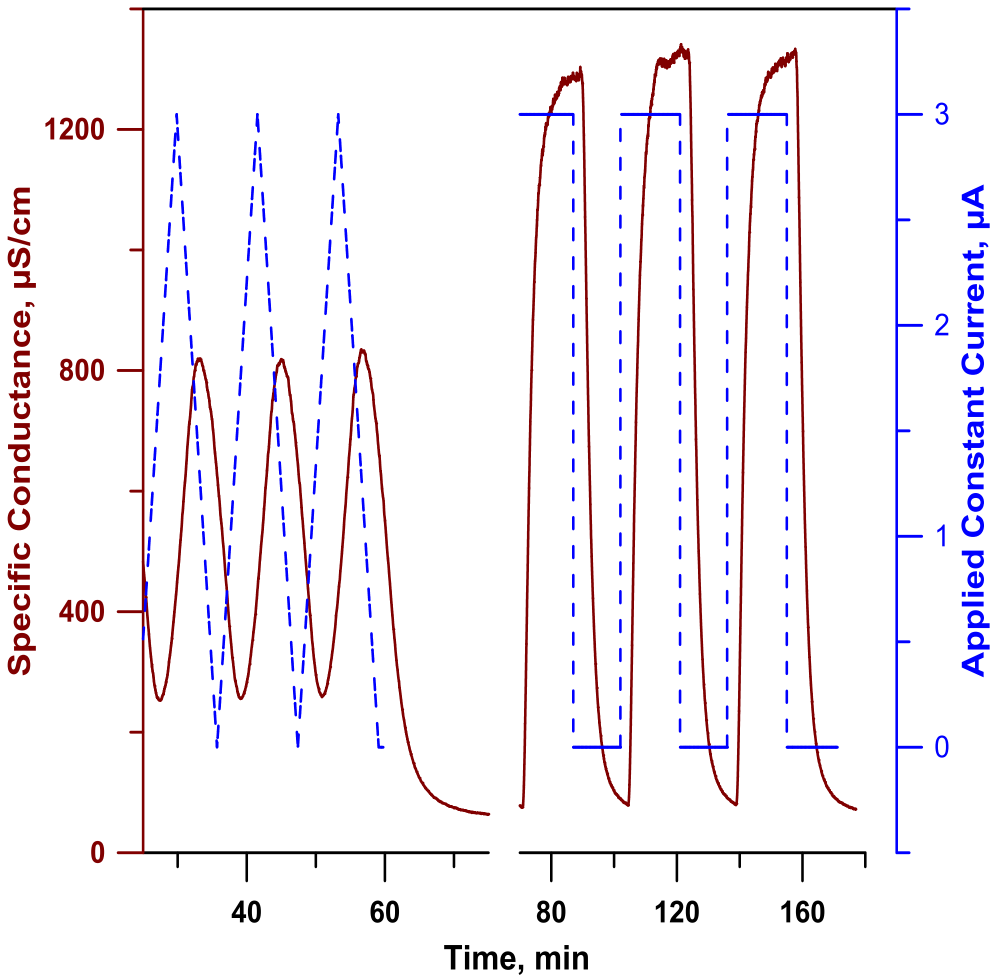

Figure C-S8 Illustrative generator output with triangular wave (flow rate 180 nL/min) and square wave current ramps (flow rate 172 nL/min). The detector was located 30 cm from the EG, essentially mid-column for typical column lengths of 60 cm. Note the phase lag between the applied ramp and observed conductance. Nevertheless, for the most relevant part, the upward ramp in the triangular wave part, the conductance ascent is virtually parallel to the current ascent, the steepness of the slope is not sacrificed.

References

(1) Bialkowski, S. E. *Photothermal Spectroscopy Methods for Chemical Analysis;* Wiley: New York, **1996.**

(2) Whinnery, J. In *Amazing Light*; Chiao, R. Y., Ed.; Springer: New York, **1996**; pp 643−649.

(3) Bell, A. G. *Am. J. Sci.* **1880**, 20 (118), 305−324.

(4) Rosencwaig, A. *Photoacoustics and Photoacoustic Spectroscopy*; Krieger: Malabar, FL, **1980**.

(5) West, G. A.; Barrett, J. J.; Siebert, D. J.; Reddy, K. V*. Rev. Sci. Instrum.* **1983**, 54, 797−817.

(6) Zhong, H.; Duan, T.; Lan, H.; Zhou, M.; Gao, F. *Sensors* **2018**, 18 (7), 2264.

(7) Morris, M. D.; Fotiou, F. K. In *Photothermal Investigations of Solids and Fluids*; Sell, J. A., Ed.; Academic Press: Boston, MA, **1989**; pp 127−154.

(8) Yang, Q. X.; Loock, H. P.; Kozin, I.; Pedersen, D. *Analyst* **2008**, 133, 1567−1572.

(9) Gordon, J. P.; Leite, R. C. C.; Moore, R. S.; Porto, S. P. S.; Whinnery, J. R. *J. Appl. Phys.* **1965**, 36, 3−8.

(10) Snook, R. D.; Lowe, R. D. *Analyst* 1**995**, 120, 2051−2068.

(11) Waldron, K. C.; Dovichi, N. J. *Anal. Chem.* **1992**, 64, 1396− 1399.

(12) Li, F. P.; Kachanov, A. A.; Zare, R. N. *Anal. Chem*. **2007**, 79, 5264−5271.

(13) McLaren, R.; Dovichi, N. J. *Anal. Chem*. **1988**, 60, 730−733.

(14) Johnston, S. E.; Fadgen, K. E.; Jorgenson, J. W. *Anal. Chem.* **2006**, 78, 5309−5315.

(15) Dennis, P. J.; Welch, E. F.; Alarie, J. P.; Ramsey, J. M.; Jorgenson, J. W. *Anal. Chem.* **2010**, 82, 4063−4071.

(16) Chun, H. G.; Dennis, P. J.; Welch, E. R. F.; Alarie, J. P.; Jorgenson, J. W.; Ramsey, J. M. *J. Chromatogr. A* **2017**, 1523, 140 − 147.

(17) Brilmyer, G. H.; Fujishima, A.; Santhanam, K. S. V.; Bard, A. J. *Anal. Chem.* **1977**, 49, 2057 −2062.

(18) Fujishima, A.; Masuda, H.; Honda, K.; Bard, A. J. *Anal. Chem*. **1980**, 52, 682 −685.

(19) Brilmyer, G. H.; Bard, A. J. *Anal. Chem*. **1980**, 52, 685 −691.

(20) Pyo, D.; Dascupta, P. K.; Yencoyan, L. S. *Anal. Sci*. **1997,** 13 (Suppl), 185 −190.

(21) Jorgenson, J. W.; Guthrie, E. J. *J. Chromatogr. A* **1983**, 255, 335 −348.

(22) Huang, W.; Chouhan, B.; Dasgupta, P. K. *Anal. Chem*. **2018**, 90, 14561 −14568.

(23) Franko, M.; Liu, M.; Boskin, A.; Delneri, A.; Proskurnin, M. A. *Anal. Sci*. **2016,** 32, 23 −30.

(24) Cassano, C. L.; Mawatari, K.; Kitamori, T.; Fan, Z. H. *Electrophoresis* **2014**, 35, 2279 −2291.

(25) Tran, C. D.; Franko, M. In *Encyclopedia of Analytical Chemistry*; Meyers, R. A., Ed.; Wiley: New York**, 2010**; pp 1 −32.

(26) Waiz, S.; Cedillo, B. M.; Jambunathan, S.; Hohnholt, S. G.; Dasgupta, P. K.; Wolcott, D. K. *Anal. Chim. Acta* **2001**, 428, 163 −171.

(27) Gelb, G. H.; Marcus, B. D.; Dropkin, D. *Rev. Sci. Instrum*. **1964,** 35, 80 −81.

(28) Bennett, G. L.; Lombardo, J. J.; Hemler, R. J.; Silverman, G.; Whitmore, C. W.; Amos, W. R.; Johnson, E. W.; Schock, A.; Zocher, R. W.; Keenan, T. K.; Hagan, J. C.; Englehart, R. W. Mission of Daring: The General-Purpose Heat Source Radioisotope Thermoelectric Generator. In *Proceedings, 4th International Energy Conversion Engineering Conference and Exhibit (IECEC)*, San Diego, CA, June 26 − 29, **2006**; AIAA 2006-4096, https://fas.org/nuke/space/gphs.pdf. See also

https://electronics.stackexchange.com/questions/64718/ current-produced-by-thermocouples.

(29) Herraez, J. V.; Belda, R.´ *J. Solution Chem*. **2006**, 35, 1315 −1328.

(30) Beadie, G.; Brindza, M.; Flynn, R. A.; Rosenberg, A.; Shirk, J. S. *Appl. Opt*. **2015**, 54, F139 −F143.

(31) https://thermtest.com/thermal-resources/rule-of-mixtures.

(32) Würth, C.; Gonzalez, M. G.; Niessner, R.; Panne, U.; Haisch,´ C.; Genger, U. R. *Talanta* **2012**, 90, 30 −37.

(33) Mardelli, M.; Olmsted, J., III *J. Photochem*. **1977**, 7, 277 −285.

(34) Fischer, M.; Georges, J. *Chem. Phys. Lett*. **1996,** 260, 115 −118.

(35) Avena, M. J.; Valenti, L. E.; Pfaffen, V.; De Pauli, C. P. *Clays Clay Miner*. **2001**, 49, 168 −173.

(36) Redmond, R. W.; Gamlin, J. N. *Photochem. Photobiol.* **1999**, 70, 391 −475.

(37) Tafulo, P. A. R.; Queiros, R. B.; Gonza´ lez-Aguilar, G.´ *Spectrochim. Acta, Part A* **2009**, 73, 295 −300.

(38) Spencer, W.; Sutter, J. R. *J. Phys. Chem.* **1979**, 83, 1573 −1576.

(39) Liska, M.; Bartosˇ, L.; Valaˇs´ek, J. *Chem. Papers* **1989** , 43, 303 − 313.

(40) Patil, K.; Pawar, R.; Talap, P. *Phys. Chem. Chem. Phys.* **2000**, 2, 4313 −4317.

(41) Ghasemi, J. B.; Miladi, M. *J. Chin. Chem. Soc*. **2009**, 56, 459 − 468.

(42) Yazdani, O.; Irandoust, M.; Ghasemi, J. B.; Hooshmand, Sh. *Dyes Pigm*. **2012,** 92, 1031 −1041.

(43) Florence, Ng; Naorem, H. *J. Mol. Liq*. **2014**, 198, 255 −258.

(44) Macka, M.; Piasecki, T.; Dasgupta, P. K. *Annu. Rev. Anal. Chem*. **2014**, 7, 183 −207.

(45) https://www.energetiq.com/ldls-laser-driven-light-source-duv-broadband.php

(46) Stock, J. T. *Anal. Chem*. **1984,** 56, 561A−570A.

(47) Small, H. *J. Chromatogr*. **1991**, 546, 3−15.

(48) Gjerde, D. T.; Fritz, J. S.; Schmuckler, G. *J. Chromatogr. A* **1979**, 186, 509−519.

(49) Qi, D.; Okada, T.; Dasgupta, P. K. *Anal. Chem.* **1989**, 61, 1383− 1387.

(50) Johnson, D. E.; Enke, C. G. *Anal. Chem*. **1970**, 42, 329−335.

(51) Huang, W.; Chen, H.; Su, Y.; Hu, R. *Talanta* **2010**, 82, 1364− 1370.

(52) *Chemistry*; Marcel Dekker: New York, **1984**.

(53) Braunstein, J.; Robbing, G. D. *J. Chem. Educ*. **1971**, 48, 52−59.

(54) Zemann, A. J.; Schnell, E.; Volgger, D.; Bonn, G. K. *Anal. Chem*. **1998**, 70, 563−567.

(55) Fracassi da Silva, J. A.; do Lago, C. L. *Anal. Chem*. **1998**, 70, 4339−4343.

(56) Stamos, B. N.; Dasgupta, P. K.; Ohira, S.-I. *Anal. Chem*. **2017**, 89, 7203−7209.

(57) Zhang, M.; Stamos, B. N.; Amornthammarong, N.; Dasgupta, P. K. *Anal. Chem*. **2014**, 86, 11538−11546.

(58) Zhang, M.; Stamos, B. N.; Dasgupta, P. K. *Anal. Chem*. **2014**, 86, 11547−11553.

(59) Nortemann, K.; Hilland, J.; Kaatze, U. *J. Phys. Chem. A* **1997**, 101, 6864−6869.

(60) Huang, W.; Dasgupta, P. K. *Anal. Chem*. **2016**, 88, 12021− 12027.

(61) Huang, W.; Seetasang, S.; Azizi, M.; Dasgupta, P. K. *Anal. Chem*. **2016**, 88, 12013−12020.

(62) Anderson, J. E. *J. Non-Cryst. Solids* **1994**, 172-174, 1190−1194.

(63) Huang, X.; Pang, T. K. J.; Gordon, M. J.; Zare, R. N. *Anal. Chem*. **1987**, 59, 2747−2749.

(64) Huang, X.; Zare, R. N. *Anal. Chem*. **1991**, 63, 2193−2196.

(65) Zhao, H.; Dadoo, R.; Reay, R. J.; Kovacs, G. T. A.; Zare, R. N. *J. Chromatogr. A* **1998**, 813, 205−208.

(66) Dasgupta, P. K.; Bao, L.-Y. *Anal. Chem*. **1993**, 65, 1003−1011.

(67) Kar, S.; Dasgupta, P. K.; Liu, H.; Hwang, H. *Anal. Chem*. **1994**, 66, 2537−2543.

(68) Haber, C.; Jones, W. R.; Soglia, J.; Surve, M. A.; McGlynn, M.; Caplan, A.; Reineck, J. R.; Krstanovic, C. *J. Capillary Electrophoresis* **1996**, 3, 1−12.

(69) Adams, A. A.; Okagbare, P. I.; Feng, J.; Hupert, M. L.; Patterson, D.; Göttert, J.; McCarley, R. L.; Nikitopoulos, D.; Murphy, M. C.; Soper, S. A. *J. Am. Chem. Soc*. **2008**, 130, 8633−8641.

(70) Dasgupta, P. K.; Chen, Y.; Serrano, C. A.; Guiochon, G.; Liu, H.; Fairchild, J. N.; Shalliker, R. A. *Anal. Chem*. **2010**, 82, 10143− 10150

(71) Wahab, M. F.; Gritti, F.; O'Haver, T. C.; Hellinghausen, G.; Armstrong, D. W. *Chromatographia* **2018**, DOI: 10.1007/s10337-018- 3607-0.

(72) Wuersig, A.; Kubań ̌, P.; Khaloo, S. S.; Hauser, P. C*. Analyst* **2006**, 131, 944−949.

(73) Wahab, M. F.; Dasgupta, P. K.; Kadjo, A. F.; Armstrong, D. W*. Anal. Chim. Acta* **2016**, 907, 31−44.

(74) Qi, D.; Okada, T.; Dasgupta, P. K. *Anal. Chem*. **1989**, 61, 1383−1387.

(75) Ryvolova, M.; Preisler, J.; Foret, F.; Hauser, P. C.; Krasensky, P.; Paull, B.; Macka, M. *Anal. Chem*. **2010**, 82, 129−135.

(76) Strong, D. L.; Dasgupta, P. K.; Friedman, K.; Stillian, J. R. *Anal. Chem*. **1991**, 63, 480−486.

(77) Strong, D. L.; Ung Joung, C.; Dasgupta, P. K. *J. Chromatogr*. **1991**, 546, 159−173.

(78) Liu, Y.; Srinivasan, K.; Pohl, C.; Avdalovic, N. J. *J. Biochem. Biophys. Methods* **2004**, 60, 205−232.

(79) Dasgupta, P. K.; Maleki, F. *Talanta* **2019**, 204, 89−137.

(80) Small, H.; Riviello, J. *Anal. Chem*. **1998**, 70, 2205−2212.

(81) Small, H.; Liu, Y.; Avdalovic, N. *Anal. Chem*. **1998**, 70, 3629− 3635.

(82) Elkin, K.; Riviello, J.; Small, H. *J. Chromatogr. A* **2015**, 1403, 63− 69.

(83) Pyo, D.; Dasgupta, P. K.; Yencoyan, L. S*. Anal. Sci*. **1997**, 13, 185−190.

(84) Ishii, D.; Takeuchi, T. *J. Chromatogr*. **1981**, 218, 189−197.

(85) Manz, A.; Simon, W. *J. Chromatogr. Sci*. **1983**, 21, 326−330.

(86) Muller, S. R.; Simon, W.; Widmer, H. M.; Grolimund, K.; Schomburg, G.; Kolla, P. *Anal. Chem*. **1989**, 61, 2747−2750.

(87) Muller, S. R.; Scheidegger, D.; Haber, C.; Simon, W. *J. High Resolut. Chromatogr*. **1991**, 14, 174−177.

(88) Rokushika, S.; Qiu, Z. Y.; Hatano, H. *J. Chromatogr. A* **1983**, 260, 81−87.

(89) Sjögren, A.; Boring, C. B.; Dasgupta, P. K.; Alexander, J. N. *Anal. Chem***. 1997**, 69, 1385−1391.

(90) Boring, C. B.; Dasgupta, P. K.; Sjögren, A*. J. Chromatogr.* **1998**, 804, 45−54.

(91) Huang, S.; Gao, M.; Zhang, F.; Lu, Y.; Yang, B. *J. Chromatogr. A* **2019**, 1596, 54−58.

(92) Yang, B.; Zhang, F.; Liang, X. *Talanta* **2009**, 79, 68−71.

(93) Yang, B.; Takeuchi, M.; Dasgupta, P. K*. Anal. Chem*. **2008**, 80, 40−47.

(94) Yang, B.; Zhang, F.; Liang, X.; Dasgupta, P. K. *J. Chromatogr. A* **2009**, 1216, 2412−2416.

(95) Strong, D. L.; Dasgupta, P. K. *J. Membr. Sci*. **1991**, 57, 321− 336.

(96) Pridantsev, A. A.; Shalatov, I. A.; Gursky, V. S. Electrodialysis Eluent Generator for Ion Chromatography. European Patent EP 1 685 887 B1, May 27, **2009**.

(97) Lu, Y.; Zhou, L.; Yang, B.; Huang, S.; Zhang, F. *Anal. Chem*. **2018**, 90, 12840−12845.

(98) Huang, W.; Seetasang, S.; Azizi, M.; Dasgupta, P. K. *Anal. Chem*. **2016**, 88, 12013−12020.

(99) Huang, W.; Dasgupta, P. K. *Anal. Chem*. **2016**, 88, 12021− 12027.

(100) Huang, W.; Chouhan, B.; Dasgupta, P. K. *Anal. Chem*. **2018**, 90, 14561−14568.

(101) Eckstrom, H. C.; Schmelzer, C. *Chem. Rev.* **1939**, 24, 367−414.

(102) Kuban, P.; Berg, J. M.; Dasgupta, P. K*. Anal. Chem*. **2004**, 76, 2561−2567.

(103) Dasgupta, P. K.; Bao, L. *Anal. Chem.* **1993**, 65, 1003−1011.

(104) Wien, M. *Ann. Phys*. **1927**, 388, 327−361.

(105) Wien, M. *Phys. Z.* **1931**, 32, 545.

(106) Christian, G. D.; Dasgupta, P. K.; Schug, K. *Anal. Chem.,* 7th ed.; Wiley, New York, **2013**; pp 211−212.

(107) Onsager, L. *J. Chem. Phys*. **1934**, 2, 599−615.

(108) Eigen, M.; Eyring, E. M*. Inorg. Chem*. **1963**, 2, 636−638.

(109) Agmon, N. *Chem. Phys. Lett*. **1995**, 244, 456−462.

(110) Agmon, N. *Chem. Phys. Lett*. **2000**, 319, 247−252.

(111) Atkinson, G.; Yokoi, M. *J. Phys. Chem*. **1962**, 66, 1520−1526.

(112) Ran, J.; Wu, L.; He, Y.; Yang, Z.; Wang, Y.; Jiang, C.; Ge, L.; Bakangura, E.; Xu, T. *J. Membr. Sci*. **2017**, 522, 267−291.

(113) Yang, B. C.; Zhang, M.; Kanyanee, T.; Stamos, B. N.; Dasgupta, P. K*. Anal. Chem***.** **2014**, 86, 11554−11561.

(114) Gormley, P. G.; Kennedy, M*. Proc. R. Ir. Acad., Sect. A* **1949**, 52, 163−169.

(115) Huang, W.; Pohl, C. A.; Dasgupta, P. K. *J. Chromatogr. A* **2018**, 1550, 75−79.

(116) El Moussaoui, R.; Pourcelly, G.; Maeck, M.; Hurwitz, H. D.; Gavach, C. *J. Membr. Sci*. **1994**, 90, 283−292.

(117) Hwang, U. S.; Choi, J. H. *Sep. Purif. Technol*. **2006**, 48, 16−23.

(118) Gilliam, R. J.; Graydon, J. W.; Kirk, D. W.; Thorpe, S. J. *Int. J. Hydrogen Energy* **2007**, 32, 359−364.

Biographical Information

Bikash Chouhan earned his Master of Science degree in chemistry from Tribhuvan University, Kirtipur, Nepal. After his master's degree, he worked in a food laboratory under government of Nepal for about seven years. He was offered an opportunity to pursue his Ph.D. degree in the Department of Chemistry and Biochemistry, University of Texas at Arlington, in January 2015. He joined professor Dasgupta's lab in the fall of 2015. He worked in the field of ion chromatography, especially in developing eluent generators, eluent suppressors and solution contact conductivity detection cells for small bore open tubular ion chromatography. He also developed a new method to measure photothermal optical absorption.